國立臺灣大學電機資訊學院光電工程學研究所

碩士論文

Graduate Institute of Photonics and Optoelectronics

College of Electrical Engineering and Computer Science

National Taiwan University

Master Thesis

微小非球面鏡於微型化視頻非線性光學顯微鏡之應用

The Application of Mini Aspheric Lens in Miniaturized Video-rate
Nonlinear Optical Microscope

鍾向宇

Hsiang-Yu Chung

指導教授：孫啟光 博士

Advisor: Chi-Kuang Sun, Ph.D.

中華民國 102 年 7 月

July, 2013

誌謝

摘要

非線性光學顯微術的發展已經有許多年了。其相對於傳統顯微鏡較為優秀的光學虛擬切片能力，來自於其光學機制–非線性訊號僅限於物鏡焦點的附近才能產生。該顯微術所使用的光源通常為近紅外光，相對於一般可見光不只對於生物體擁有較低的破壞性，更有較佳的穿透深度。典型非線性光學顯微系統的架設是直接將一般的顯微鏡與雷射光源和額外的掃瞄機制整合在一起，然而這將使的整個系統顯得笨重許多。

為使非線性光學顯微術在臨床上能更方便應用，則原本笨重的系統就必須被縮小、重新設計。在本論文中，我們研究的重心將會擺在微小化的鏡頭上。在我們的藍圖中，一個微小化的觀測鏡頭是必要的，因為一個手持大小的系統在觀測過程中可以擁有更多方便性及彈性。再者，我們希望這個鏡頭能提供寬廣的觀測視野，這樣在觀察的過程中我們便可同時揭露更多資訊；系統的掃描機制如果能夠提供夠高的畫面更新率，則在觀察過程中微小震動造成影像模糊的問題可以獲得改善，甚至可以進行動態影像觀察的應用。

非球面鏡名稱的由來在於其表面並非剛好是正球型的一部份。相對於一般簡易生產的球面鏡，其較複雜的表面是專門設計用來減少像差或是取代多重鏡組。一些非球面鏡被設計的非常小，並被應用在手機相機鏡頭、光碟機讀取頭或是雷射二極體準直鏡上。這些鏡子的尺寸都不大而且價錢也相當便宜，或許可以用來作為傳統顯微物鏡的替代品並發揮類似的功能。
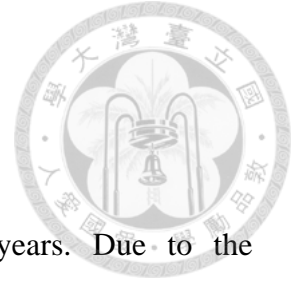
在本論文中，我們將呈現我們對於高數值孔徑微小非球面鏡（0.85 NA 藍光光碟機鏡頭、0.8 NA 雷射二極體準直鏡）作為微型化非線性光學顯微系統物鏡的潛力

之研究。本系統的構造非常簡單，只有 5 片鏡子。微小非球面鏡與不同放大倍率之筒鏡被組合起來當作系統的物鏡，微機電鏡擔任系統掃描機制的角色，一片二色的分光鏡則用來區隔入射的紅外光與反射的可見光訊號。我們研究了該系統在不同非線性光學訊號上之表現，諸如：雙光子螢光、二倍頻、三倍頻，並使用綠螢光斑馬魚來評估生物活體實驗的可行性，以及動態影像的觀察。在論文中，亦涵蓋了本設計與其他不同微小化系統設計的比較。

關鍵字：雷射、非球面鏡、微機電鏡、非線性光學顯微術

ABSTRACT

Nonlinear optical microscopy has been developed for many years. Due to the mechanism of nonlinear optics, the nonlinear signal can only be generated around the focus of the objective. Thus, this kind of microscopy is known for its optical virtual biopsy ability in comparison with the traditional wide field microscopy. The excitation light is infrared, which is not only less invasive but also provides better depth of penetration. Typical way to apply nonlinear optical microscopy is directly integrating a conventional microscope with a laser light source and some additional scanning mechanisms. However, it will make the whole system bulkier.

In order to apply nonlinear optical microscopy in clinical applications, the system must be miniaturized and redesigned for more flexibility. In this thesis, the investigation is focused on the miniaturized imaging head. An optical imaging head with a miniaturized size, a larger field of view (FOV), and a video frame-rate is highly desired because a miniaturized system is more convenient to be manipulated during the observation and allows intravital applications. Larger field of view means we can reveal more information once simultaneously. Higher frame rate can not only deal with the image blurring problem resulted from vibrations but also allow one to reduce the imaging acquisition time, thus dynamic observation may be realized.

Aspheric lenses, which are known for their complex lens surface profile designed for aberration reduction or replacement for a multi-lens system, are used in 3C products, such as cell phone cameras, optical disk drives, or laser diode collimators. With its smaller size and cheaper price, it could be an alternative to traditional objectives in

miniaturized nonlinear microscopy systems.

In this thesis, we present our investigation on the potential to use high numerical aperture mini aspheric lens (a blu-ray disk lens with 0.85 NA and a laser diode collimating lens with 0.8 NA) as the objective of the miniaturized nonlinear microscopy system. The structure of the system is very simple, and only five mirrors or lenses are used. The mini aspheric lens is integrated with a tube lens pair for beam size magnification. A MEMS mirror acts as a scanner, and a dichroic beam splitter separates the excitation light and the epi-collected signal. We investigate its performance for 2PF (two-photon fluorescence), SHG (second harmonic generation), and THG (third harmonic generation) microscopies. Live GFP (green fluorescence protein) zebrafish is used to estimate the feasibility of *in-vivo* experiment and the ability of dynamic observation. Comparison among different systems from other groups is also listed.

Keywords: Laser, Aspheric lens, MEMS mirror, Nonlinear optical microscopy

CONTENTS

LIST OF FIGURES

xiii

LIST OF TABLES

Chapter 1 Introduction

1.1 Historical overview of microscopy

After passing through different media, light will refract. According to this mechanism, lenses with different kinds of surface were used to converge or diverge the light. Simply combing these lenses, the history of the very first microscope could be traced back to 16th century. Since then, the study of using a microscope as an instrument to observe the thing that we can't see merely by our naked eyes is called microscopy.

The process of microscopy usually has lots to do with refractions, reflections, or diffractions and the collections of the scattered signals. The microscopy using light as the illumination during these processes is called optical microscopy, whereas electron microscopy uses the electron for the similar purposes since 1930s. In 1931 the first transmission electron microscope (TEM) was built by Max Knoll and Ernst Ruska [1.1], and in 1935Max Knoll got the first scanning electron microscope (SEM) image [1.2]. After 1980, by scanning a probe over the surface of the specimen and analyzing the interaction, the scanning probe microscopy (SPM) had been founded with the invention of the scanning tunneling microscope (STM) [1.3]. In this thesis, we only focus on the part of optical microscopy.

The theoretical limitation of the resolution in traditional optical microscopy is about 0.2 micrometers (We'll discuss this topic more in Chapter 2), but the actual performance normally can't reach such a level. The reason is due to the wide-field illumination of the incidence, so the light comes from the place out of the focus contributes to the
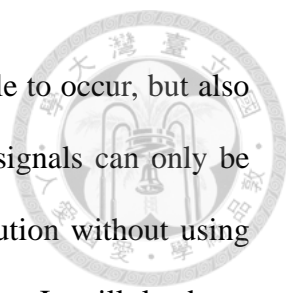
background and thus blurs the image. In 1957, a method using pinholes to improve the resolution was demonstrated by Marvin Minsky [1.4]. The idea was simple and known as confocal microscopy [1.5]. A pinhole is designed to allow the light scattered from the same focal plane to pass through and blocks the out of focus lights. However, this method requires an additional scanning mechanism since once only one spot could be illuminated instead of the wide-field illumination.

Although the resolution could be improved in confocal microscopy, but the intensity of the signal also weakens since most part of the light is blocked by the pinhole, thus lowers the signal to noise ratio (SNR). To recover the ratio, we can reduce the noise or average the signal, but it's not efficient enough than directly increase the intensity of the incidence. However, the higher power the specimen is exposed to, the more likely the photodamage occurs. Accordingly, observation in biological tissues is restricted by the damage threshold of the intensity.

After the invention of laser in 1960 [1.6], different wavelength light sources and various types of laser scanning microscopy (LSM) had been developed [1.7]. Then nonlinear optical microscopy started to be developed as the introduction of pulsed laser. Based on different nonlinear processes, various kinds of nonlinear optical microscopy could be conducted, such as two-photon fluorescence (2PF) microscopy [1.8], harmonic generation (HG) microscopy [1.9], or coherent anti-Stokes Raman scattering (CARS) microscopy [1.10].

2PF microscopy is first realized in 1990 [1.8]. The application of pulsed laser as the illumination source can provide an instantaneous extremely high intensity but a low

average intensity. Thus, not only the nonlinear optical effects are able to occur, but also the risk of damage is lowered. Besides, the feature that nonlinear signals can only be generated near the focus of an objective also provides a fine resolution without using pinholes. However, 2PF is not a completely noninvasive process. It still leads to photodamage and photobleaching [1.11].

HG process is related to only virtual state energy level transition, whereas 2PF induces energy deposition to the object. So we can regard HG as a truly noninvasive process. The application of HG can be traced back to 1961. Just one year after the invention of laser, the concept of second harmonic generation (SHG) is demonstrated [1.12]. In 1968, SHG from media with inversion symmetry is reported [1.13]. Then the first microscopy imaging of SHG signal was reported in 1974 from polycrystalline ZnSe [1.9], and the first biological imaging experiment to study the orientation of collagen fibers in rat tail tendon was done in 1986 [1.14]. Then SHG is applied in various biological studies, ex: membrane potentials [1.15-1.18], microtubule polarity [1.14, 1.19-1.20], extracellular matrix structure [1.21-1.23], and cellular structure [1.24]. Some studies by our group also indicate that SHG signals can be generated spatially organized crystalline structures with inversion symmetry, ex collagen fibrils [1.25], skeleton muscle [1.25-1.26], cardiac muscle, mitosis spindles [1.27], and polyhedral inclusion bodies of nuclear polyhedrosis viruses [1.28].

Third harmonic generation (THG) is another kind of HG process. Though it is relatively weak in comparison with SHG, it can be generated from all surfaces with different diffraction index [1.29], whereas SHG can only be generated only from inversion symmetry structural [1.13]. The concept of THG is first reported in 1995 [1.29]. Then in

1996, THG is found in chicken tissues [1.30], and the first microscopy demonstration of THG was done in 1997 within an optical fiber [1.31]. Due to the interface sensitivity feature, THG started to be applied in the study of morphological and interfacial imaging or cellular and subcellular organelles [1.32-1.36].
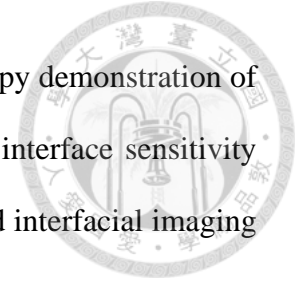
As nonlinear optical microscopy gradually becomes a tool for biological or medical study these years, the feasibility of the system as a medical assistant tool or the ability of clinical application becomes a topic. Thus, some efforts were done in order to miniaturize the microscope system or design a suitable endoscope. The concerning work usually relates to the miniaturization of the laser light source, and the microscope imaging head. A review and comparison of these works on miniaturized microscope system for the past ten years are presented in Chapter 4, which includes the method and the performance.

1.2 Structure of this thesis

This thesis is about the application of mini aspheric lens in a miniaturized nonlinear optical microscope. The content is composed of 5 chapters. The followings are some descriptions of each chapter respectively.

In Chapter 1, the historical overview of microscopy is briefly described and the structure of the thesis is shown.

In Chapter 2, basic principles are mentioned. First, some basic important conceptions of microscopy are discussed, including the resolution and the aberration. Then the mechanism of nonlinear optics by different process is introduced, such as harmonic

generation and multi-photon fluorescence. The last part of this chapter is the discussion about the nonlinear effect occurred while light is delivering in an optical fiber.
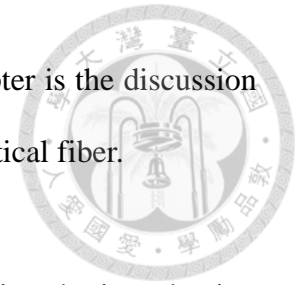
Chapter 3 is about the nonlinear optical microscope system, including the introduction of different light source and the historical review of the system miniaturization. Comparison between different miniaturized systems is also listed at the end of this chapter.

In the beginning of chapter 4, the method we used in this thesis is demonstrated. It roughly consists of two parts: the optical and the electronic one. The optical part is about the imaging head design. Various home-designed tube lens pairs are integrated with different kinds of mini aspheric lens to optimize the performance. The electronic part is about the control of the MEMS scanning mirror and instant mapping. An FPGA computer system is introduced to not only generate synchronized control signals but also deal with the mass data processing. Combining all the above equipment together, finally a miniaturized microscope could be presented. By repackaging, the imaging head is further miniaturized. Then the performance of the system is discussed, such as the field of view (FOV) and resolution analysis. Finally, dynamic observation of *in-vivo* GFP zebrafish heartbeat by 2PF microscopy is the highlight of this thesis.

Chapter 5 is the summary of this work and the possible future work.
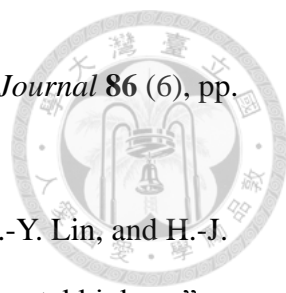
Reference

[1.1]   T. Mulvey, "The electron microscope: The British contribution," *Journal of Microscopy* **155** (3), pp. 327-338 (1989).

[1.2]   L. Reimer, "Scanning Electron Microscopy: Physics of Image Formation and Microanalysis," *Meas. Sci. Technol*. **11**, pp. 1826 (2000).

[1.3]   G. Binnig, H. Rohrer, Ch. Gerber, and E. Weibel, "Surface Studies by Scanning Tunneling Microscopy," *Phys. Rev. Lett*. **49** (1), pp. 57–61 (1982).

[1.4]   M. Minsky, "Microscopy Apparatus," U.S. Patent no. 3013467 (1957).

[1.5]   C. J. R. Sheppard and D. M. Shotton, *Confocal Laser Scanning Microscopy* (Oxford, 1997).

[1.6]   T.H. Maiman, "Stimulated Optical Radiation in Ruby," *Nature* **187**, pp. 493-494 (1960).

[1.7]   W. J. Alford, R. D. Vanderneut, and V. J. Zaleckas, "Laser scanning microscopy," *Proceedings of IEEE* **70** (6), pp. 641-651 (1982).

[1.8]   W. Denk, J.H. Strickler, and W.W. Webb, "Two-photon laser scanning fluorescence microscopy," *Science* **248**, pp. 73-76 (1990).

[1.9]   R. Hellwarth, and P. Christensen, "Nonlinear optical microscopic examination of structure in polycrystalline ZnSe," *Optics Communications* **12** (3), pp. 318-322 (1974).

[1.10] M. D. Duncan, J. Reintjes, and T. J. Manuccia, "Scanning coherent anti-Stokes Raman microscope," *Optics Letters* **7** (8), pp. 350-352 (1982).

[1.11] K. König, P. T. C. So, W. W. Mantulin, and E. Gratton, "Cellular response to near-infrared femtosecond laser pulses in two-photon microscopes," *Optics Letters* **22** (2), pp. 135-136 (1997).

[1.12] P. A. Franken, A. E. Hill, C. W. Peters, and G. Weinreich, "Generation of

Optical Harmonics," *Phys. Rev. Lett.* **7**, pp. 118–119 (1961).

[1.13] N. Bloembergen, R. K. Chang, S. S. Jha, and C. H. Lee, "Optical Second-Harmonic Generation in Reflection from Media with Inversion Symmetry," *Phys. Rev.* **174**, pp. 813–822 (1968).

[1.14] I. Freund, M. Deutsch, and A. Sprecher, "Connective tissue polarity. Optical second-harmonic microscopy, crossed-beam summation, and small-angle scattering in rat-tail tendon," *Biophysical Journal* **50** (4), pp. 693-712 (1986).

[1.15] G. Peleg, A. Lewis, M. Linial, and L. M. Loew," Nonlinear optical measurement of membrane potential around single molecules at selected cellular sites," *Proceedings of the National Academy of Sciences of the United States of America* **96**, pp. 6700-6704 (1999).

[1.16] L. Moreaux, O. Sandre, and J. Mertz, "Membrane imaging by second-harmonic generation microscopy," *J. Opt. Soc. Am. B* **17** (10), pp. 1685-1694 (2000).

[1.17] A. C. Millard, L. Jin, A. Lewis, and L. M. Loew, "Direct measurement of the voltage sensitivity of second-harmonic generation from a membrane dye in patch-clamped cells," *Optics Letters* **28** (14), pp. 1221-1223 (2003).

[1.18] D. A. Dombeck, M. Blanchard-Desce, and W. W. Webb, "Optical Recording of Action Potentials with Second-Harmonic Generation Microscopy," *The Journal of Neuronscience* **24**, pp. 999-1003 (2004).

[1.19] Y.-C. Guo, P. P. Ho, H. Savage, D. Harris, P. Sacks, S. Schantz, F. Liu, N. Zhadin, and R. R. Alfano," Second-harmonic tomography of tissues," *Optics Letters* **22** (17), pp. 1323-1325 (1997).

[1.20] D. A. Dombeck, K. A. Kasischke, H. D. Vishwasrao, M. Ingelsson, B. T. Hyman, and W. W. Webb, "Uniform polarity microtubule assemblies imaged
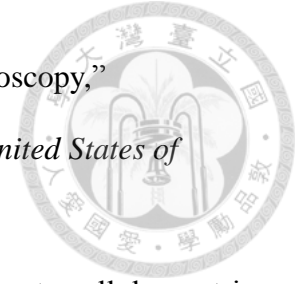
in native brain tissue by second-harmonic generation microscopy," *Proceedings of the National Academy of Sciences of the United States of America* **100**, pp. 7081-7086 (2003).

[1.21] A. Zoumi, A. Yeh, and B. J. Tromberg, "Imaging cells and extracellular matrix *in vivo* by using second-harmonic generation and two-photon excited fluorescence," *Proceedings of the National Academy of Sciences of the United States of America* **99**, pp. 11014-11019 (2002).

[1.22] W. Mohlera, A. C. Millardb, and P. J. Campagnola, "Secondharmonicgeneration imaging of endogenous structural proteins," *Methods* **29**, pp. 97-109 (2003).

[1.23] W. R. Zipfel, R. M. Williams, R. Christie, A. Y. Nikitin, B. T. Hyman, and W. W. Webb, "Live tissue intrinsic emission microscopy using multiphoton-excited native fluorescence and second harmonic generation," *Proceedings of the National Academy of Sciences of the United States of America* **100**, pp. 7075-7080 (2003).

[1.24] P. J. Campagnola, A. C. Millard, M. Terasaki, P. E. Hoppe, C. J. Malone, and W. A. Mohler, "Three-Dimensional High-Resolution Second-Harmonic Generation Imaging of Endogenous Structural Proteins in Biological Tissues," *Biophysical Journal* **82**, pp. 493-508 (2002).

[1.25] S.-W. Chu, I.-H. Chen, T.-M. Liu, C.-K. Sun, S.-P. Lee, B.-L. Lin, P.-C. Cheng, M.-X. Kuo, D.-J. Lin, and H.-L. Liu, "Nonlinear bio-photonic crystal effects revealed with multimodal nonlinear microscopy," *Journal of Microscopy* **208** (3), pp. 190-200 (2002).

[1.26] S.-W. Chu, S.-Y. Chen, G.-W. Chern, T.-H. Tsai, Y.-C. Chen, B.-L. Lin, and C.-K. Sun, "Studies of $\chi(2)/\chi(3)$ Tensors in Submicron-Scaled Bio-Tissues by

Polarization Harmonics Optical Microscopy," *Biophysical Journal* **86** (6), pp. 3914-3922 (2004).

[1.27]   C.-K. Sun, S.-W. Chu, S.-Y. Chen, T.-H. Tsai, T.-M. Liu, C.-Y. Lin, and H.-J. Tsai, "Higherharmonicgeneration microscopy for developmental biology," *Journal of Structural Biology* **147** (1), pp. 19-30 (2004).

[1.28]   T.-M. Liu, Y.-W. Lee, C.-F. Chang, S.-C. Yeh, C.-H. Wang, S.-W. Chu, and C.-K. Sun." Imaging polyhedral inclusion bodies of nuclear polyhedrosis viruses with second harmonic generation microscopy," *Optics Express* **16** (8), pp. 5602-5608 (2008).

[1.29]   T. Y. F. Tsang, "Optical third-harmonic generation at interfaces," *Phys. Rev. A* **52**, pp. 4116–4125 (1995).

[1.30]   Y. Guo, P.-P. Ho, A. Tirksliunas, F. Liu, and R. R. Alfano, "Optical harmonic generation from animal tissues by the use of picosecond and femtosecond laser pulses," *Applied Optics* **35** (34), pp. 6810-6813 (1996).

[1.31]   Y. Barad, H. Eizenberg, M. Horowitz and Y. Silberberg, "Nonlinear scanning laser microscopy by thirdharmonic generation," *Appl. Phys. Lett*. **70**, pp. 922-924 (1997).

[1.32]   M. Müller, J. Squier, K. R. Wilson, and G. J. Brakenhoff," 3D microscopy of transparent objects using third-harmonic generation," *Journal of Microscopy* **191** (3), pp. 266–274 (1998).

[1.33]   J. A. Squier, M. Muller, G. J. Brakenhoff, and K. R. Wilson, "Third harmonic generation microscopy," *Optics Express* **3** (9), pp. 315-324 (1998).

[1.34]   D. Yelin and Y. Silberberg, "Laser scanning third-harmonic-generation microscopy in biology," *Opt. Express* **5**, pp. 169-175 (1999).

[1.35]   S.-W. Chu, I-H. Chen, T.-M. Liu, P.-C. Chen, C.-K. Sun, and B.-L. Lin,

"Multimodal nonlinear spectral microscopy based on a femtosecond Cr:forsterite laser," *Optics Letters* **26** (23), pp. 1909-1911 (2001).

[1.36] C.-K. Sun, S.-W. Chu, S.-P. Tai, S. Keller, U. K. Mishra, and S. P. DenBaars, "Scanning second-harmonicÔ third-harmonic generation microscopy of gallium nitride," *Appl. Phys. Lett.* **77**, pp. 2331-2333 (2000).
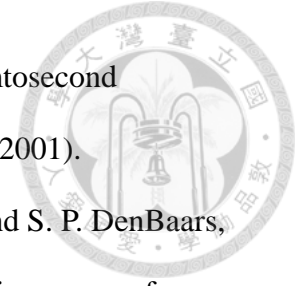
Chapter 2 Basic principles

2.1 Basic conceptions of microscopy

2.1.1 Resolution

When the incident light passes through or reflects by the target, such as a small hole or a small spot, it will generate a diffraction pattern with a central bright spot known as the airy disk and surrounded by a series of bright and dark rings. These circular stripes are due to the interference of higher orders of the beam. The constructive interference generates the bright stripes, whereas the destructive interference generates the dark ones. Thus, there appears the diffraction pattern [2.1].

Considering the radius of the airy disk is *r*. Lord Rayleigh set a criterion [2.1] to determine if two very close adjacent beam spots could be distinguished from each other or not. When two beam spots are separated by a distance *r*, the center of the airy disk just locates on the center of the first node (the dark ring) one another. Thus, the intensity between two peaks of the beam is up to about 85% of the peak. These two points can still be resolved, and the minimum distance *d* is defined as the resolving power and can be shown as [2.2]

$$d = \frac{0.61\lambda}{n\sin\theta} = \frac{0.61\lambda}{NA}$$

(2.1) (Rayleigh's criterion)

where λ is the wavelength of the incidence, n is the refractive index, and θ is the half-angle of the acceptance of the lens. The denominator $n\sin\theta$ characterizes the range of the angle is also known as the numerical aperture (NA) of the lens.
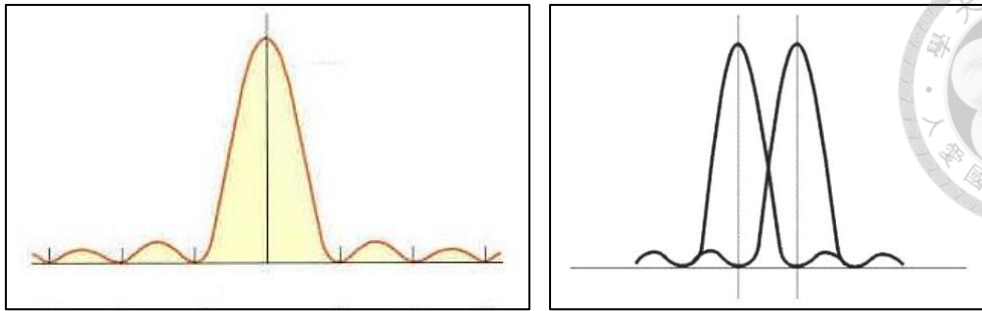
Fig 2.1 The diffraction pattern and the Rayleigh criterion.

If there is only one point, we can just consider its full width at half maximum (FWHM) [2.2] of the point spread function (PSF) as the resolution power, thus

$$d = \frac{0.51\lambda}{n \sin \theta} = \frac{0.51\lambda}{NA}$$

(2.2) (Sparrow's criterion)

which is slightly lower than the value from Rayleigh's criterion because many astronomers say they can still distinguish the two stars even when they're closer than Rayleigh's resolution limit.

From Eq. 2.1 and Eq. 2.2, obviously there are two ways to improve the resolution: either using light with shorter wavelength as the incidence or using higher NA optics. Typically, the lens is designed for usage in air. Combing with Different immersion media, higher NA can be achieved. Water-immersion lens can provides NA over 1, whereas even higher NA can be provided by oil-immersion ones.

2.1.2 Aberration

The well-known Snell's law [2.3] is shown below

$$n_I \sin \theta_I = n_R \sin \theta_R$$
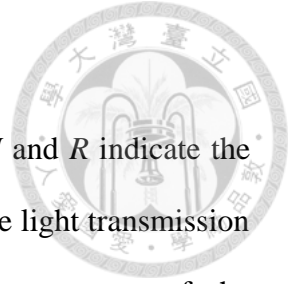
(2.3)

where n is the refractive index, θ is the angle, and the subscripts I and R indicate the incident and the refractive light, respectively. This law determines the light transmission mechanism between two distinct media and strongly contributes to most of the aberrations due to the difference of refractive index among all wavelengths. Aberrations could be roughly sorted into six types [2.4-2.5]: chromatic, spherical, coma, astigmatism, curvature of field, and distortion. They may affect the performance and make the optical system imperfect. Since most of the light passes through the central part of the lens, here we consider only the first three factors under the paraxial assumption.

In chromatic aberration, light with different wavelength has different refractive index, which is also called dispersion. White light is actually a mixture of light with different color. The blue light part has a greater value of refractive index than the red part does, so it suffers more deflections while passing through a convex lens. Thus blue light focuses on a closer place from the lens than red light does. Fortunately, the excitation source we use could be considered highly monochromatic, so this factor could be ignored.

Even though the light is monochromatic, it still suffers geometric aberration called spherical aberration. Off-axis and paraxial light can't converge at the same focus without passing through a perfect parabolic lens. Unfortunately, it's hard to fabricate such perfect parabolic lens, and the price is also expensive. In normal circumstances, spherical shape lens is used as a substitution for low-order approach due to its cheap price and since it can be relatively easily produced.

The name of coma, or also called comatic aberration, originates from the incidence oblique to the lens axial not focusing on the same point. This could be regarded as a series of variation in magnification over the clear aperture (CA). In laser scanning microscopy (LSM), this may induce the distortion around the scanning area. The farther from the center, the severe the distortion is. While the numerical aperture (NA) of a lens increases, the theoretical resolution is improved. However, the coma becomes stronger at the same time.
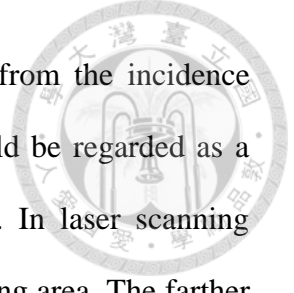
2.2. Nonlinear optics

2.2.1 Second harmonic generation (SHG)

Assuming an electric field of a laser beam can be presented as [2.6]

$$\tilde{E}(t) = \frac{1}{2}\left[E(\omega)e^{-i\omega t} + E(-\omega)e^{i\omega t}\right]$$

(2.4)

The created second-order nonlinear polarization is [2.6]

$$\tilde{P}^{(2)}(t) = \varepsilon_0\chi^{(2)}\tilde{E}(t)^2$$
$$= \frac{1}{2}\varepsilon_0\chi^{(2)}(0:\omega,-\omega)EE^* + (\frac{1}{4}\varepsilon_0\chi^{(2)}(2\omega:\omega,\omega)E^2e^{-i2\omega t} + c.c.)$$

(2.5)

According to the driven wave equation [2.7]

$$\left(\nabla^2 - \mu_0\sigma\frac{\partial}{\partial t} - \mu_0\varepsilon\frac{\partial^2}{\partial t^2}\right)\tilde{E} = \mu_0\frac{\partial^2\tilde{P}}{\partial t^2}$$

(2.6)

The first term $(\chi^{(2)}(0:\omega,-\omega))$ on the right-hand side of Eq. 2.5 contributes zero

14

frequency, and it doesn't generate electromagnetic field since its second time derivative is zero. This process is known as the optical rectification, and a static electric field will be created. The second term ($\chi^{(2)}(2\omega:\omega,\omega)$) contributes 2ω frequency which is the process of second harmonic generation (SHG). In SHG, one photon of frequency 2ω is generated while two photons of frequency ω vanish simultaneously. The intensity of the induced signal is proportional to the square power of the excitation source. Fig. 2.2 shows the schematic diagram of SHG. The solid line represents ground state whereas the dashed lines represent virtual states.

If we change the sign of the electric field in Eq. 2.5, the sign of the induced polarization also changes. Then we get [2.6]

$$-\tilde{P}^{(2)}(t) = \varepsilon_0\chi^{(2)}[-\tilde{E}(t)^2] = \varepsilon_0\chi^{(2)}\tilde{E}(t)^2$$

(2.7)

In comparison with Eq. 2.5, then [2.8]

$$\tilde{P}^{(2)}(t) = -\tilde{P}^{(2)}(t)$$

(2.8)

This only validates when $\tilde{P}^{(2)}(t)$ vanishes, so $\chi^{(2)}$ is zero. Thus, SHG cannot be observed in material with centro-symmetry (possesses center of inversion). It's allowed only in material without inversion symmetry [2.8-2.9].
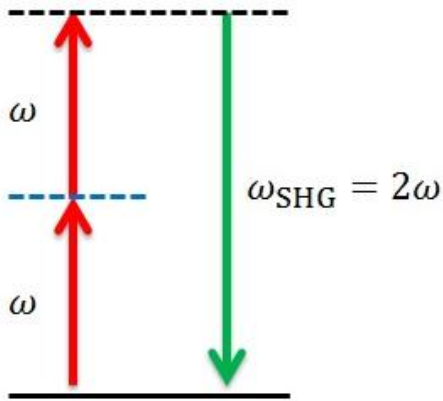
Fig 2.2 Jablonski diagram of SHG.

2.2.2 Third harmonic generation (THG)

Same as previous assumption for the electric field, the created third-order nonlinear polarization is [2.6]

$$\tilde{P}^{(3)}(t) = \varepsilon_0 \chi^{(3)} \tilde{E}(t)^3$$
$$= \frac{1}{8}\varepsilon_0\left(\chi^{(3)}(3\omega:\omega,\omega,\omega)E^3 e^{-i3\omega t} + 3\chi^{(3)}(\omega:\omega,0,0)E^2 E e^{-i\omega t} + c.c.\right)$$

(2.9)

Considering only the real part then we get [2.6]

$$\frac{1}{4}\varepsilon_0\chi^{(3)}(3\omega:\omega,\omega,\omega)E^3\cos 3\omega t + \frac{3}{4}\varepsilon_0\chi^{(3)}(\omega:\omega,0,0)|E|^2 E\cos \omega t$$

(2.10)

The first term $(\chi^{(3)}(3\omega:\omega,\omega,\omega))$ on the right hand side contributes 3ω frequency which is the process of third harmonic generation (THG). During the process, one photon of frequency 3ω is generated while three photons of frequency ω vanish simultaneously. Unlike SHG, the intensity of the generated signal tends to increase as the cubic power of the intensity of the applied light source. The schematic diagram of
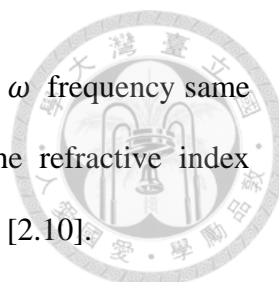
THG is showed in Fig. 2.3. The term $(\chi^{(3)}(\omega:\omega,0,0))$ contributes ω frequency same as the incidence, which leads to a third-order contribution to the refractive index experienced by a wave of frequency ω, known as optical Kerr effect [2.10].

$\chi^{(3)}$ doesn't vanish when we change the sign of the electric field. This feature allows THG generated in material of all kinds structure, including inversion symmetry. However, we should consider Gouy phase shift [2.11] under strong focusing laser beam. The phase of the focusing light will shift by π while propagating through the focus, and leads to a destructive interference for THG [2.8-2.9]. Thus, theTHG signal can only be generated without a destructive interference when the focus is located around an inhomogeneous medium [2.12]. That's why THG is able to distinguish interfaces [2.12].
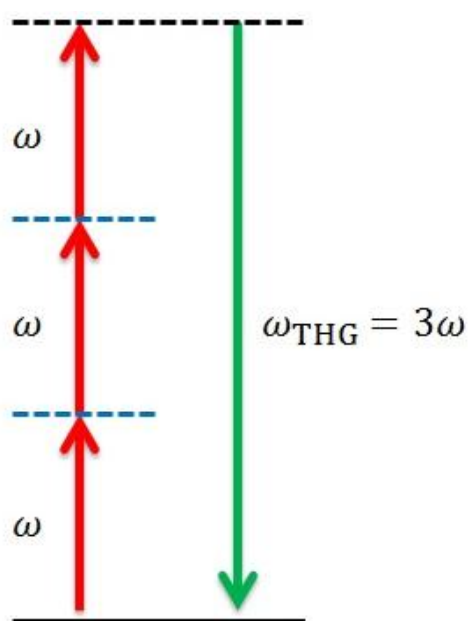
Fig 2.3 Jablonski diagram of THG.

2.2.3 Two-photon fluorescence (2PF)

Previous discussion about the harmonic generation (HG) and the optical Kerr effect are
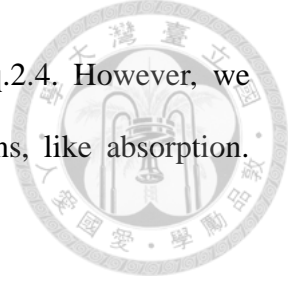
related only with virtual state transitions and the real part of Eq.2.4. However, we should also consider the imaginary part while real state transitions, like absorption. Considering $\chi^{(3)}$ and the constitutive law, then we can derive [2.9]

$$\tilde{D} = \varepsilon\tilde{E} = \varepsilon_0\tilde{E} + \tilde{P} = \varepsilon_0\tilde{E} + \tilde{P}^{(1)} + \tilde{P}^{(3)}$$

$$= \varepsilon_0\tilde{E} + \varepsilon_0\big(\mathrm{Re}\chi^{(1)} + i\mathrm{Im}\chi^{(1)}\big)\tilde{E} + \varepsilon_0\left(\frac{3}{4}\mathrm{Re}\chi^{(3)}\big|\tilde{E}\big|^2 + \frac{3}{4}\mathrm{Im}\chi^{(3)}\big|\tilde{E}\big|^2\right)\tilde{E}$$

$$= \varepsilon_0\tilde{E} + \varepsilon_0\left(\mathrm{Re}\chi^{(1)} + \frac{3}{4}\mathrm{Re}\chi^{(3)}\big|\tilde{E}\big|^2\right)\tilde{E}$$

$$+ i\varepsilon_0\left(\mathrm{Im}\chi^{(1)} + \frac{3}{4}\mathrm{Im}\chi^{(3)}\big|\tilde{E}\big|^2\right)\tilde{E} = \varepsilon_0(1 + \mathrm{Re}\chi + \mathrm{Im}\chi)\tilde{E}$$

(2.11)

where $\mathrm{Re}\chi = \mathrm{Re}\chi^{(1)} + \frac{3}{4}\mathrm{Re}\chi^{(3)}\big|\tilde{E}\big|^2$, $\mathrm{Im}\chi = \mathrm{Im}\chi^{(1)} + \frac{3}{4}\mathrm{Im}\chi^{(3)}\big|\tilde{E}\big|^2$

Assuming the electric field of a propagating plane wave is

$$\tilde{E} = E_0 e^{ikz}e^{-i\omega t}$$

(2.12)

where z direction is the propagation direction.

The relation between the wave number k and the susceptibility could be presented as [2.9]

$$k = \omega\sqrt{\mu\varepsilon} = \omega\sqrt{\mu\varepsilon_0(\mathrm{Re}\chi + \mathrm{Im}\chi)} = \frac{\omega}{c}(1 + \mathrm{Re}\chi)^{\frac{1}{2}}\left(1 + \frac{i\mathrm{Im}\chi}{1 + \mathrm{Re}\chi}\right)^{\frac{1}{2}}$$

$$\cong \frac{\omega n}{c} + i\frac{\omega}{2cn}\mathrm{Im}\chi = \mathrm{Re}k + i\mathrm{Im}k$$

(2.13)

where $n = (1 + \mathrm{Re}\chi)^{\frac{1}{2}}$ is the optical refractive index.

After substitution, the electric field becomes

$$\tilde{E} = E_0 e^{i(\mathrm{Re}kz - \omega t)} e^{-\mathrm{Im}kz}$$

(2.14)

where $\mathrm{Im}k$ corresponds to absorption.

Considering Eq. 2.13 and Eq. 2.14, we can get [2.9]

$$\frac{d\tilde{E}}{dz} \propto (i\mathrm{Re}k - \mathrm{Im}k) = i\mathrm{Re}k - \frac{\omega}{2cn}\left(\mathrm{Im}\chi^{(1)} + \frac{3}{4}\mathrm{Im}\chi^{(3)}I\right)$$

(2.15)

where $I = \frac{n_0}{2}\sqrt{\frac{\varepsilon_0}{\mu_0}}|E|^2$ is the intensity of excitation. The term $\mathrm{Im}\chi^{(1)}$ and $\mathrm{Im}\chi^{(3)}$ contribute to linear and nonlinear absorption, respectively. If we introduce E_{tp} as the two-photon absorbed electric field strength, the nonlinear contribution could be showed as [2.13]

$$\left|\frac{dE_{tp}}{dz}\right| = \left|\frac{3\omega}{4cnn_o}\mathrm{Im}\chi^{(3)}\sqrt{\frac{\mu_0}{\varepsilon_0}}\right|$$

(2.16)

If the intensity of nonlinear absorption is

$$I_{tp} = E_{tp} \times E_{tp}^*$$

(2.17)

then we get [2.13]

$$\frac{dI_{tp}}{dz} \propto I^2$$

(2.18)
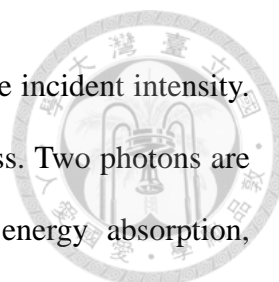
The intensity of absorption is proportional to the square power of the incident intensity. This could be considered as the two-photon absorption (2PA) process. Two photons are absorbed simultaneously when the process occurs. Due to the energy absorption, molecules can be stimulated to excited states or even be ionized.

The process of two-photon fluorescence (2PF) consists of two parts. A schematic diagram is showed in Fig 2.4. First, a molecule is in its ground state (I). After 2PA process (excitation light with frequency ω), it makes a transition to a higher excited state (II). Then it quickly drops to a metastable state (III). Finally it emits a photon with a frequency almost the double of the incidence, but less than 2ω.
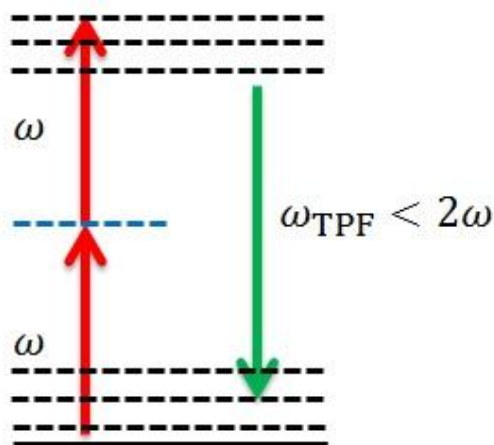
Fig 2.4 Jablonski diagram of 2PF.

2.3 Phenomena in optical fibers

2.3.1 Dispersion

The feature that the group velocity of a wave propagating in media depends on the frequency is called dispersion or group velocity dispersion (GVD) [2.6]. It is also called

chromatic dispersion since the difference of frequency (or wavelength) leads to different phase velocity.

As a result, a laser pulse will suffer dispersion while it's delivered by an optical fiber. The dispersion can be sorted into two types. The material dispersion depends on the characteristic of the waveguide material, whereas the waveguide dispersion concerns the geometrical structure of the waveguide.

If we're going to use an optical fiber to transmit the excitation laser pulse (which is very common in a miniaturized system), we have to evaluate the influence of the dispersion.

If we introduce the propagation constant β and expand it in Taylor series, then we can get [2.14]:

$$\beta(\omega) = n(\omega)\frac{\omega}{c} = \beta_0 + \beta_1(\omega - \omega_0) + \frac{1}{2}\beta_2(\omega - \omega_0)^2 + c.c$$

(2.19)

And [2.14]

$$\beta_m = (\frac{d^m\beta}{d\omega^m})_{\omega=\omega_0} \quad ,(m = 0, 1, 2, ...)$$

The group velocity is [2.6]

$$V_g = \frac{d\omega}{d\beta} = \frac{1}{\beta_1}$$

(2.20)

Considering a light pulse traveling in an optical fiber, each component of the pulse has

its own inverse group velocity $\frac{1}{V_g}$, over the width of the spectrum $\Delta\omega$ [2.6]

$$\Delta\left(\frac{1}{V_g}\right) = \frac{d^2\beta}{d\omega^2}\Delta\omega$$

(2.21)

After traveling a distance l, the pulse width is shifter by [2.6]

$$\Delta\tau = \Delta\left(\frac{1}{V_g}\right)l = \frac{d^2\beta}{d\omega^2}\Delta\omega l = \beta_2 l\Delta\omega = Dl\Delta\lambda$$

(2.22)

Where $D(\lambda) = \beta_2\frac{\Delta\omega}{\Delta\lambda} = \beta_2\frac{d\omega}{d\lambda} = -\frac{2\pi c}{\lambda^2}\beta_2$ is the GVD parameter [2.14].

(2.23)

The unit for D is usually $\frac{ps}{nm\cdot km}$, which can be considered as after traveling several kilometers, the pulse width of wavelength with nanometers difference gets shifted by several picoseconds.

In Eq. 2.23, if $\beta_2 > 0$, then $D < 0$, we call it a normal dispersion. When normal dispersion happens, light with longer wavelength travels faster. On the contrary, for the case $\beta_2 < 0$ and $D > 0$, we call it an anomalous dispersion and light with shorter wavelength travels faster.

When $D(\lambda_{ZD}) = 0$, we considered it a zero dispersion, where λ_{ZD} is the zero dispersion wavelength [2.15]. For common used telecommunication optical fiber, λ_{ZD} is 1.31μm. Light with such wavelength can be generated by InGaAsP laser diodes.

Now we consider the wave equation. If the envelope of a general has the form [2.14]

$$A(z,t) = \sqrt{P_0}e^{-2\alpha z}U(z,t)$$

(2.24)

where P_0 is the peak power of the pulse, α is the attenuation constant of the fiber, and $U(z,t)$ is the normalized amplitude of the pulse.

Then we introduce the time scale τ normalized by the pulse width T_0 [2.14]

$$\tau = \frac{t - {}^z\!/V_g}{T_0}$$

(2.25)

Assuming the wave is propagating under fundamental-mode operation and slow-varying envelope approximation, the wave equation can be showed as follows [2.14]

$$i\frac{\partial u}{\partial z} = \frac{sgn(\beta_2)}{2L_D}\frac{\partial^2 U}{\partial \tau^2}$$

(2.26)

where $sgn(\beta_2)$ is the sign of β_2, and

$$L_D = \frac{T_0{}^2}{|\beta_2|}$$

(2.27)

is the dispersion length. If the length of the fiber is greater than or close to L_D, then the GVD effect can't be ignored.

2.3.2 Nonlinearity and higher order dispersion

As we mentioned before, nonlinear optical effects can be observed under strong light

intensity. The intensity I can be simply described by

$$I = \frac{P}{A}$$

(2.28)

where P is the power, and A is the cross-sectional area.

This feature can be applied to nonlinear optical microscopy by using a pulsed laser which provides high instantaneous power and an objective of which the focused spot area is tiny. Thus the intensity near the focus is temporally and spatially high enough to generate the nonlinear signal.

Besides GVD, there still exists some other factors may distort the pulse. If we use an optical fiber to transmit the laser pulse, nonlinear effects will happen inside the fiber since the mode area of common single mode fibers (SMF) is very small. Therefore we have to consider the influence of the nonlinearity to the pulse. Higher order dispersion such as the third-order dispersion (TOD) should also be introduced [2.12, 2.16-2.17], if the pulse width is in the order of femtoseconds [2.11, 2.16-2.17], whereas the previously discussed GVD considers only to the picoseconds scale.

Fortunately, due to the symmetry of the structure in SiO_2, which is a common used component to manufacture optical fibers ,the second-order susceptibility $\chi^{(2)}$ vanishes. So we only have to discuss the nonlinear contribution due to the third-order susceptibility $\chi^{(3)}$.

The phase-matching [2.8-2.9] condition plays a crucial role in generating nonlinear

signals. It is based on the momentum conservation. According to this, we can neglect the part of THG and four wave mixing (4WM) because phase-matching conditions of these are not automatically reached in the fiber [2.14]. So we only have to consider the part of self-phase modulation (SPM) [2.14], cross-phase modulation (XPM) [2.14], stimulated Raman scattering (SRS) [2.14], and stimulated Brillouin scattering (SBS) [2.14].

SPM and XPM are both considered as optical Kerr effect, in which a variation of refractive index induced by the field thus leads to the phase shift. The difference between them is: SPM is induced by its own field while XPM is induced by another one. For SRS and SBS, they're describing the phenomena an optical pulse transferring its energy to the vibrational mode of the fiber with optical phonons and acoustic phonons respectively.

Only SPM and XPM contribute to the phase shift, whereas SRS and SBS don't. We only consider the influence of SPM here because there are no other fields to induce XPM. It provides the phase shift [2.14]

$$\Delta\phi = n_2|E|^2 k_0 l = \frac{2\pi n_2|E|^2 l}{\lambda}$$

(2.29)

where l is the fiber length, I_0 is the peak intensity of the pulse, and n_2 is the nonlinear refractive index coefficient

And the wave equation in Eq. 2.26 should be modified as [2.14]

25

$$i\frac{\partial u}{\partial z} = \frac{sgn(\beta_2)}{2L_D}\frac{\partial^2 U}{\partial \tau^2} - \frac{e^{-\alpha z}}{L_{NL}}|U|^2 U$$

(2.30)

and

$$L_{NL} = \frac{cA_{eff}}{n_2 P_0 \omega_0}$$

(2.31)

where A_{eff} is the effective mode area of the optical pulse in the fiber, and c is the speed of light

L_{NL} is the nonlinear length and it plays a similar role just like L_D to evaluate if the nonlinear effect can be neglected or not for different l.

Further, after considering the TOD with SPM together, the final modification of the critical length should be [2.16]

$$L_C = (\frac{e}{(4\pi)^2\sqrt{\ln 2}})^{1/3}(\frac{\lambda_0^2 A_{eff}^2}{|\beta_3|(n_2 P_0)^2})^{1/3}T_o$$

(2.32)

where $\beta_3 = (\frac{d^3\beta}{d\omega^3})_{\omega=\omega_0}$

Now we can estimate the influence from both SPM and TOD.

Reference

[2.1]   P. N. Prasad, *Introduction to Biophotonics* (Wiley, 2003).

[2.2]   M. Born and E. Wolf, *Principles of Optics* (Pergamon,1975).

[2.3]   E. Hecht, *Optics* (Addison Wesley, 2002)

[2.4]   R. Guenter, *Modern Optics* (Wiley,1990)

[2.5]   R. F. Fischer, B. Tadic, *Optical system design* (McGtaw-Hill, 2000).

[2.6]   H. A. Haus, *Wave and fields in optoelectronics* (Prentice-Hall, 1984)

[2.7]   J. A. Armstrong, N. Bloembergen, J. Ducuing, P. S. Pershan, "Interactions between Light Waves in a Nonlinear Dielectric," *Phys. Rev.* **127**, pp. 1918–1939 (1962).

[2.8]   R. W. Boyd, *Nonlinear optics* (Academic, 1992)

[2.9]   Y.-R. Shen, *The principles of nonlinear optics* (Wiley,1984)

[2.10]   P. Weinberger, "John Kerr and his Effects Found in 1877 and 1878," *Philosophical Magazine Letters* **88** (12), pp. 897–907

[2.11]   S. Feng, H. G. Winful, "Physical origin of the Gouy phase shift," *Optics Letters* **26** (8), pp. 485-487 (2001).

[2.12]   D. Débarre, N. Olivier, and E. Beaurepaire, "Signal epidetection in third-harmonic generation microscopy of turbid media," *Optics Express* **15** (14), pp. 8913-8924 (2007).

[2.13]   E. G. Sauter, *Nonlinear Optics* (John Wiley & Sons).

[2.14]   G. P. Agrawal, *Nonlinear fiber optics* (Academic, 2007).

[2.15]   D. Derickson, *Fiber optic test and measurement* (Prentice Hall, 1998).

[2.16]   J. Schütz, W. Hodel, and H.P. Weber, "Nonlinearpulse distortion at the zero dispersion wavelength of an optical fibre," *Optics Communications* **95** (4–6), pp. 357–365 (1993).

[2.17]   V. P. Yanovsky and F. W. Wise, "Nonlinear propagation of high-power, sub-100-fs pulses near the zero-dispersion wavelength of an optical fiber," *Optics Letters*. **19** (19), pp. 1547-1549 (1994).
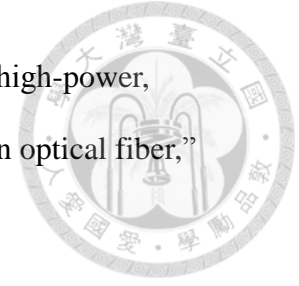
Chapter 3 Nonlinear optical microscopy

3.1 Basic components of a nonlinear optical microscope

The microscopy using pulsed laser as the illumination source to conduct nonlinear optical mechanism is considered as the nonlinear optical microscopy. A nonlinear optical microscope system usually consists of three parts: the pulsed laser, the optical component (mirrors, lenses, and the microscope), and the scanning mechanism.

Unlike the traditional wide-field optical microscope, an additional scanner is necessary for the microscope to scan over all the field of view, thus we can get a complete image. It is due to the mechanism of nonlinear optical microscopy, which nonlinear signal can only be generated near the focus. Thus the scanning speed also decides the image acquisition time, or the so-called "frame rate". Microscopy connected to scanning is called laser scanning microscopy (LSM).

3.1.1 Pulsed laser

Pulsed laser is the key to conduct nonlinear optical microscopy. It provides high peak intensity so the nonlinear effect could be occurred, whereas its average power is still low to prevent the risk of damage.

Since the first functioning laser was invented by Theodore Maiman in 1960 [3.1], many techniques related to it were also developed. There are two major ways to operate the laser. If the output power of the laser is constant over time, we say it is under the continuous wave (CW) operation. On the other hand, if the output separate on different

time interval, then we regard it under the pulsed operation. Furthermore, the pulsed operation can be categorized into Q-switching [3.2] or mode-locking [3.3] depending on the pulse width of the output laser.
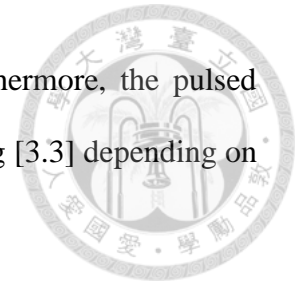
The abbreviation Q represents the quality factor which means to what extent an oscillator is under damping. In a Q-switching laser, an attenuator is installed inside the laser cavity. The attenuator is variable and can control the Q factor. When the Q factor is reduced, the pump energy stores in the gain medium. After the factor is restored, the lasing begins with the previous accumulated energy. By repeating above steps, then the discontinuous and pulsed laser is generated. Typically the pulse width can be compressed to several 10 ns by this method. The theory of Q-switching is first proposed in 1958 [3.2] and demonstrated in 1962 [3.4].

Even shorter pulse width can be reached if we can control the coherence of all different oscillation modes inside the cavity. The technique how to modulate all modes and make them interfering with one another constructively is known as "mode-locking". The method using external signal to induce modulations is active mode-locking [3.5], whereas passive mode-locking [3.6] installs certain element to induce self-modulations.

Common methods for active mode-locking are amplitude modulation (AM) [3.7], frequency modulation (FM) [3.7], or synchronous mode-locking which the laser is directly pumped by another mode-locked laser. Saturable absorber mirrors (SAM) [3.8] and Kerr-lenses [3.9] are the common objects used for passive mode-locking.
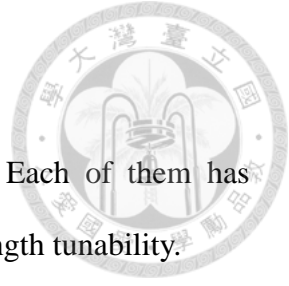
3.2 Selection of the light source

Various kinds of pulsed laser are available for the light source. Each of them has different features, for example: type, central wavelength and wavelength tunability.

Central wavelength is the most important feature. First, it's directly related to the photon energy, since $E = h\nu = h\frac{c}{\lambda}$. The higher the photon energy is, the easier the damage may cause when single or multi photon fluorescence occurs since the process during the emission of fluorescence concerning real state absorption of the photon by an electron. So if we use longer wavelength light for illumination, the power threshold of the damage could be raised. An excitation "window" [3.10-3.14], which is a wavelength band relatively safer for exposure, is located around the range of near infrared (NIR). Another importance of the central wavelength is its corresponding emission nonlinear signal. For example, for SHG and THG, the emission wavelength is its 1/2 and 1/3 of the excitation wavelength respectively. Thus we can choose the appropriate excitation wavelength, as long as the emission signal can be easily collected. Generally, the emission wavelength locates among the range of visible lights is especially expected. Those which locate in the deep ultraviolet part will suffer strong attenuation in organisms due to the strong absorption by water.

There are many kinds of fluorescent materials and dyes, and each of them has its own intrinsic excitation wavelength. Since it's related to the real state energy transition between fixed energy levels, the transition energy and the corresponding excitation wavelength are also fixed. Therefore, only the laser whose central wavelength covers the excitation band can be the excitation source for single or multi photon fluorescence

excitation. Unlike harmonic generations (HG), the selection of excitation wavelength for florescence meets more restrictions.

3.3 Common light source

We have tested three kinds of different laser as our light source. Two of them are solid state lasers, and another one is fiber-based. Each of them has different central wavelength and tunable range.

3.3.1 Ti:sapphire laser

"Ti:sapphire" ,which acts as the laser gain medium, is actually the name of a kind of crystal--sapphire (Al_2O_3) doped with titanium ions. First constructed in 1982 [3.15], it is famous for its wide tunable range (from about 700 nm to 1100 nm) and is able to generate ultra-short pulses. By incorporating an optical parametric oscillator (OPO) [3.16], the wavelength range can be even extended, but the complexity and the cost also increase. The wide tunable wavelength covers many of the excitation wavelengths of two-photon fluorescence. With these advantages, Ti:sapphire laser is the most popular commercial solid-state mode-locked laser, and is widely used as the light source of nonlinear optical microscopy, such as two photon fluorescence microscopy (2PFM) or harmonic generation microscopy (HGM).

However, it's not suitable for all kinds of higher HG. Since the wavelength of its THG located in the range of deep ultraviolet (wavelength < 300 nm), which suffers strong attenuation in organisms by the absorption of water, not all kinds of HG can be easily collected. Only part of the SHG (wavelength between 350 nm and 550 nm), which overlaps the range of visible lights (wavelength between 350 nm and 750 nm), is

available. Thus, the common application of Ti:sapphire laser in nonlinear optical microscopy is to excite SHG or 2PF.
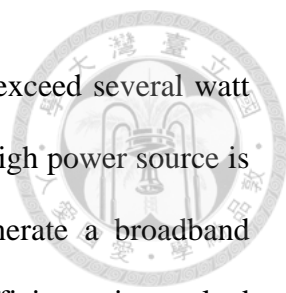
3.3.2 Cr:forsterite laser

Similar to "Ti:sapphire", "Cr:forsterite" [3.17] is the name of another kind of laser gain medium crystal---forsterite (Mg_2SiO_4) doped with chromium ions. Its central wavelength locates around 1230 nm. Although it's not tunable and the crystal has a lower gain and poorer thermal property [3.18] in comparison with the Ti:Sapphire crystal. The THG of Cr:forsterite lasers can be easily collected in comparison with the one excited by Ti:sapphire lasers. Since the wavelength of its THG no longer locates in the range of ultraviolet, no strong attenuation and absorption by water will be encountered anymore. Thus, both SHG (wavelength 615 nm) and THG (410 nm wavelength) signals can be collected easily.

Besides an extra order HG signal for observation, another advantage of Cr:forsterite lasers is the high tolerance of the illumination power. Exposure to the excitation light with over 100 mW average power is allowed without damage due to the lower photon energy of 1230 nm wavelength.

3.3.3 Yb fiber laser

The last kind of laser we used is a Ytterbium (Yb)-doped fiber laser [3.19], whose central wavelength locates around 1030 nm. This fiber-based laser provides more flexibility and has some advantages over a solid-state laser, including the smaller size, the maximum power, the higher electrical-to-optical conversion efficiency, and the reliability. Since there has no crystal used and no concerning thermal effect (heat

dissipation capability [3.20]), the average output power can easily exceed several watt by an amplifier. Though the central wavelength is not tunable, this high power source is suitable for optical parametric amplification (OPA) [3.21] to generate a broadband tunable light source. The higher electrical-to-optical conversion efficiency is resulted from the fine mode confinement in fibers and the single-stage conversion (980 nm laser diodes to 1030 nm Yb fiber laser). The reliability is due to the fiber has less sensitivity to temperature and humidity.

3.4 Miniaturization of the nonlinear optical microscope

In the beginning, scanners are directly integrated with an already available microscope to conduct the nonlinear optical microscopy. The method is simple, but the appended scanner would make the whole system even bulkier. Since the technique related to these integrated microscope systems have been developed these years, the system is improved in many aspects such as: the field of view (FOV), the resolution, the scanning speed of the system, and the miniaturization of the total size. These improvements bring the system more flexibility and mobility. Thus, it's possible that the nonlinear optical microscopy can not only be applied in the laboratory but also in the hospital.

In the recent ten years, some groups have worked on the miniaturization of the system [3.22-3.57]. In order to miniaturize the system, the scanner and the imaging head are usually integrated into an endoscope. Optical fibers are widely used to transmit the light from the source to the scope, so the size of the laser source can be ignored. Thus, GRIN lenses and optical fibers are commonly used in an endoscope.

3.4.1 GRIN lens

Gradient-index (GRIN) lens is widely used in the miniaturized endoscope [3.22, 3.26-3.29, 3.32-3.45, 3.47-3.49, 3.51-3.54]. Since it is produced by a gradually varied refractive index material, it can converge light and act as an objective even though its surface is flat.
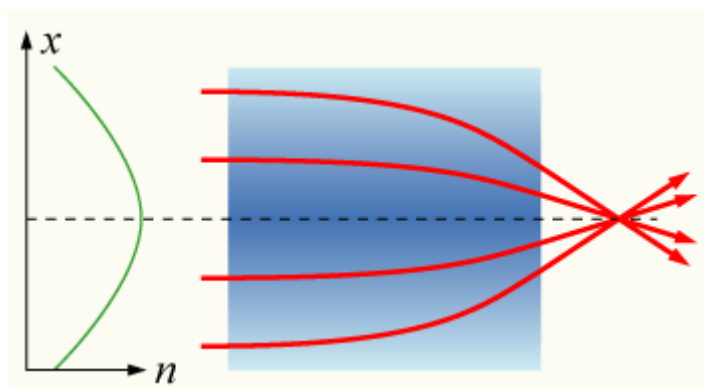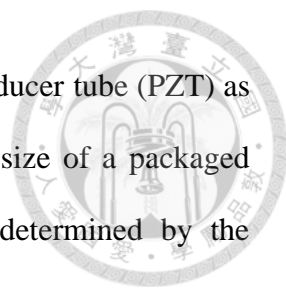
Fig 3.1 Gradually varied refractive index feature of a GRIN lens.

GRIN lens could be fabricated in a very small size just like a thin needle (the so-called "GRIN rod"), which includes three parts: the coupling lens, the relay lens, and the objective lens. The coupling lens is for the light coupling from the original objective to the GRIN lens. The relay lens decides the whole length of the GRIN rod. The objective lens can be regarded as the extension of the original objective. The easiest way to apply the GRIN lens is directly attaching it to the tip of an objective [3.26, 3.29, 3.36-3.37, 3.41-3.43], so the imaging head thus becomes a thin probe. By using a fiber bundle to join the objective and the GRIN lens together [3.32-3.33], the imaging head could be mobile. However, the resolution is also restricted to the number of fiber in the bundle, and some missing points might appear in the FOV.

Due to the flat surface feature of GRIN lens, it could be directly mounted or fused to an

optical fiber. Combining with optical fibers and a piezoelectric transducer tube (PZT) as the scanner [3.27-3.28, 3.34-3.35, 3.38, 3.46-3.47, 3.51-3.54], the size of a packaged endoscope could be very small. The image acquisition rate is determined by the scanning speed of PZT, which are usually under 10/s.

There's a small problem for the GRIN lens. It suffers more chromatic aberration than the usual lens, which leads to a reduction to the signal collection efficiency. It is due to the wavelength difference between the excitation light and the emitted nonlinear signal, so a slight shift of the focus of the objective would happen. A method to deal with the focus shift problem is to use double-clad fibers (DCF) [3.27, 3.46, 3.52-3.58], which are composed of three layers in order to guide the excitation light and the emission signal into different layer respectively.

3.4.2 Optical fiber

Optical fibers are known for their flexibility. They could be a very suitable tool for light transmission in the miniaturized system, including the excitation source delivering and the collection of the signal [3.22-3.23, 3.25, 3.27-3.28, 3.30-3.35, 3.38-3.40, 3.44-3.58]. However, pulsed laser will suffer strong spectrum broadening and pulse distortion due to the self-phase modulation (SPM) [3.59], one kind of nonlinear optical effects in single mode fibers (SMF) we've mentioned in chapter 2. This effect not only lowers the peak intensity but also lengthens the pulse width of the incidence, which will reduce the efficiency generating nonlinear signals. Thus, optical fibers with different structure, such as multimode fibers (MMF) [3.60], large-mode area (LMA) fibers [3.61-3.62], or photonic crystal fibers (PCF) [3.63], are introduced in order to maintain the pulse quality during the transmission.
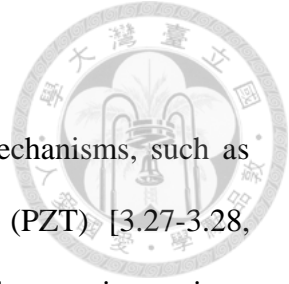
3.4.3 Mini scanner

Various kinds of scanner is applied in LSM based on different mechanisms, such as galvano mirror, resonant scanner, piezoelectric transducer tube (PZT) [3.27-3.28, 3.30-3.31, 3.34-3.35, 3.38, 3.46-3.47, 3.50-3.58], and MEMS scanning mirror [3.22-3.25, 3.39-3.40, 3.44-3.45, 3.48-3.49]. The latter two are usually used in the miniaturized system especially.

As mentioned before, PZT is usually combined with GRIN lens and applied in a miniaturized fiber endoscope [3.27-3.28, 3.34-3.35, 3.38, 3.46-3.47, 3.51-3.54]. Its dimension is really small, but the scanning speed is not very fast so far, so only low frame rate could be reached. Micro-electro mechanical system (MEMS) mirror is a kind of mini resonant scanner. Its size is only a little bit larger than PZT, and can provide relatively higher scanning speed. On the other hand, it's also cheap, thus it's chosen as the scanner in our nonlinear optical microscope to meet the demand for miniaturized size and high frame rate [3.22-3.25, 3.40].

3.5 Comparison between different miniaturized systems

This section lists the performance of the miniaturized system done by different groups [3.22-3.57], including the field of view (FOV), the lateral resolution, the axial resolution, the numerical aperture (NA) of the objective lens, the working distance (WD), the penetration depth, the frame rate, and the method. The length unit of FOV, resolution, WD, and penetration depth is μm.

No.	From	Year	FOV	NA
1	Adela Ben-Yakar	2008	36~310 in diameter	0.46
2		2011	142×297	0.55
3	Chi-Kuang Sun	2008	70×76	0.9 (water)
4		2010	70×100	1.2 (water)
5	Chris Xu	2010	150~1000 in extent	0.18 or 0.5
6		2011	110 in extent	0.8 (water)
7	Eric Seibel	2008	up to 200 in diameter	0.5
8	Fabio Mammano	2011	80 in extent	0.4~0.75
9	Fritjof Helmchen	2001	65 in extent	0.8 (water)
10		2002	100 in extent	N/A
11		2004	up to 800 in diameter	0.5
12	Joachim Knittel	2001	up to 280 in extent	0.5
13	K. König	2008	up to 420 in extent	0.65
14		2009	up to 420 in extent	0.65
15	Mark J. Schnitzer	2003	up to 211 in diameter	0.46, 0.42, 0.26
16		2004	at least 166 in extent	0.47, 0.46, 0.38
17		2005	145~215 in extent	0.48
18		2007	up to 80×20	0.46
19		2009	up to 295×100	0.58
20		2009	at least 40 in extent	0.82
21			275 in extent	0.49
			130 in extent	0.48
			75 in extent	0.45
		2010	700 in extent	0.49
			350 in extent	0.47
			120 in extent	0.65
			75 in extent	0.82
22	Michael J. Levene	2012	>120 in extent	0.6
23	Min Gu	2006	at least 111 in extent	0.5
24		2007	at least 147×85	0.6
25		2008	up to 475×475	0.35
26	Robert J. Gordon	2010	at least 150 in diameter	N/A
27	Shuo Tang	2008	at least 91×91	0.62
28		2009	up to ~200 in extent	0.62

29	Winfried Denk	2007	up to ~250 in extent	0.9 (water)
30	Xingde Li	2006	up to 120~220 in diameter	0.46
31		2009	up to ~320 in diameter	N/A
32		2009	120 in diameter	0.5
33		2010	150 in diameter	N/A
34		2011	110 in diameter	0.8
35		2012	~100 in diameter	N/A
36		2012	~100 or 150 in diameter	0.8
37		2012	110 in diameter	~0.7

Table 3.1 System comparison of FOV and NA

The size of the FOV is related to the optical design of the system, including the alignment of the lens and the scanning angle of the scanner. Most of the example have a range between 100~200 μm in extent or diameter. However, the FOV shrinks anyway as the improvement in NA for better resolution.
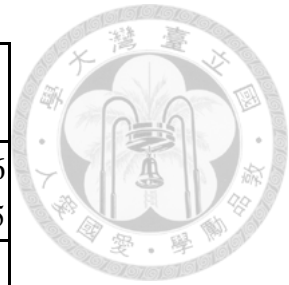
No.	Lateral Resolution	Axial Resolution	WD	NA
1	1.64±0.09	16.4±1.0	210	0.46
2	1.27±0.03	13.5±0.54	880	0.55
3	<1	N/A	N/A	0.9 (water)
4	0.4	N/A	N/A	1.2 (water)
5	0.976	N/A	N/A	0.18 or 0.5
6	0.8	9.4	135	0.8 (water)
7	~1	N/A	300 (water)	0.5
8	0.9~1.2	10~12	150~800	0.4~0.75
9	N/A	N/A	>1.5 mm	0.8 (water)
10	N/A	N/A	N/A	N/A
11	>4	N/A	300	0.5
12	3.3	N/A	N/A	0.5
13	0.6	5.8	170 (water), 95 (air)	0.65
14	x=1.08,y=0.67	5.8	170 (water), 95 (air)	0.65
15	1.26±0.1	N/A	300, 300, 800	0.46, 0.42, 0.26
16	0.86±0.07	N/A	130, 390, 1040	0.47, 0.46, 0.38
17	1.21±0.04	9.8±0.5	250	0.48
18	N/A	N/A	400	0.46
19	1.29±0.05	10.3±0.3	280	0.58
20	1.0±0.2	4.4±0.2	230	0.82
21	0.9		250	0.49
	1			0.48
	1.2			0.45
	0.9	N/A		0.49
	1			0.47
	0.8			0.65
	0.6			0.82
22	0.618	5.5	150 (water)	0.6
23	N/A	5.4	150	0.5
24	N/A	~10	200	0.6
25	~1	~14.5	N/A	0.35
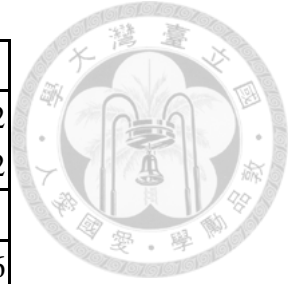
26	1.5	9.2	420	N/A
27	N/A	N/A	N/A	0.62
28	~2	N/A	N/A	0.62
29	0.9±0.1	N/A	700	0.9 (water)
30	2±0.2	~20	~900	0.46
31	~1.6	~11.4	N/A	N/A
32	N/A	N/A	650	0.5
33	N/A	N/A	N/A	N/A
34	N/A	N/A	~200	0.8
35	N/A	N/A	200 (water)	N/A
36	~1.2	~5.7	200	0.8
37	~0.7	~6	N/A	~0.7

Table 3.2 System comparison of resolution, WD, and NA

In table 3.2, most of the lateral resolution is around 1 µm, and the axial resolution is about 5~10 times as the lateral resolution. The resolution tends to be improved while objectives with higher NA used. However, the WD is thus shortened.

No.	Frame Rate	Penetration Depth	Method	Reference
1	10	210	MEMS+GRIN+fiber	[3.22]
2	7	N/A	MEMS+aspheric lens+fiber	[3.23]
3	24	N/A	MEMS+objective	[3.24]
4	31	>200	MEMS+objective+fiber	[3.25]
5	1	N/A	Galvo+lens package	[3.26]
6	4.1	>70	PZT+GRIN+DCF	[3.27]
7	25	N/A	PZT+GRIN+fiber	[3.28]
8	N/A	N/A	only GRIN as the objective	[3.29]
9	2	~250	PZT+objective+fiber	[3.30]
10	N/A	N/A	PZT+objective+fiber	[3.31]
11	N/A	1000	Objective+GRIN+fiber bundle	[3.32]
12	N/A	N/A	Objective+GRIN+fiber bundle	[3.33]
13	2.6	N/A	PZT+GRIN+fiber	[3.34]
14	6	N/A	PZT+GRIN+fiber	[3.35]
15	N/A	N/A	Objective+GRIN	[3.36]
16	<3	270	Objective+GRIN	[3.37]
17	2	N/A	PZT+GRIN+fiber	[3.38]
18	N/A	N/A	MEMS+GRIN+fiber	[3.39]
19	1~15	N/A	MEMS+GRIN+fiber	[3.40]
20	N/A	N/A	GRIN	[3.41]
21				[3.42]
	1~5	N/A	Objective+GRIN	
22	N/A	800	Objective+GRIN	[3.43]
23	N/A	N/A	MEMS+GRIN+fiber	[3.44]
24	N/A	100	MEMS+GRIN+fiber	[3.45]
25	2.6	>60, up to 250	PZT+custom design lens+DCF	[3.46]
26	1.1	>20	PZT+GRIN+fiber	[3.47]
27	N/A	N/A	MEMS+GRIN+fiber+aspheric lens	[3.48]

28	0.25	N/A	MEMS+GRIN+fiber+aspheric lens	[3.49]
29	N/A	N/A	PZT+objective+fiber	[3.50]
30	2.6	N/A	PZT+GRIN+fiber	[3.51]
31	3.3	at least 120	PZT+GRIN+fiber+DCF	[3.52]
32	3	N/A	PZT+GRIN+aspheric lens+DCF	[3.53]
33	~3	at least 64	PZT+GRIN+aspheric lens+DCF	[3.54]
34	2.6	at least ~150	PZT+aspheric lens+DCF	[3.55]
35	1.9	N/A	PZT+miniature objective+DCF	[3.56]
36	~3	N/A	PZT+aspheric lens+DCF	[3.57]
37	~3	N/A	PZT+microlens+DCF	[3.58]
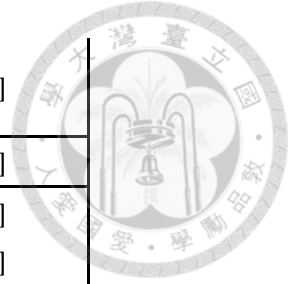
Table 3.3 System comparison of frame rate, penetration, and method

In table 3.3, we can find that the image acquisition speed for most of the miniaturized

system so far is not very high, only some designs can approach the video rate [3.3, 3.6].
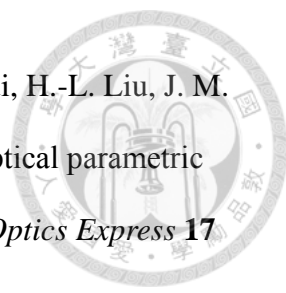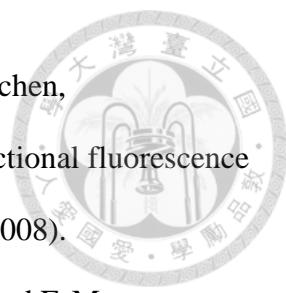
Reference

[3.1]   T. H. Maiman, "Stimulated Optical Radiation in Ruby," *Nature* **187**, pp. 493-494 (1960).

[3.2]   N. Taylor, *LASER: The inventor, the Nobel laureate, and the thirty-year patent war* (Simon & Schuster, 2000).

[3.3]   W. E. Lamb, Jr., "Theory of an optical laser," *Phys. Rev.* **134**, pp. 1429-1450 (1964).

[3.4]   F. J. McClung and R. W. Hellwarth, "Giant Optical Pulsations from Ruby," *Applied Optics* **1** (1), pp. 103-105 (1962).

[3.5]   L. E. Hargrove, R. L. Fork, and M. A. Pollack, "Locking of He-Ne laser modes induced by synchronous intracavity modulation," *Appl. Phys. Letters* **5**, pp. 4-5 (1964).

[3.6]   H. W. Mocker and R. J. Collins, "Mode competition and self-locking effects in a Q-switched ruby laser," *Appl. Phys. Lett*. **7**, pp. 270–273 (1965).

[3.7]   D. J. Kuizenga and A. E. Siegman, "FM and AM mode locking of the homogeneous laser – Part I: theory," *IEEE J. Quantum Electron.* **6**, pp. 694-708 (1970).

[3.8]   A. J. DeMaria, D. A. Stetser, and H. Heynau, "Self mode-locking of lasers with saturable absorbers," *Appl. Phys. Lett*. **8**, pp. 174 (1966).

[3.9]   D. E. Spence, P. N. Kean, and W. Sibbett, "60-fsec pulse generation from a self-mode-locked Ti:sapphire laser," *Optics Letters* **16** (1), pp. 42-44 (1991).

[3.10]   P. C. Cheng, S. J. Pan, A. Shih, K. S. Kim, W. S. Liou and M. S. Park, "Highly efficient upconverters for multiphoton fluorescence microscopy," *Journal of Microscopy* **189**: 199–212 (1998).

[3.11]   M.-C. Chan, T.-M. Liu, S.-P. Tai, and C.-K. Sun, "Compact fiber-delivered
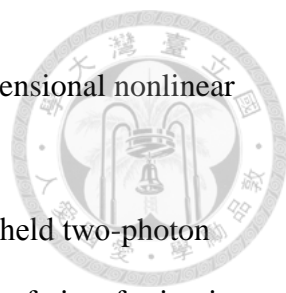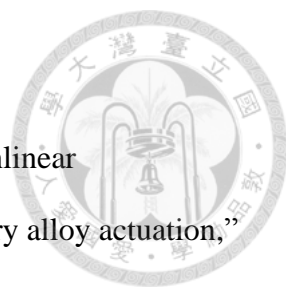
Cr:forsterite laser for nonlinear light microscopy," *Journal of Biomedical Optics* **10** (4) 054006 (2005).

[3.12]   S.-W. Chu, I.-H. Chen, T.-M. Liu, C.-K. Sun, S.-P. Lee, B.-L. Lin, P.-C. Cheng, M.-X. Kuo, D.-J. Lin, and H.-L. Liu, "Nonlinear bio-photonic crystal effects revealed with multimodal nonlinear microscopy," *Journal of Microscopy* **208** (3), pp. 190–200 (2002).

[3.13]   R. R. Anderson and J. A. Parrish, "The Optics of Human Skin," *Journal of Investigative Dermatology* **77**, pp. 13–19 (1981).

[3.14]   T. Vo-Dinh, *Biomedical photonics handbook* (CRC Press, 2003).

[3.15]   P. F. Moulton, "Spectroscopic and laser characteristics of Ti:Al$_2$O$_3$," *JOSA B* **3** (1), pp. 125-133 (1986).

[3.16]   J. A. Giordmaine and Robert C. Miller, "Tunable Coherent Parametric Oscillation in LiNbO3 at Optical Frequencies," *Phys. Rev. Lett*. **14** (24), pp. 973–976 (1965).

[3.17]   V. Petricevic, "Laser action in chromium-doped forsterite," *Appl. Phys. Lett*. **52** (13), pp. 1040-1042 (1988).

[3.18]   A. Agnesi, E. Piccinini, G.C. Reali, "Influence of thermaleffects in Kerr-lens mode-locked femtosecond Cr4+:forsterite lasers," *Optics Communications* **135**, Issues (1–3), pp. 77–82 (1997).

[3.19]   C. Hönninger, R. Paschotta, M. Graf, F. Morier-Genoud, G. Zhang, M. Moser, S. Biswal, J. Nees, A. Braun, G.A. Mourou, I. Johannsen, A. Giesen, W. Seeber, and U. Keller, "Ultrafast ytterbium-doped bulk lasers and laser amplifiers," *Applied Physics B: Lasers and Optics* **69** (1), pp. 3-17 (1999).

[3.20]   W. F. Krupke, "Ytterbium solid-state lasers. The first decade," *IEEE J. Sel. Top. Quantum Electron.* **6** (6), pp.1287-1296 (2000).
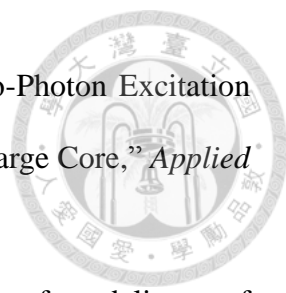
[3.21]   Y.-W. Tzeng, Y.-Y. Lin, C.-H. Huang, J.-M. Liu, H.-C. Chui, H.-L. Liu, J. M. Stone, J. C. Knight, and S.-W. Chu, "Broadband tunable optical parametric amplification from a single 50 MHz ultrafast fiber laser," *Optics Express* **17** (9), pp. 7304-7309 (2009).

[3.22]   C. L. Hoy, N. J. Durr, P. Chen, W. Piyawattanametha, H. Ra, O. Solgaard, and A. Ben-Yakar, "Miniaturized probe for femtosecond laser microsurgery and two-photon imaging," *Optics Express* **16** (13), pp. 9996-10005 (2008).

[3.23]   C. L. Hoy, O. Ferhanoğlu, M. Yildirim, W. Piyawattanametha, H. Ra, O. Solgaard, and A. Ben-Yakar, "Optical design and imaging performance testing of a 9.6-mm diameter femtosecond laser microsurgery probe," *Optics Express* **19** (11), pp. 10536-10552 (2011).

[3.24]   T.-M. Liu, M.-C. Chan, I.-H. Chen, S.-H. Chia, and C.-K. Sun, "Miniaturized multiphoton microscope with a 24Hz frame-rate," *Optics Express* **16** (14), pp. 10501-10506 (2008).

[3.25]   S.-H. Chia, C.-H. Yu, C.-H. Lin, N.-C. Cheng, T.-M. Liu, M.-C. Chan, I-H. Chen, and C.-K. Sun, "Miniaturized video-rate epi-third-harmonic- generation fiber-microscope," *Optics Express* **18** (16), pp. 17382-17391 (2010).

[3.26]   M. Chen, C. Xu, and W. W. Webb, "Endoscope Lens with Dual Field of View and Resolution for Multiphoton Imaging," *Optics Letters* **35** (16), pp. 2735-2737 (2010).

[3.27]   D. R. Rivera, C. M. Brown, D. G. Ouzounov, I. Pavlova, D. Kobat, W. W. Webb, and C. Xu, "Compact and flexible raster scanning multiphoton endoscope capable of imaging unstained tissue," *Proceedings of the National Academy of Sciences of the United States of America* **108** (43), pp. 17598-17603 (2011).

[3.28]   C. J. Engelbrecht, R. S. Johnston, E. J. Seibel, and F. Helmchen, "Ultra-compact fiber-optic two-photon microscope for functional fluorescence imaging in vivo," *Optics Express*l **16** (8), pp. 5556-5564 (2008).

[3.29]   F. Bortoletto1, C. Bonoli1, P. Panizzolo, C. D. Ciubotaru, and F. Mammano, "Multiphoton Fluorescence Microscopy with GRIN Objective Aberration Correction by Low Order Adaptive Optics," *PLoS ONE* **6** (7): e22321 (2011).

[3.30]   F. Helmchen, M. S. Fee1, D. W. Tank, and W. Denk, "A Miniature Head-Mounted Two-Photon Microscope: High-Resolution Brain Imaging in Freely Moving Animals," *Neuron* **31** (6), pp. 903–912 (2001).

[3.31]   F. Helmchena, and W. Denk, "New developments in multiphoton microscopy," *Current Opinion in Neurobiology* **12** (5), pp. 593-601 (2002).

[3.32]   W. Göbel, J. N. D. Kerr, A. Nimmerjahn, and F. Helmchen, "Miniaturized two-photon microscope based on a flexible coherent fiber bundle and a gradient-index lens objective," *Optics Letters* **29** (21), pp. 2521-2523 (2004).

[3.33]   J. Knittel, L. Schnieder, G. Buess, B. Messerschmidt, and T. Possner, "Endoscope-compatible confocal microscope using a gradient index-lens system," *Optics Communications* **188** (5–6), pp. 267–273 (2001).

[3.34]   R. Le Harzic, M. Weinigel, I. Riemann, K. König, and B. Messerschmidt, "Nonlinear optical endoscope based on a compact two axes piezo scanner and a miniature objective lens," *Optics Express* **16** (25), pp. 20588-20596 (2008).

[3.35]   R. Le Harzic, I. Riemann, M. Weinigel, K. König, and B. Messerschmidt, "Rigid and high-numerical-aperture two-photon fluorescence endoscope," *Applied Optics* **48** (18), pp. 3396-3400 (2009).

[3.36]   Juergen C. Jung and Mark J. Schnitzer, "Multiphoton endoscopy," *Optics Letters* **28** (11), pp. 902-904 (2003).

[3.37]   J. C. Jung, A. D. Mehta, E. Aksay, R. Stepnoski, and M. J. Schnitzer, "In Vivo Mammalian Brain Imaging Using One- and Two-Photon Fluorescence Microendoscopy," *Journal of Neurophysiology* **92** (5), pp. 3121-3133 (2004).

[3.38]   B. A. Flusberg, J. C. Jung, E. D. Cocker, E. P. Anderson, and M. J. Schnitzer, "In vivo brain imaging using a portable 3.9 gram two-photon fluorescence microendoscope," *Optics Letters* **30** (17), pp. 2272-2274 (2005).

[3.39]   E. D. Cocker, R. P. J. Barretto, J. C. Jung, B. A. Flusberg, H. Ra, O. Solgaard, and M. J. Schnitzer, "A Portable Two-photon Fluorescence Microendoscope Based on a Two-dimensional Scanning Mirror," *Optical MEMS and Nanophotonics, 2007 IEEE/LEOS International Conference*, pp. 6-7 (2007).

[3.40]   W. Piyawattanametha, E. D. Cocker, L. D. Burns, R. P. J. Barretto, J. C. Jung, H. Ra, O. Solgaard, and M. J. Schnitzer, "In vivo brain imaging using a portable 2.9 g two-photon microscope based on a microelectromechanical systems scanning mirror," *Opt Lett.* **34** (15), pp. 2309–2311 (2009).

[3.41]   R. P. J. Barretto, B. Messerschmidt, and M. J. Schnitzer, "In vivo fluorescence imaging with high-resolution microlenses," *Nature Methods* **6**, pp. 511 - 512 (2009).

[3.42]   R.P. Barretto, and M.J. Schnitzer, "In Vivo Optical Microendoscopy for Imaging Cells Lying Deep within Live Tissue," *Imaging: A Laboratory Manual* (Cold Spring Harbor Laboratory Press, 2011).

[3.43]   T. A. Murray, and M. J. Levene, "Singlet gradient index lens for deep in vivo multiphoton microscopy," *J. Biomed. Opt.* **17** (2), 021106 (2012).

[3.44]   L. Fu, A. Jain, H. Xie, C. Cranfield, and M. Gu, "Nonlinear optical endoscopy based on a double-clad photonic crystal fiber and a MEMS mirror," *Optics Express* **14** (3), pp. 1027-1032 (2006).

[3.45]   L. Fu, A. Jain, C, Cranfield, H. Xie, and M. Gu, "Three-dimensional nonlinear optical endoscopy," *J. Biomed. Opt.* **12** (4), 040501 (2007).

[3.46]   H. Bao, J. Allen, R. Pattie, R. Vance, and M. Gu, "Fast handheld two-photon fluorescence microendoscope with a 475 μm × 475 μm field of view for in vivo imaging," *Optics Letters* **33** (12), pp. 1333-1335 (2008).

[3.47]   Y. Zhao, H. Nakamura, and R. J. Gordon, "Development of a versatile two-photon endoscope for biological imaging," *Biomedical Optics Express* **1** (4), pp. 1159-1172 (2010).

[3.48]   W. Jung, S. Tang, D. T. McCormic, T. Xie, Y.-C. Ahn, J. Su, I. V. Tomov, T. B. Krasieva, B. J. Tromberg, and Z. Chen, "Miniaturized probe based on a microelectromechanical system mirror for multiphoton microscopy," *Optics Letter* **33** (12), pp. 1324-1326 (2008).

[3.49]   S. Tang, W. Jung, D. McCormick, T. Xie, J. Su, Y.-C. Ahn, B. J. Tromberg and Z. Chen, "Design and implementation of fiber-based multiphoton endoscopy with microelectromechanical systems scanning," *J. Biomed. Opt.* **14** (3), 034005 (2009).

[3.50]   J. Sawinskia and W. Denk, "Miniature random-access fiber scanner for in vivo multiphoton imaging," *Journal of Applied Physics* **102** (3), 034701 (2007).

[3.51]   M. T. Myaing, D. J. MacDonald, and X. Li, "Fiber-optic scanning two-photon fluorescence endoscope," *Optics Letters* **31** (8), pp. 1076-1078 (2006).

[3.52]   Y. Wu, Y. Leng, J. Xi, and X. Li, "Scanning all-fiber-optic endomicroscopy system for 3D nonlinear optical imaging of biological tissues," *Optics Express* **17** (10), pp. 7907-7915 (2009).

[3.53]   Y. Wu, J. Xi, M. J. Cobb, and X. Li, "Scanning fiber-optic nonlinear endomicroscopy with miniature aspherical compound lens and multimode fiber

collector," *Optics Letters* **34** (7), pp. 953-955 (2009).

[3.54]   Y. Wu, Y. Zhang, J. Xi, M.-J. Li, and X. Li, "Fiber-optic nonlinear endomicroscopy with focus scanning by using shape memory alloy actuation," *J. Biomed. Opt.* **15** (6), 060506 (2010).

[3.55]   K. Murari, Y. Zhang, S. Li, Y. Chen, M.-J. Li, and X. Li, "Compensation-free, all-fiber-optic, two-photon endomicroscopy at 1.55 μm," *Optics Letters* **36** (7), pp. 1299-1301 (2011).

[3.56]   W. Liang, K. Murari, Y. Zhang, Y. Chen, M.-J Li, and X. Li, "Increased illumination uniformity and reduced photodamage offered by the Lissajous scanning in fiber-optic two-photon endomicroscopy," *J. Biomed. Opt.* **17** (2), 021108 (2012).

[3.57]   J. Xi, Y. Chen, Y. Zhang, K. Murari, M.-J. Li, and X. Li, "Integrated multimodal endomicroscopy platform for simultaneous en face optical coherence and two-photon fluorescence imaging," *Optics Letters* **37** (3), pp. 362-364 (2012).

[3.58]   Y. Zhang, K. Murari, W. Liang, J. Xi, Y. Chen, M.-J. Li, Z. Bhujwalla, K.Glunte, and X. Li, "Scanning Nonlinear Endomicroscopy Technology for Intrinsic Imaging of Biological Tissues," *CLEO: Applications and Technology*, paper: ATh5A.1 (2012).

[3.59]   G. P. Agrawal, *Nonlinear fiber optics* (Academic, 2007).

[3.60]   M. E. Fermann, "Single-mode excitation of multimode fibers with ultrashort pulses," *Optics Letters* **23** (1), pp. 52-54 (1998).

[3.61]   D. G. Ouzounov, K. D. Moll, M. A. Foster, W. R. Zipfel, W. W. Webb, and A. L. Gaeta, "Delivery of nanojoule femtosecond pulses through large-core microstructured fibers," *Optics Letters* **27** (17), pp. 1513-1515 (2002).

[3.62]   F. Helmchen, D. W. Tank, and W. Denk, "Enhanced Two-Photon Excitation Through Optical Fiber by Single-Mode Propagation in a Large Core," *Applied Optics* **41** (15), pp. 2930-2934 (2002).

[3.63]   W. Göbel, A. Nimmerjahn, and F. Helmchen, "Distortion-free delivery of nanojoule femtosecond pulses from a Ti:sapphire laser through a hollow-core photonic crystal fiber," *Optics Letters* **29** (11), pp. 1285-1287 (2004).

[3.64]   R.E. Fischer, B. Tadic-Galeb, *Optical system design* (McGraw-Hill, 2000)

[3.65]   J. Squier, M. Müller, "High resolution nonlinear microscopy: A review of sources and methods for achieving optimal imaging," *Rev. Sci. Instrum.* **72**, pp. 2855-2867 (2001).

Chapter 4 Mini aspheric lens applied in the nonlinear optical microscope

4.1 Method of miniaturization

For convenient clinical application, we desire a nonlinear optical microscope imaging head with a miniaturized size, a large field of view (FOV), and a high frame rate. System with a miniaturized size provides convenience and flexibility rather than the traditional bulky microscope. Large FOV means more information can be revealed once simultaneously. At last, high frame rate can cope with the problem about inevitable small vibrations during the observation. The strategy how we achieve all these requirements is using a MEMS mirror as the scanner and a mini aspheric lens as the objective, and tube lens pairs with different beam magnification are used to control the FOV and the resolution.

Since the resonant oscillation frequency of the MEMS mirror can reach up to several kHz nowadays, video-rate scanning speed of our system could be realized. The two-dimensional (2D) scanning MEMS mirror (PE100011, OPUS) with oscillation frequency 16~20 kHz for the fast axis and 1~2 kHz for the slow axis can project a Lissajous scanning curve to cover the FOV. Considering the scanning efficiency and the missing pixel problem, we set the oscillation frequency of the MEMS scanning mirror to 16 kHz in the fast axis and 1.75 kHz in the slow axis. Then it leads to a frame rate of 17/s with no missing pixel. By average and interpolation method, we can double the frame rate to 34/s, thus the video rate is realized.
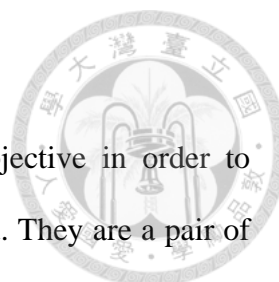
4.1.1 Tube lens pair design

We use a home-made imaging head instead of a commercial objective in order to miniaturize the size. Only the most critical components are included. They are a pair of tube lens, a mini aspheric lens, a MEMS scanning mirror, and a dichroic beam splitter. The beam size of the incidence reflected by the MEMS mirror will be magnified by the tube lens pair. With different ratio of magnification, the tube lens pair controls how much the clear aperture (CA) of the aspheric lens will be covered. Thus, the FOV and the resolution of the objective lens will be decided.

We have three tube lens pairs with different beam size magnification: the 1:1 magnification, the 1:1.5 magnification, and the 1:3 magnification. The design of the 1:1 tube lens pair is carried out by the optical design program ZEMAX for less spherical aberration. The controllable parameter includes the material of the glass, the radius of curvature, the thickness and the diameter of the lens. Through the simulation, the optical path difference (OPD) and aberrations of different incident angle are reduced (the further discussion is in section 4.4.3). Finally, the 1:1 tube lens pair was manufactured by ITRC (Instrument Technology Research Center).

Lens Data Editor

Edit Solves Options Help

Surf:Type		Comment	Radius	Thickness	Glass	Semi-Diameter	
OBJ	Standard		Infinity	Infinity		Infinity	
STO	Standard		Infinity	5.000000		0.350000	
2*	Standard		9.860948	5.000000	SF11	5.000000	U
3*	Standard		-8.170207	10.000000		5.000000	U
4*	Standard		10.903525	7.000000	SF11	5.000000	U
5*	Standard		-8.832714	5.000000		5.000000	U
6	Paraxial			0.700000		0.429865	
IMA	Standard		Infinity	-		0.109418	

Fig 4.1 Controllable parameters of a 1:1 magnification tube lens pair, which includes the radius of curvature, type of the glass, the thickness and the semi-diameter of the lens.
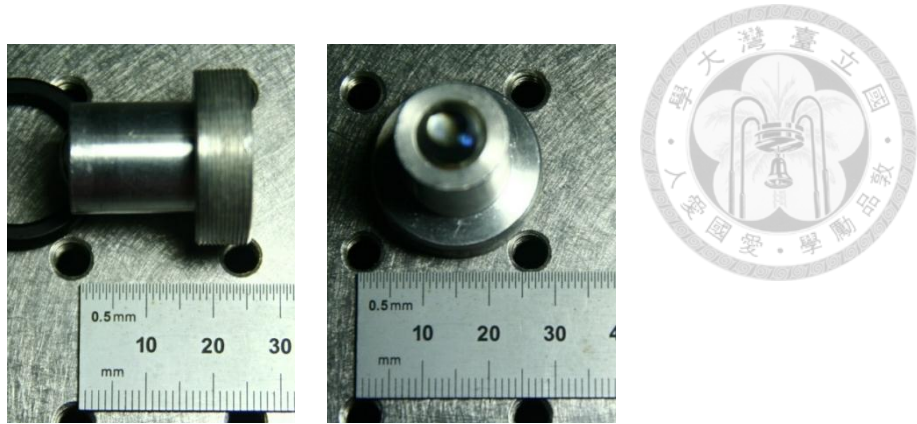
Fig 4.2 Side and bottom view of the originally packaged 1:1 magnification tube lens. The lenses are 1cm long in diameter, and the total length of the tube is 2.5 cm.
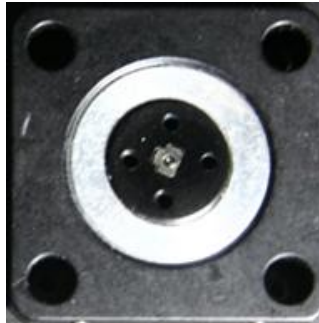
Fig 4.3 Top view of the mini aspheric lens (laser diode collimating lens) mounted on the originally packaged 1:1 magnification tube lens pair.

The diameter of the MEMS mirror is 1.2 mm, and the CA (clear aperture) of the mini aspheric lens (collimating lens) is also 1.2 mm. However, since the MEMS mirror is 45^0 angle oblique to the mini aspheric lens, the effective cross-sectional area for the incidence is smaller than the full aperture of the aspheric lens (ratio: $(\cos 45^o)^2 = (\frac{1}{\sqrt{2}})^2 = \frac{1}{2} < 1$). So if we choose a 1:1 magnification tube lens pair, the aspheric lens won't perform its full numerical aperture (0.8 NA for the laser diode collimating lens). Therefore, the resolution is not as ideal as we expect. To cover the full aperture of the mini aspheric lens, we need tube lens pairs for higher beam size magnification.

The 1:1.5 magnification tube lens pair is composed of two commercial lenses

(KPX013AR.16 and KPX016AR.16, Newport). Each of the lenses is 6.35 mm long in diameter. By using this lens pair, the beam size of the incidence can cover the full aperture of the mini aspheric lens (collimating lens) (ratio: $(\frac{1}{\sqrt{2}} \times \frac{3}{2})^2 = \frac{9}{8} > 1$) after passing through the MEMS scanning mirror and the tube lens pair. Thus, the aspheric lens can perform its full NA.

The CA of another kind of mini aspheric lens (Blu-ray disk lens) is close to 2 mm. Here, we use a tube lens pair with 1:3 magnification to cover the full aperture of the mini aspheric lens (ratio: $(\frac{1.2}{2} \times \frac{1}{\sqrt{2}} \times 3)^2 = \frac{81}{50} > 1$). The tube is also composed of two commercial lenses with a 6.35 mm diameter (KPX010AR.16 and KPX016AR.16, Newport).

Though we can use higher magnification tube lens pair to cover the entire CA, however, the FOV will reduce. It's a trade-off between the resolution and the FOV. On the other hand, the coma (comatic aberration) also increases due to the oblique incidence.

4.1.2 Aspheric lens

Most of the common simple lenses are spherical lenses of which the surface profiles are just part of a right sphere, whereas aspheric lenses are not. A typical aspheric lens usually has a more complicated surface profile designed for aberration reduction or replacement for a multi-lens system.

Unlike the part of a right sphere, the complex surface profile of an aspheric lens is described as the form [4.1]

$$z(r) = \frac{r^2}{R\left(1 + \sqrt{1 - (1 + \kappa)\frac{r^2}{R^2}}\right)} + \alpha_1 r^2 + \alpha_2 r^4 + \alpha_3 r^6 + \cdots$$

where the optic axis is in the z direction, and $z(r)$ means the displacement of the surface from the vertex in z direction at distance r from the optic axis. The coefficients α_i describe the deviation of the surface from the axially symmetric quadric surface specified by R and κ.

Mini aspheric lenses have many kinds of applications. They are commonly used in 3C products, such as: consumer cameras, camera cell phones, optical disk drives, and video players. They are also used for laser diode collimation and for light coupling of optical fibers.

Fig 4.4 Dual lens pair in an optical disk drive, where the marked on is the BD lens and another one is the DVD lens. A simple way to distinguish these two lenses is to observe their reflective light. The surface coating for the BD lens is highly transmitted for blue light, so it will reflect yellow light; whereas the DVD lens is highly transmitted for red light, thus it will reflect blue light.

There are two conditions we concerned while picking the aspheric lens as the objective of the imaging head. First, the size should be small within several millimeters, so it could be integrated into a miniaturized system. Next, the NA of the lens should be high, since we consider the resolution is simply proportional to $\frac{0.61\lambda}{NA}$. Finally, two kinds of

mini aspheric lens are chosen. One (FLBN1Z001A, ALPS) with 0.8 NA is originally designed for laser diode collimating. Another one with 0.85 NA is the BD (blu-ray disk) lens from the optical disk drive (Panasonic) of the laptop.

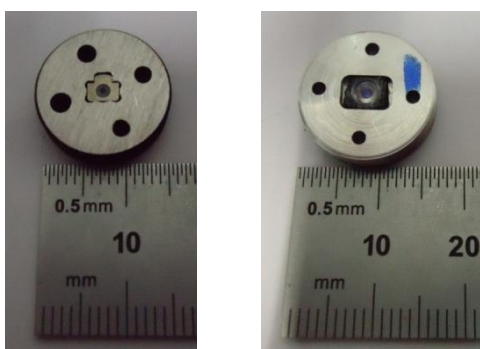**Fig 4.5** The mounted diode collimating lens (left) and the mounted BD lens (right).

4.2 Package of the system and experimental setup

Fig 4.8 is the setup of the experiment. Different pulsed lasers can be used as the excitation source. A pair of telescope (L1+L2) (KPX112 and KPX094, Newport) is used to adjust the incident beam size in order to match the MEMS scanning mirror.
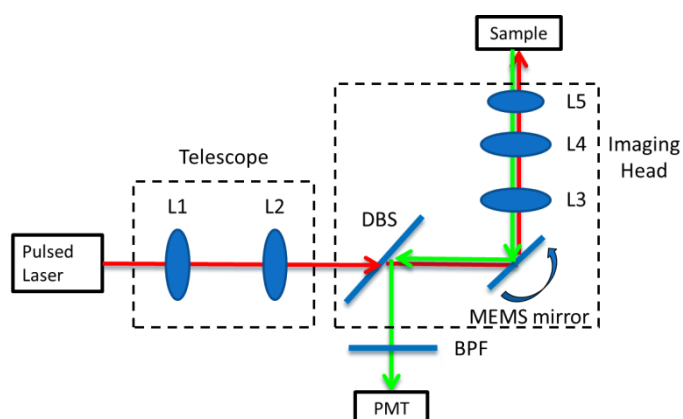

Fig 4.6 Setup of the experiment.

Fig 4.7 is the side view of the system and how the optical path runs. The red line indicates the excitation light. After beam size magnification by the telescope (L1+L2), the excitation light enters the system and passes through a DBS (dichroic beam splitter) (FF705-Di01, Semrock). Due to its special coating, it only allows infrared light to pass, but reflects the visible light. After passing through the beam splitter, the excitation light hits the MEMS scanning mirror. Then the light passes through L3, L4, and L5, where L3 and L4 are the tube lens pair and L5 is the mini aspheric lens .Finally it reaches the sample and the nonlinear optical signal is generated near the focus, such as 2PF or HG.

The green line indicates the epi-collected signal. It traces back through almost the same path but is reflected by the DBS and enters the PMT (photomultiplier tube) (R4220P, Hamamatsu). The band pass filter (BPF) (FF01-520/35-25, Semrock) is set to collect the signal of 2PF or HG.
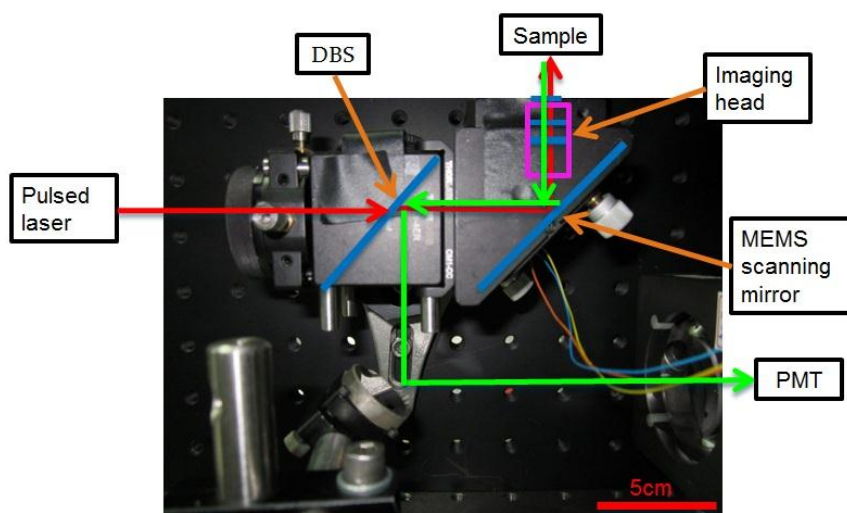

Fig 4.7 Side view of the originally packaged system.

4.2.1 Repackage of the system

The originally packaged work was done by the former lab member Che-Hang Yu. The

package is composed of the commercial mount (CM1-4ER, Thorlabs) for the dichroic beam splitter, and the commercial mount (KC82, Thorlabs) for the MEMS scanning mirror, and a home-made objective including the tube lens pair and the mount of the mini aspheric lens. By reserving only the most essential parts of the components (DBS, MEMS mirror, and the imaging head) and remounting them in a series of customized package, the repackaged size of the imaging head is much smaller than the originally packed one. Besides, replaceable tube lens pairs for different beam size magnification are also designed for different mini aspheric lens.
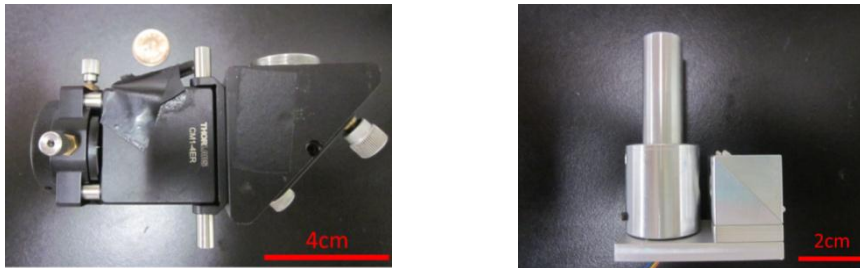
Fig 4.8 The originally packaged system (left) and the newer one (right).

Fig 4.9 Size comparison of the two systems.

Fig 4.10 Replaceable tube lens pairs, the magnification ratio is 1:1.5, 1:3, and 1:1 (top to bottom).
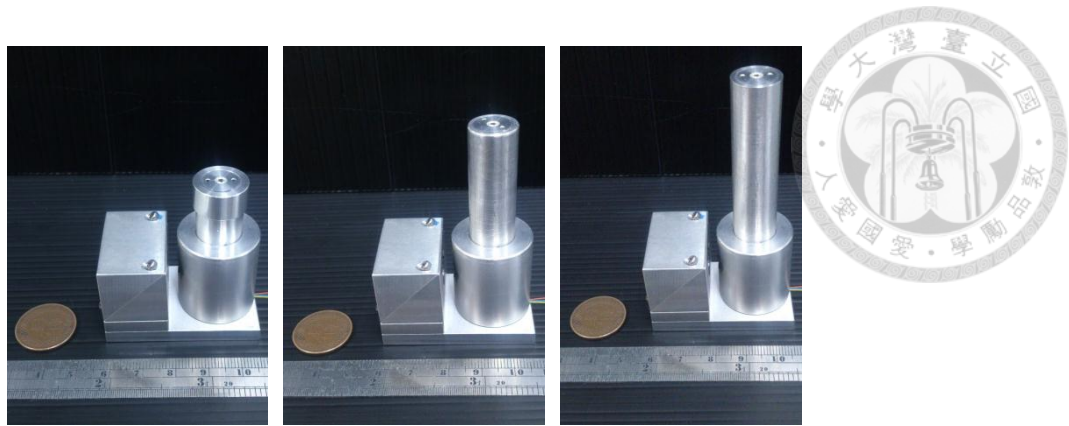
Fig 4.11 Replaceable tube lens pairs mounted with the repackaged system with magnification ratio 1:1,

1:3, and 1:1.5 (left to right).
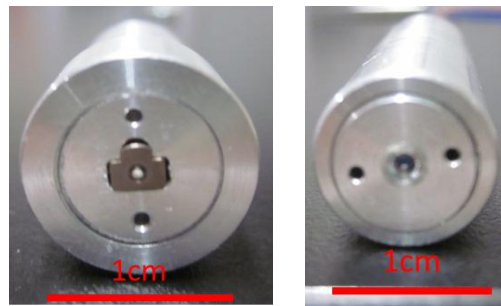
Fig 4.12 The collimating lens (left) and BD lens (right) mounted in the tube respectively.
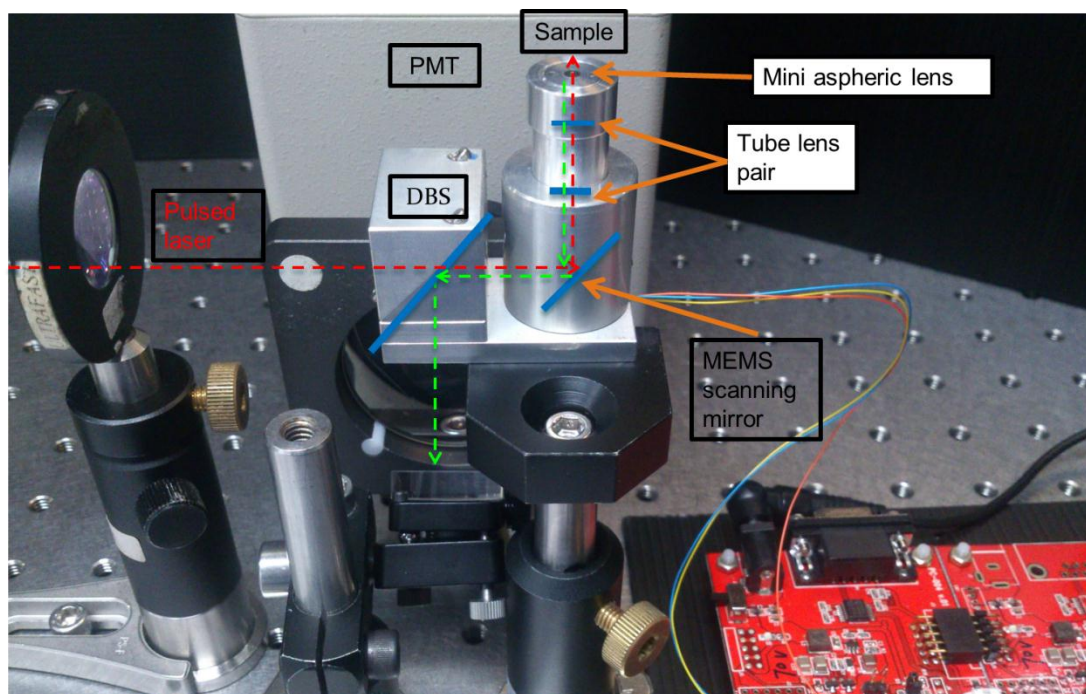
Fig 4.13 Side view of the repackaged system. The red board on the right side provides a 0~70 voltage to

drive the MEMS mirror.
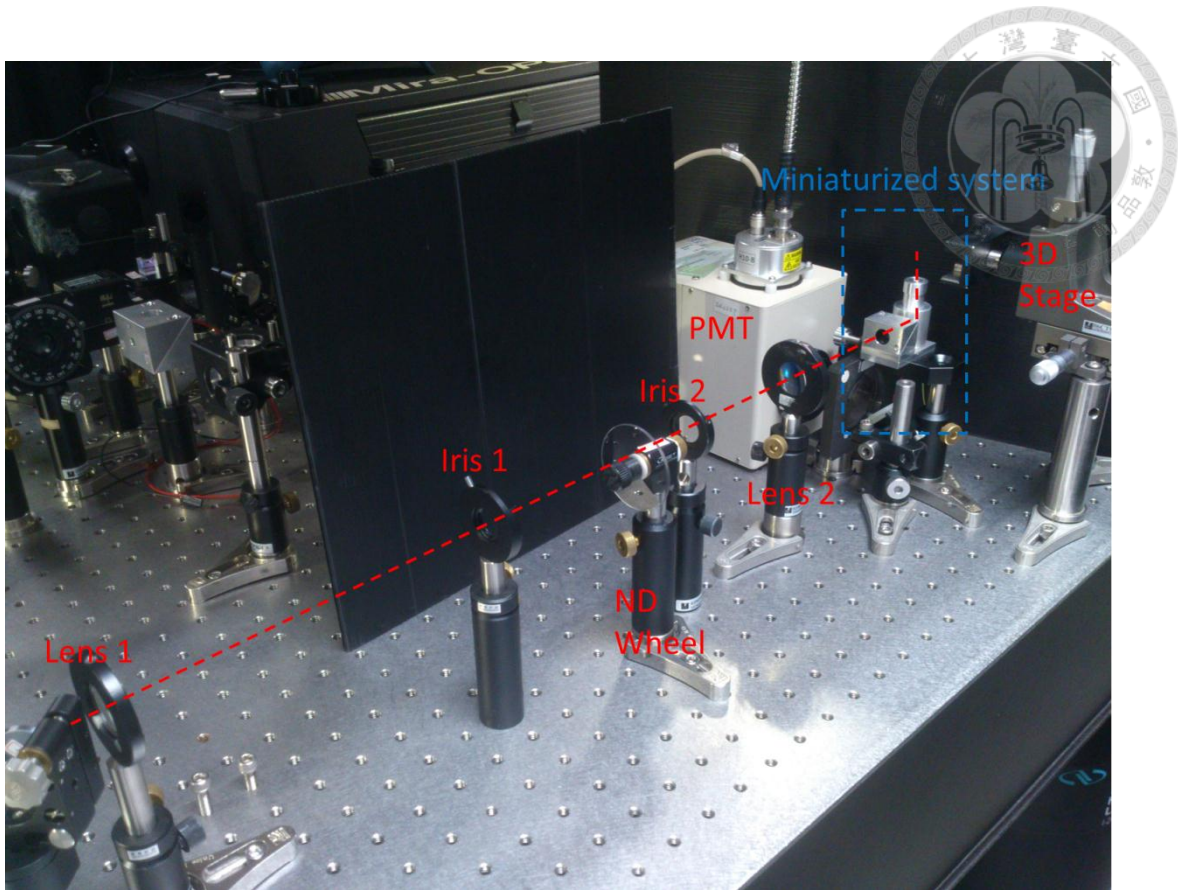
Fig 4.14 Experimental setup including the telescope, PMT, and the 3D stage. The telescope consists of

Lens 1 (KPX112, Newport) and Lens 2 (KPX094, Newport).
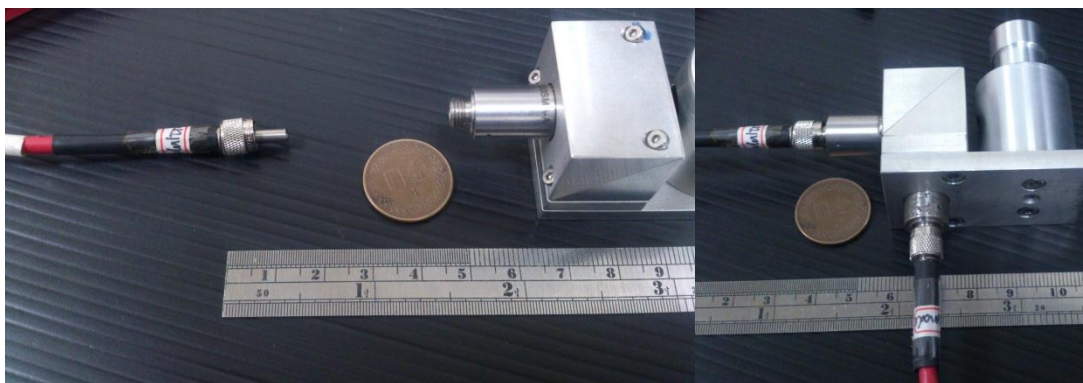
Fig 4.15 Collimators can be directly mounted to the system for fiber-based light source or signal

collection delivery.
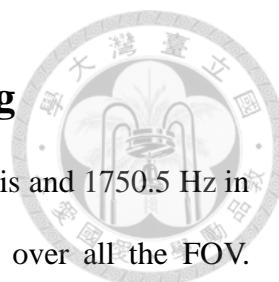
4.3 Electronic control and instant data processing

Since the scanning speed of the MEMS mirror is 16016 Hz in fast axis and 1750.5 Hz in slow axis, the sampling rate must be even higher while scanning over all the FOV. Sampling frequency up to 36.7 MHz (36666667 Hz) is needed to ensure every pixel of a 512×512 pixels frame will be captured with a 17/s frame rate. To double the frame rate up to 34/s, we apply the average and interpolation method.

With such a high sampling frequency, a tremendous amount of data will be generated, so mass data acquisition and instant mapping become crucial tasks. An FPGA (field programmable gate array) computer system (PXIe, National Instruments) is introduced to deal with this situation. It is capable of instant data acquisition and mapping in 2-channel 14-bit 512×512 pixels frame. Thus a real-time continuous video image can be shown on the monitor while the experiment is conducted. Thanks to the high-speed PXIe buses, the data can be also recorded and stored in a 1TB RAID (redundant array of independent disks) simultaneously for up to two hours. This work is thanks to the help of Yu-Hsiang Cheng.

Fig 4.16 Electronic control of the system.

4.4 Performance

In this section, we use the "1951 USAF resolution chart" (RES-1, Newport) to analyze two major parameters of the microscope, including the FOV (field of view) and the resolution. The 1951 USAF resolutio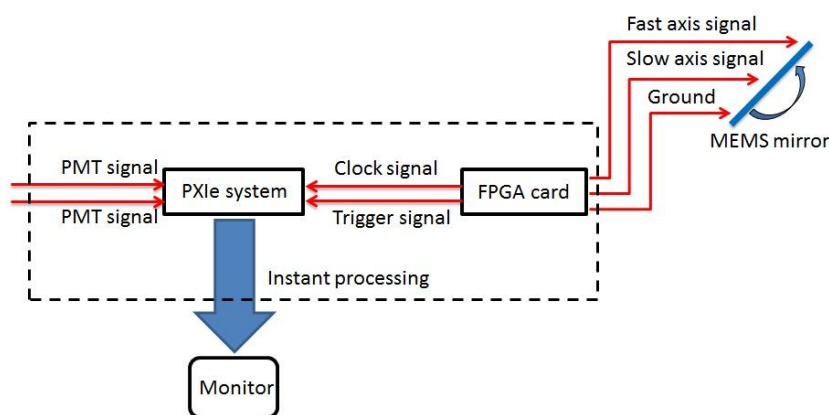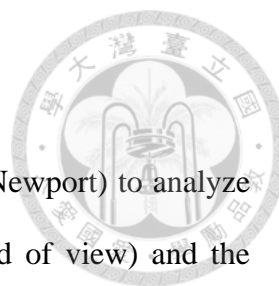n chart is a test pattern conforming to the standard set by US Air Force in 1951. It consists of groups of three bars (small Ronchi rulings) with dimensions from big to small, and the largest bar can't be discerned is the limitation of the resolving power. Since the normal resolution chart can't emit 2PF, we use the green fluorophore to dye the chart. Thus, we can observe the pattern of the chart by 2PF microscopy with a 920 nm excitation light and a 520 nm emitted signal.

Fig 4.17 The 1951 USAF resolution test chart.

	Line Pairs per millimeter							
Element Number	Group Number							
	0	1	2	3	4	5	6	7
1	1.00	2.00	4.00	8.00	16.00	32.00	64.00	128.00
2	1.12	2.24	4.49	8.98	17.96	35.92	71.84	143.70
3	1.26	2.52	5.04	10.08	20.16	40.32	80.63	161.30
4	1.41	2.83	5.66	11.31	22.63	45.25	90.51	181.00
5	1.59	3.17	6.35	12.70	25.40	50.80	101.60	203.20
6	1.78	3.56	7.13	14.25	28.51	57.02	114.00	228.10
Line pairs/mm = LP			Line width (mm) = 1/(2LP)					
Space width (mm) = 1/(2LP)			Line length = 5(line width)					

Table 4.1 Specifications of the chart, including how to measure the line pairs/mm, the space width, the line width, and the line length of different group and element numbers.
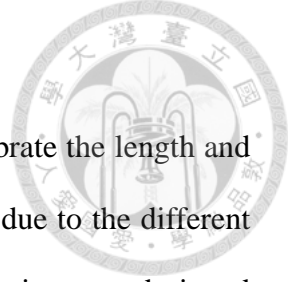
4.4.1 Field of view (FOV) estimation

In order to measure the actual area of the FOV, first we have to calibrate the length and the width of the image since the scanning shape is a rectangle. It is due to the different scanning angle and frequency of each scanning axis of the MEMS mirror we designed for a higher frame rate and no missing pixels. The scanning angle is inversely proportional to the scanning frequency, so the MEMS mirror scans in a rectangular shape.

Fig 4.18 (a) is the FOV mapped into a 512×512 pixels frame, in which the ratio of the length to the width of the rulings is not correct. The actual ratio should be 5:1 according to the standard, so we calibrate the figure by compressing its width to get Fig 4.18 (b). Then we look up the information of the rulings (Group 6 Element 3) in Table 4.1. Thus we can get the line length:

$$\frac{1000 \ \mu m}{2 \times 80.63} \times 5 \approx 31 \ \mu m$$

The line width and the space width are:

$$\frac{1000 \ \mu m}{2 \times 80.63} \approx 6.2 \ \mu m$$
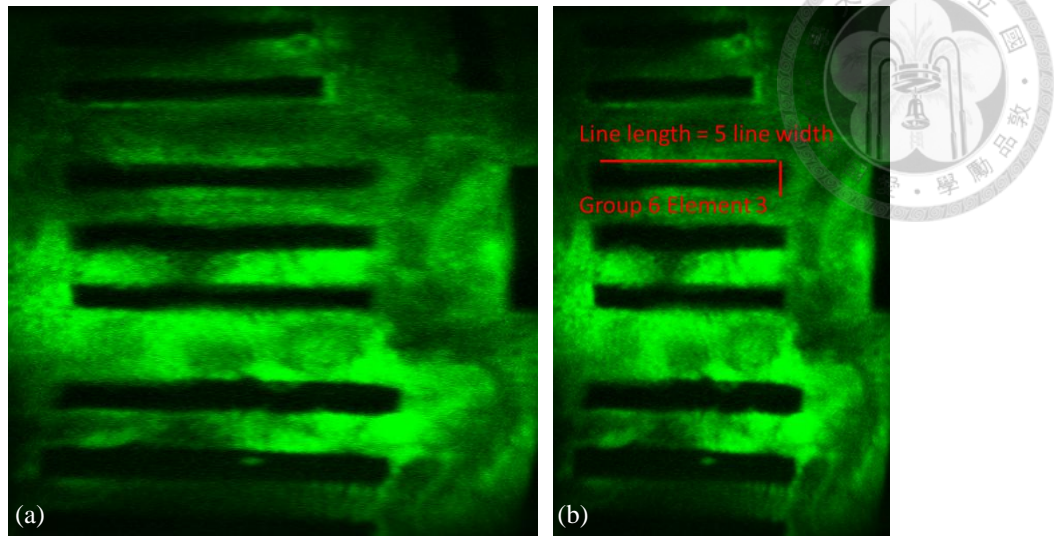
Fig 4.18 The 2PF pattern of the green-fluorophore-dyed 1951 USAF resolution test chart (rulings of

Group 6, Element 3) (BD lens with 1:3 tube lens). **(a)** The FOV mapped into a 512×512 pixels frame. **(b)**

The actual FOV after calibration is 59 μm × 93 μm.

Considering the rulings as a standard scale, we can measure the actual FOV by:

$$l_{af}: l_{ar} = l_{if}: l_{ir}$$

$$l_{af} = \frac{l_{ar} \times l_{if}}{l_{ir}}$$

where l_{af} is the actual length of the FOV, l_{ar} is the actual length of the ruling, l_{if} is

the length of the FOV in the image, and l_{ir} is the length of the ruling in the image. The

rulings (l_{ar}) are 31 μm long and 6.2 μm wide (Group 6 Element 3).
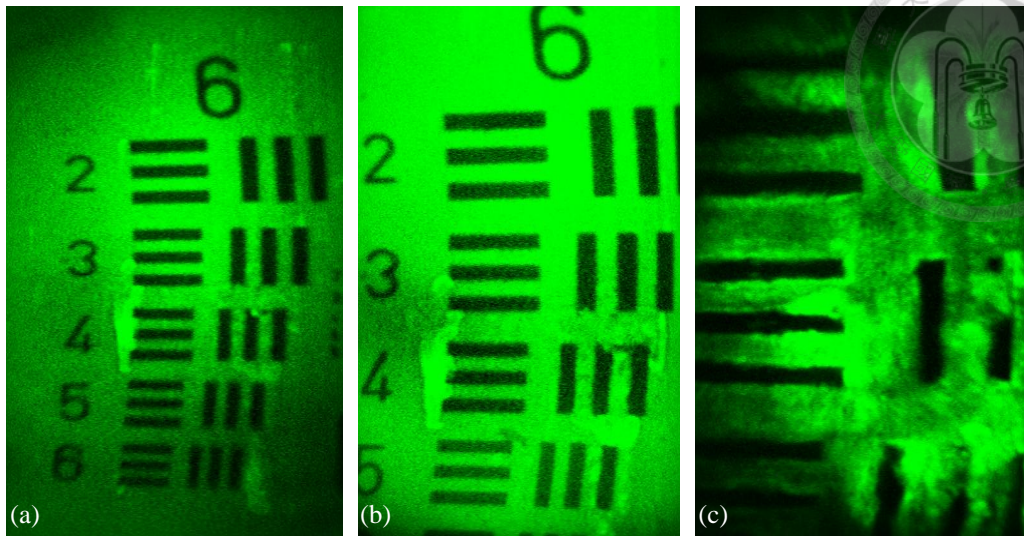
Fig 4.19 The FOV of the BD lens as the objective with different tube lens pairs. **(a)** FOV: 178 μm × 280 μm with 1:1 tube lens. **(b)** FOV: 121 μm × 200 μm with 1:1.5 tube lens. **(c)** FOV: 59 μm × 93 μm with 1:3 tube lens.

In Fig 4.19 and Fig 4.20, as the FOV increases we can find that the shape of the rulings start to distort. This effect could be attributed to "distortion", which is one kind of optical aberration. We'll discuss more about this in section 4.4.5.

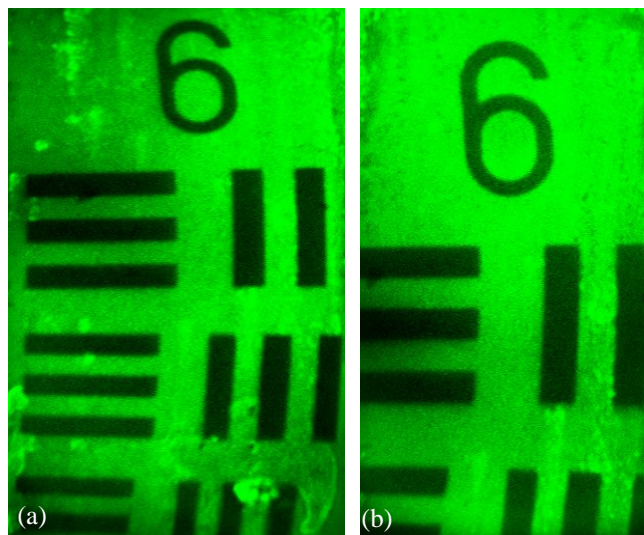**Fig 4.20** The FOV of the collimating lens as the objective with different tube lens pairs. **(a)** FOV: 87 μm × 140 μm with 1:1 tube lens. **(b)** FOV: 62 μm × 112 μm with 1:1.5 tube lens.

66

Tube lens magnification	Lens type	x-direction	y-direction
1:1	BD	178	280
	collimating	87	140
1:1.5	BD	121	200
	collimating	62	112
1:3	BD	59	93

Table 4.2 Field of view (FOV) comparison among combinations of different aspheric lens and tube lens.

(unit: μm)

4.4.2 Resolution estimation

The typical way to estimate the spatial resolution is to analyze the point spread function (PSF) of a sub-resolution (point-like) radiating sources, such as quantum dots or fluorescent beads. However, this method is not so convenient since sometimes these sources are not available or it's hard to find a sub-resolution point source in the image. Therefore, we use another method, the "step-edge" method [4.2], to estimate the lateral resolution. The method is relatively convenient because the measurement can be derived from the edge source instead of the sub-resolution point source in the image. Considering a "step-edge" source as the input of the optical system, then the actual acquired signal through the edge is the edge response. We can get the line spread function (LSF) in the considered direction by differentiating the edge response with respect to the position. Finally, the full width at half maximum (FWHM) of the LSF is regarded as the estimation of the lateral resolution [4.3].

In the following Fig 4.21 to Fig 4.23 we briefly describe how we apply the method step by step.
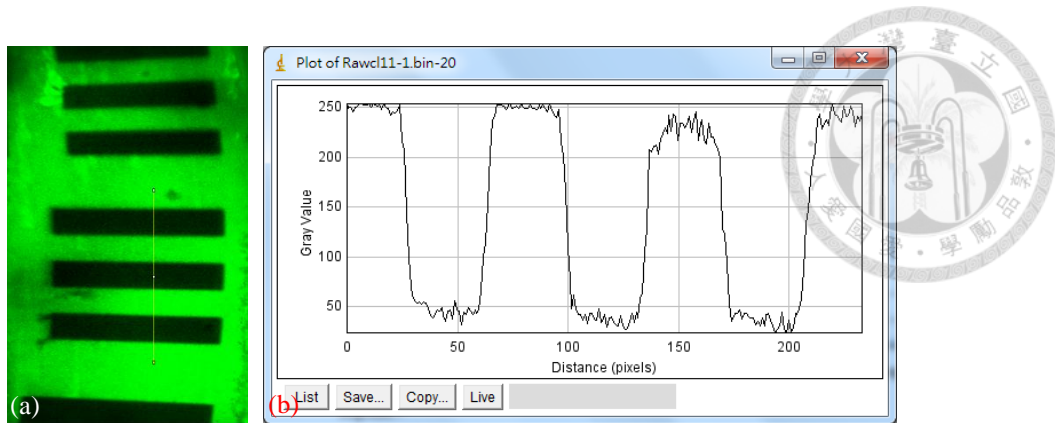
Fig 4.21 (a) The red line indicates the direction we choose across six edges. **(b)** The corresponding edge response.
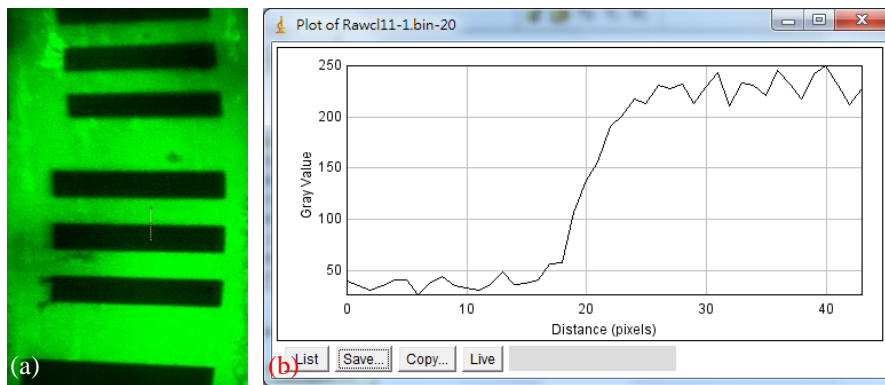
Fig 4.22 (a) Still in the same direction, but we shorten the red line and choose only one edge this time. **(b)** The corresponding edge response.
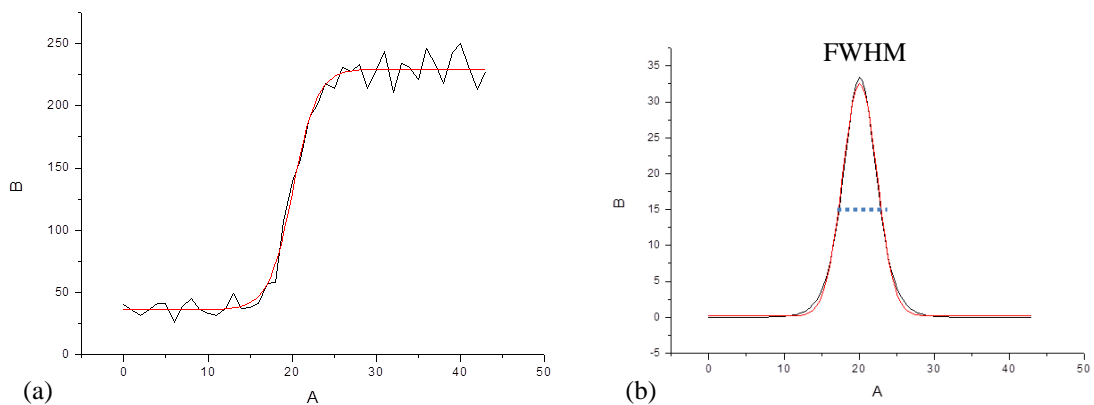
Fig 4.23 (a) The edge response (black curve) and the Boltzmann fitting (red curve). **(b)** The PSF differentiated from the Boltzmann fitting curve with respect to the position (red curve) and the Gaussian fitting curve (blue curve). The FWHM of this Gaussian curve is considered as the estimation of the lateral resolution in this direction.

The result for the all 5 combinations of different tube lens pair and the mini aspheric lens is listed in Table 4.3 and Table 4.4. The 1:1 magnification tube lens pair provides larger FOV, whereas the 1:1.5 and the 1:3 magnification tube lenses are designed for the collimating lens (0.8 NA) and the BD lens (0.85 NA) to cover the CA and perform their full NA respectively. Thus, they provide smaller FOV but better resolution power.

To evaluate the resolution from different part of the figure, we divide the figure into 4 pieces and assume the resolution in each quadrant is similar due to the symmetry. Then we randomly choose one quadrant and divide it into a 3x3 area to analyze the resolution. Different values of the resolution from those areas are expected since we consider the oblique incidence will lead to aberrations. We'll discuss it in section 4.4.3.
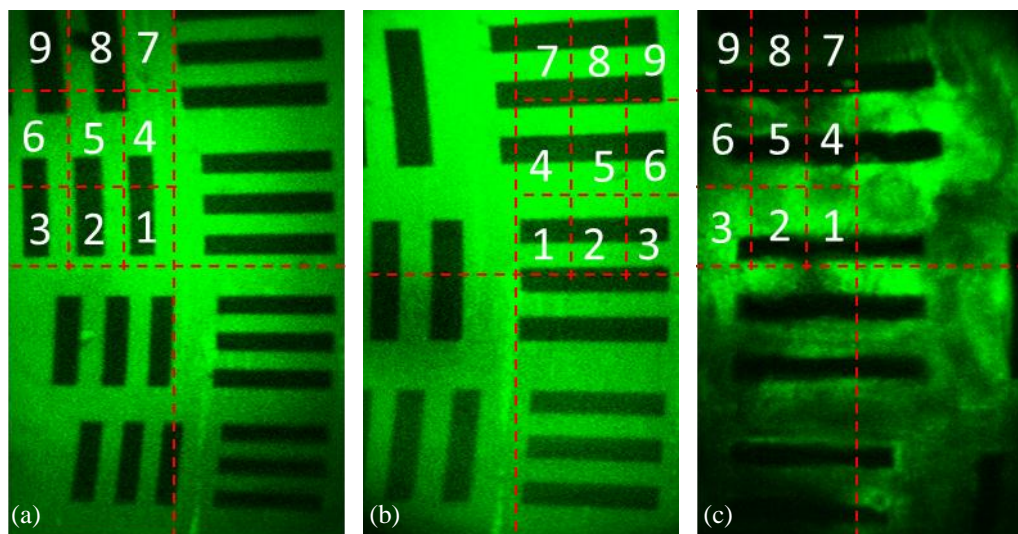

Fig 4.24 Sample pictures for resolution analysis of the BD lens with **(a)** the 1:1, **(b)** the 1:1.5, and **(c)** the 1:3 tube lens pair. First, each figure is divided into 4 pieces. Then one of the quadrants is further divided into a 3x3 area and labeled from 1 to 9. Due to the oblique incidence, we expect a difference of the resolution between the central part of the frame (ex: area 1, area 2, or area 4) and the marginal part of the frame (ex: area 3, area 7, or area 9).

Tube lens	Area	1	2	3	4	5	6	7	8	9
1:1	x-direction	1.63	1.73	1.85	1.76	1.89	1.99	1.93	2.03	2.09
	y-direction	1.66	1.76	1.82	1.78	1.86	1.98	1.95	2.00	2.08
1:1.5	x-direction	1.06	1.12	1.16	1.13	1.21	1.21	1.19	1.22	1.26
	y-direction	1.04	1.13	1.18	1.18	1.22	1.24	1.20	1.27	1.29
1:3	x-direction	0.60	0.63	0.66	0.64	0.67	0.75	0.69	0.77	0.80
	y-direction	0.62	0.64	0.70	0.67	0.71	0.77	0.72	0.78	0.79

Table 4.3 Resolution from different area of the image of the BD lens with different tube lens pairs. (unit: μm)
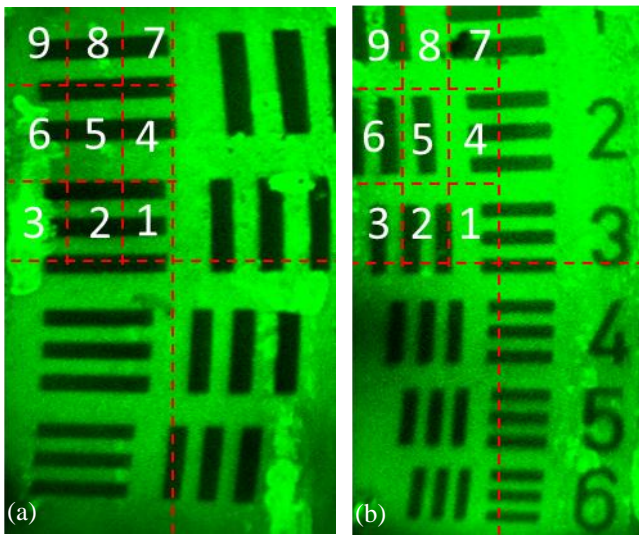
Fig 4.25 Sample pictures for resolution analysis of the collimating lens with **(a)** the 1:1 and **(b)** the 1:1.5 tube lens pair.

Tube lens	Area	1	2	3	4	5	6	7	8	9
1:1	x-direction	1.30	1.32	1.34	1.34	1.39	1.50	1.45	1.52	1.54
	y-direction	1.30	1.35	1.39	1.37	1.40	1.45	1.41	1.48	1.50
1:1.5	x-direction	0.67	0.70	0.76	0.72	0.80	0.81	0.81	0.86	0.91
	y-direction	0.67	0.69	0.78	0.70	0.82	0.85	0.83	0.88	0.90

Table 4.4 Resolution from different area of the image of the collimating lens with different tube lens pairs. (unit: μm)
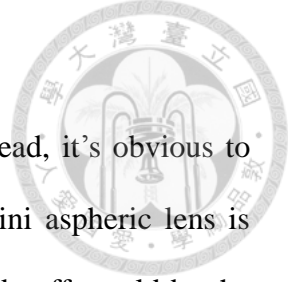
4.4.3 Performance discussion

From table 4.2 to Table 4.4, for all combinations of the imaging head, it's obvious to find that the resolution power becomes better as the CA of the mini aspheric lens is gradually covered with higher magnification tube lens pair. The trade-off would be the decrease of the FOV.

The resolution limit is $\frac{0.61\lambda}{NA}$ according to Rayleigh's criterion and $\frac{0.51\lambda}{NA}$ according to Sparrow's criterion as we mentioned in section 2.1.1. For the nonlinear optical microscopy, the resolution limit is improved. For an Nth order nonlinear optical process, the FWHM is decreased by a factor of $\sqrt{N}$ [4.4] relative to the linear optical process. Thus, the lateral resolution for SHG and THG can be shown as follows based on Rayleigh's criterion:

$$r_{SHG} = \frac{1}{\sqrt{2}} \frac{0.61\lambda}{NA} \approx \frac{0.43\lambda}{NA}$$

$$r_{THG} = \frac{1}{\sqrt{3}} \frac{0.61\lambda}{NA} \approx \frac{0.35\lambda}{NA}$$

For N-photon fluorescence, the FWHM is also modified by a factor $\sqrt{N}$ [4.4], so the lateral resolution based on Rayleigh's criterion for 2PF is:

$$r_{2PF} = \frac{1}{\sqrt{2}} \frac{0.61\lambda}{NA} \approx \frac{0.43\lambda}{NA}$$

For a 920 nm wavelength excitation light, if we regard our objective as perfect, the resolution limit of 2PF microscopy for a CA fully covered collimating lens (0.8 NA) should be:

$$r_{2PF} = \frac{1}{\sqrt{2}} \frac{0.61\lambda}{NA} \approx \frac{0.43\lambda}{NA} = \frac{0.43 \times 0.92\mu m}{0.8} \approx 0.49\mu m$$
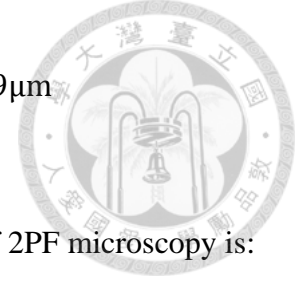
As for a CA fully covered BD (0.85 NA) lens, the resolution limit of 2PF microscopy is:

$$r_{2PF} = \frac{1}{\sqrt{2}} \frac{0.61\lambda}{NA} \approx \frac{0.43\lambda}{NA} = \frac{0.43 \times 0.92\mu m}{0.85} \approx 0.47\mu m$$

However, even though the CA is fully covered, the experimental result is still worse than the resolution limit. It is because our objectives are not perfect indeed and the FWHM of the PSF usually broadens due to various reasons, such as aberrations, imperfect lenses and mirrors, or even the atmospheric turbulence.

The aberrations our system suffered can mainly attribute to spherical aberration and comatic aberration. The spherical aberration is due to lights passing through different parts of the lens won't focus perfectly. There are two spherical lenses used in our system as the tube lens pair. Even though the incident beam size is small and it only passes through the center part of the lens, the spherical aberration still exists. Besides, in order to cover a large FOV the MEMS mirror scans $\pm 10^0$ in fast axis and $\pm 9.5^0$ in slow axis. Thus, the oblique incidence will leads to comatic aberrations.

Furthermore, the mini aspheric lenses are not originally designed for the excitation wavelength or the purpose we use. For example, BD lens is designed for 410 nm blue ray optical drive, whereas the collimating lens is for 1310 or 1550 nm laser diode. We consider them as imperfect lenses which will also lead to chromatic aberrations. By the way, the quality of the resolution test chart and the unevenness of the fluorescent dye

will also affect the analyzed resolute.

On the other hand, BD lens is not good for the oblique incidence in comparison with the collimating lens. This could be found that the central part of the figure is usually brighter and clearer than the margin of the figure from the BD lens objective, whereas figures from the collimating lens objective don't have this effect obviously.
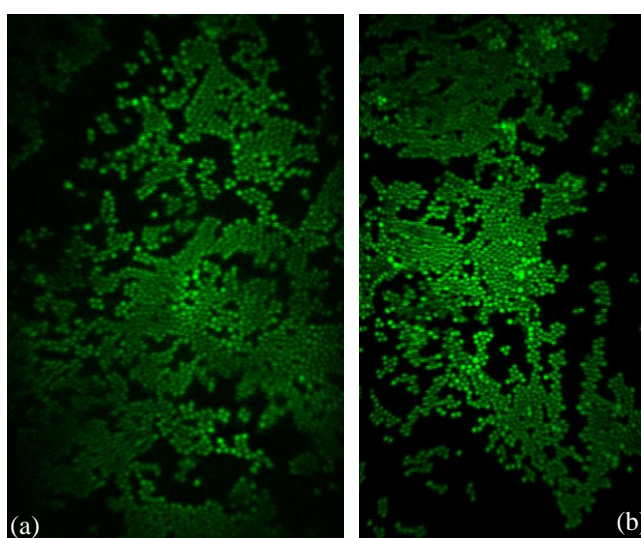
Fig 4.26 1.1μm diameter green fluorescent beads. The excitation wavelength is 920 nm, and the emission wavelength is around 520 nm for 2PF microscopy. The beads look dimmer in the corner of the FOV of the **(a)** BD lens with 1:3 tube lens, in comparison with the FOV of the **(b)** collimating lens with 1:1.5 tube lens.

Finally, sometimes there is a small difference between $r_{2PF,x}$ and $r_{2PF,y}$, maybe it is because the FOV is a rectangle rather than a square. After the FOV mapping into a 512×512 pixels frame, the y direction with a longer length has a lower resolution because a pixel has to resolve a longer distance.
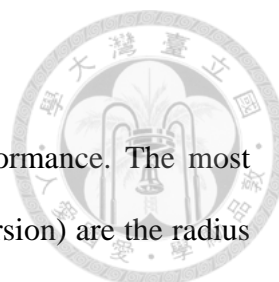
4.4.4 Simulation of the tube lens

Simulation of the optical system can help us to estimate the performance. The most important parameters for the simulation program ZEMAX (2005 version) are the radius of curvature of the lens, thickness of the lens, semi-diameter of the lens, and of course the distance between each lens. The specs for the tube lens (KPX010AR.16, KPX013AR.16, KPX016AR.16, Newport) are available. However, we lack of the detailed information (the aspheric coefficients) of the mini aspheric lens, so we attempt to find a substitute for the objective lens for similar performance (ex: NA or the radius) during the simulation. From Fig 4.27 to Fig 4.31 show the parameters we set to run the simulation for all the 5 combinations of the tube lens pair and the mini aspheric lens.

	Surf:Type	Comment	Radius	Thickness	Glass	Semi-Diameter	
OBJ	Standard		Infinity	Infinity		Infinity	
STO	Standard		Infinity	5.000000		0.420000	U
2*	Standard		9.860948	5.000000	SF11	5.000000	U
3*	Standard		-8.170207	10.000000		5.000000	U
4*	Standard		10.903525	7.000000	SF11	5.000000	U
5*	Standard		-8.832714	5.000000		5.000000	U
6*	Paraxial			0.700000 V		1.000000	U
IMA	Standard		Infinity	–		0.109944	

Fig 4.27 Simulation parameters of the 1:1 tube lens pair with the substitute of the BD lens.

	Surf:Type	Comment	Radius	Thickness	Glass	Semi-Diameter	
OBJ	Standard		Infinity	Infinity		Infinity	
STO	Standard		Infinity	12.700000		0.420000	U
2*	Standard		6.563000	3.819000	BK7	3.175000	U
3*	Standard		Infinity	28.650000		3.175000	U
4*	Standard		Infinity	3.527000	BK7	3.175000	U
5*	Standard		-9.819000	19.000000		3.175000	U
6*	Paraxial			0.994000 V		1.000000	U
IMA	Standard		Infinity	–		0.114152	

Fig 4.28 Simulation parameters of the 1:1.5 tube lens pair with the substitute of the BD lens.

	Surf:Type	Comment	Radius	Thickness	Glass	Semi-Diameter	
OBJ	Standard		Infinity	Infinity		Infinity	
STO	Standard		Infinity	6.400000		0.420000	U
2*	Standard		3.308000	5.381000	BK7	3.175000	U
3*	Standard		Infinity	19.520000		3.175000	U
4*	Standard		Infinity	3.527000	BK7	3.175000	U
5*	Standard		-9.819000	19.000000		3.175000	U
6*	Paraxial			0.999750 V		1.000000	U
IMA	Standard		Infinity	–		0.057365	

Fig 4.29 Simulation parameters of the 1:3 tube lens pair with the substitute of the BD lens.

Surf:Type		Comment	Radius	Thickness	Glass	Semi-Diameter	
OBJ	Standard		Infinity	Infinity		Infinity	
STO	Standard		Infinity	5.000000		0.420000	U
2*	Standard		9.860948	5.000000	SF11	5.000000	U
3*	Standard		-8.170207	10.000000		5.000000	U
4*	Standard		10.903525	7.000000	SF11	5.000000	U
5*	Standard		-8.832714	5.000000		5.000000	U
6*	Paraxial			0.699950		0.600000	U
IMA	Standard		Infinity	–		0.109908	

Fig 4.30 Simulation parameters of the 1:1 tube lens pair with the substitute of the collimating lens.

Surf:Type		Comment	Radius	Thickness	Glass	Semi-Diameter	
OBJ	Standard		Infinity	Infinity		Infinity	
STO	Standard		Infinity	12.700000		0.420000	U
2*	Standard		6.563000	3.819000	BK7	3.175000	U
3*	Standard		Infinity	28.650000		3.175000	U
4*	Standard		Infinity	3.527000	BK7	3.175000	U
5*	Standard		-9.819000	19.000000		3.175000	U
6*	Paraxial			0.994000 V		0.600000	U
IMA	Standard		Infinity	–		0.114152	

Fig 4.31 Simulation parameters of the 1:1.5 tube lens pair with the substitute of the collimating lens.

Then we can get the result of the simulated optical path difference (OPD) and the spot diagram of each combination.
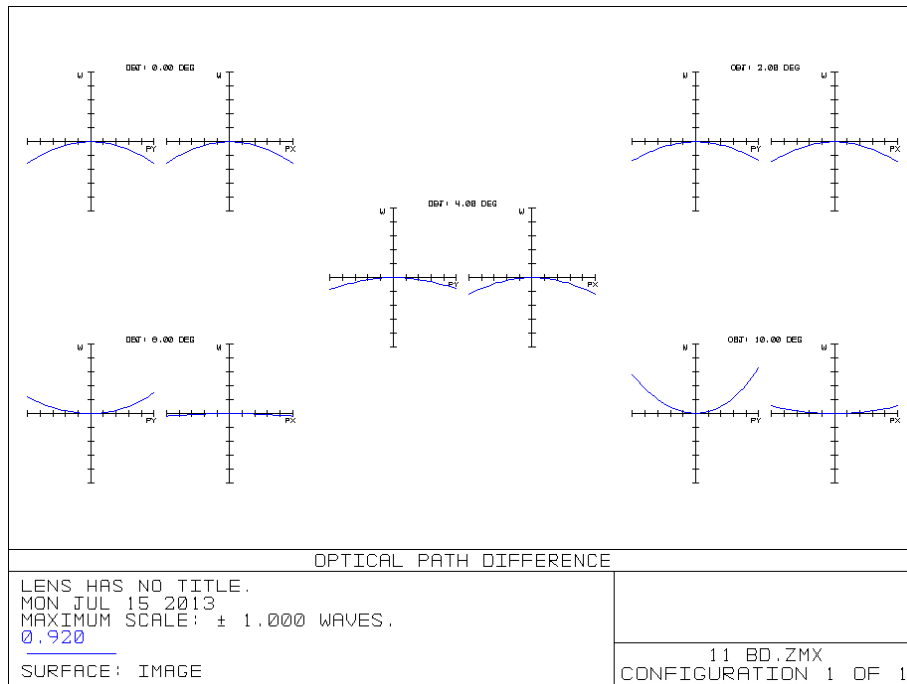

Fig 4.32 Simulated result of the OPD of the 1:1 tube lens pair with the substitute of the BD lens. The
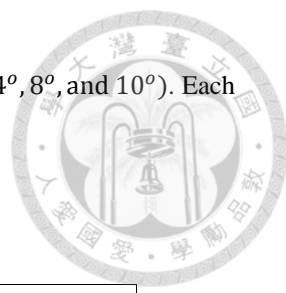
75

figure has 5 groups, which are incidences from 5 different incident angles ($0^o, 2^o, 4^o, 8^o,$ and 10°). Each

group has two graphs, which are the OPD in x and in y direction respectively.
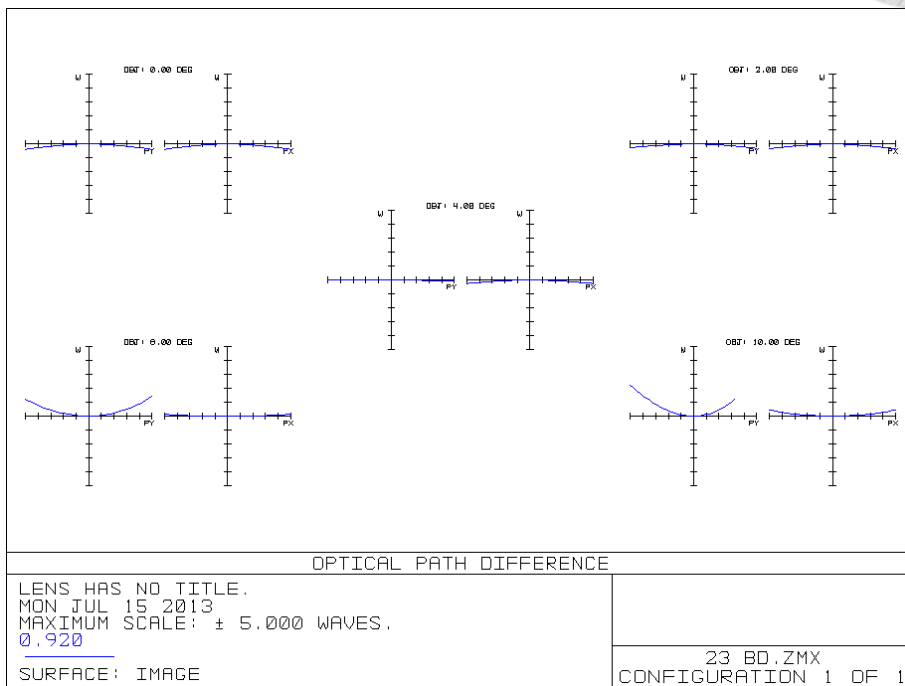

Fig 4.33 Simulated result of the OPD of the 1:1.5 tube lens pair with the substitute of the BD lens.
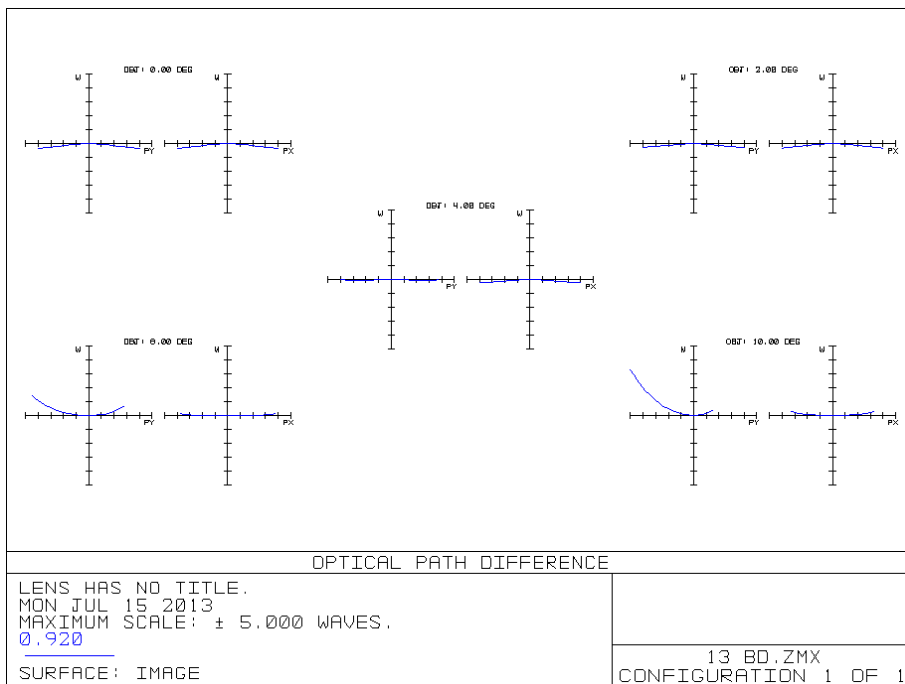

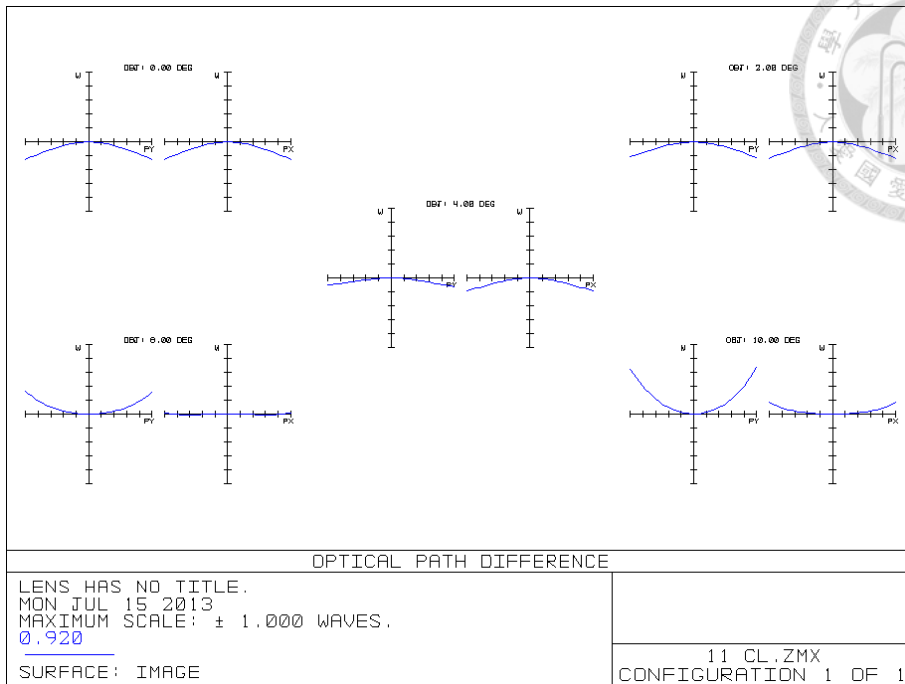**Fig 4.34** Simulated result of the OPD of the 1:3 tube lens pair with the substitute of the BD lens.

Fig 4.35 Simulated result of the OPD of the 1:1 tube lens pair with the substitute of the collimating lens.
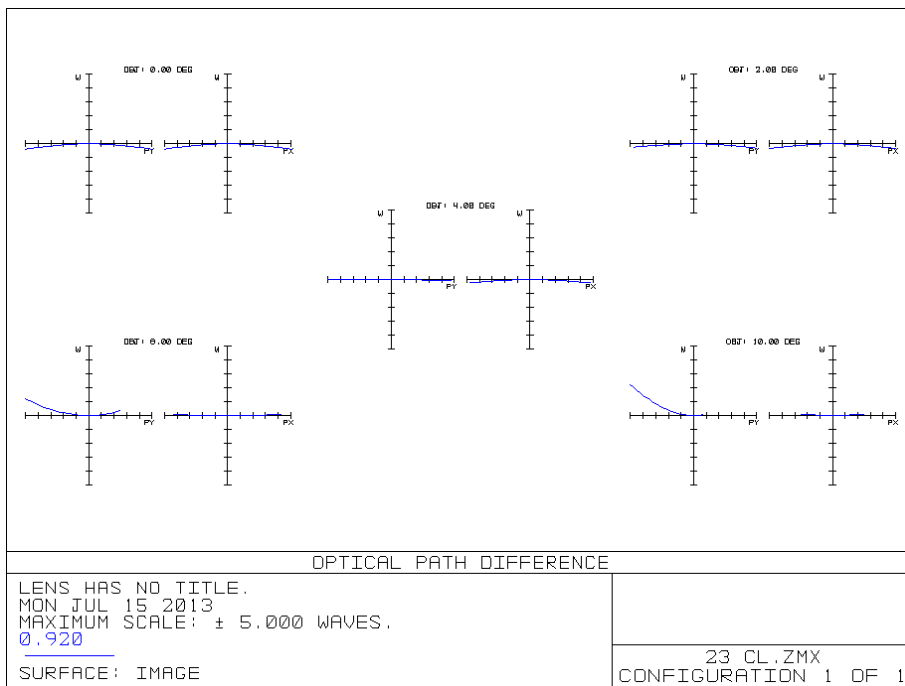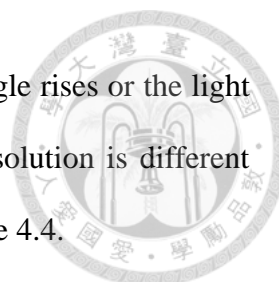

Fig 4.36 Simulated result of the OPD of the 1:1.5 tube lens pair with the substitute of the collimating lens.

From Fig 4.32 to Fig 4.36 we can see the curve rising or falling, which means the

77

positive or the negative OPD. The OPD increases as the incident angle rises or the light deviates from the central axis. This could also explain why the resolution is different between the central and the margin of the FOV in Table 4.3 and Table 4.4.

To further estimate the aberration, we can consider the simulated spot diagram as the comparison with the resolution limit. We regard it as the theoretical resolution limit for our imperfect optical system, which is more practical than using Rayleigh's criterion.
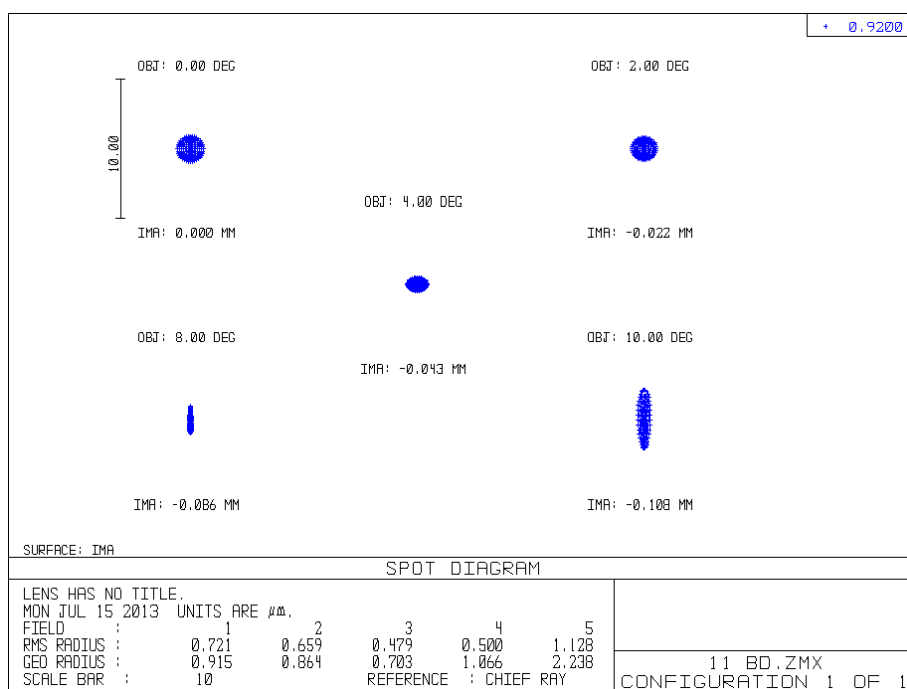

Fig 4.37 Spot diagram of the OPD of the 1:1 tube lens pair with the substitute of the BD lens. The figure has 5 groups, which are incidences from 5 different incident angles ($0^o, 2^o, 4^o, 8^o,$ and 10°). The GEO radius indicates the longest part of the spot. The RMS (root mean square) radius considering all direction of the spot is regarded as the theoretical resolution limit.
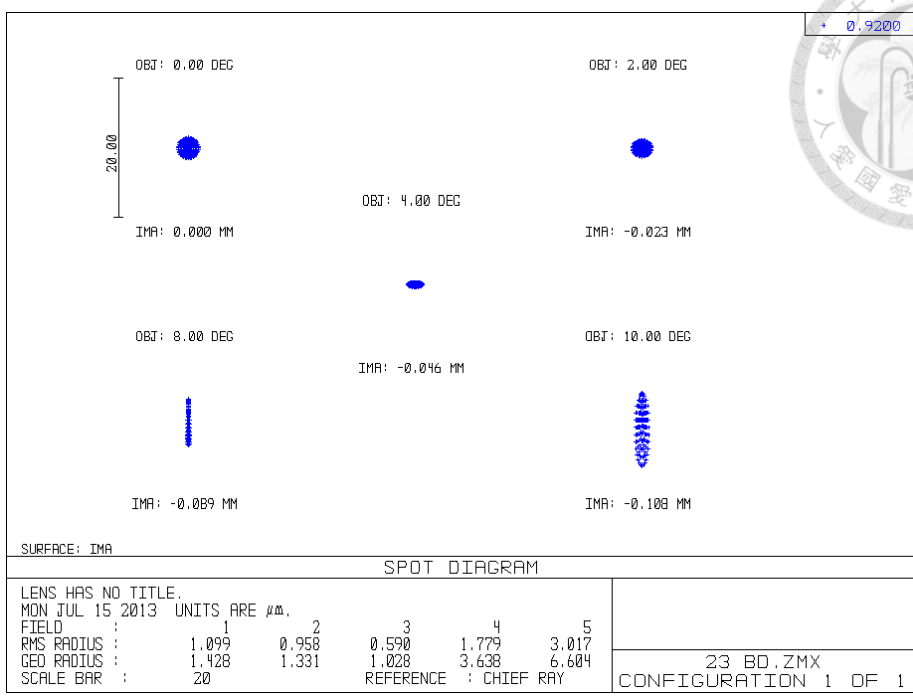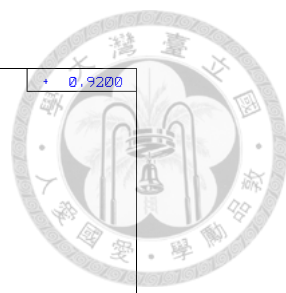
Fig 4.38 Spot diagram of the OPD of the 1:1.5 tube lens pair with the substitute of the BD lens.

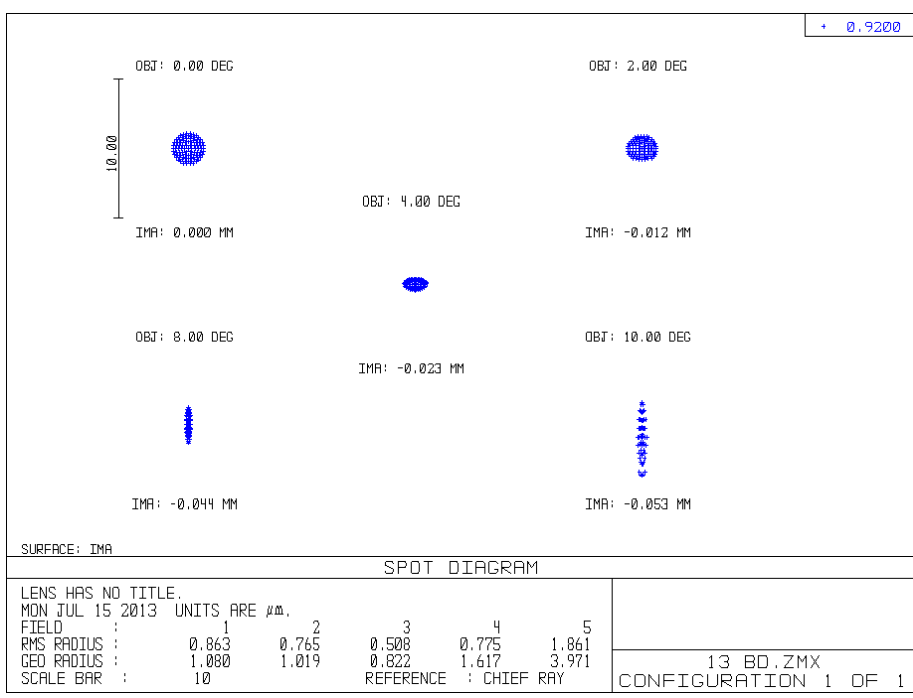**Fig 4.39** Spot diagram of the OPD of the 1:3 tube lens pair with the substitute of the BD lens.
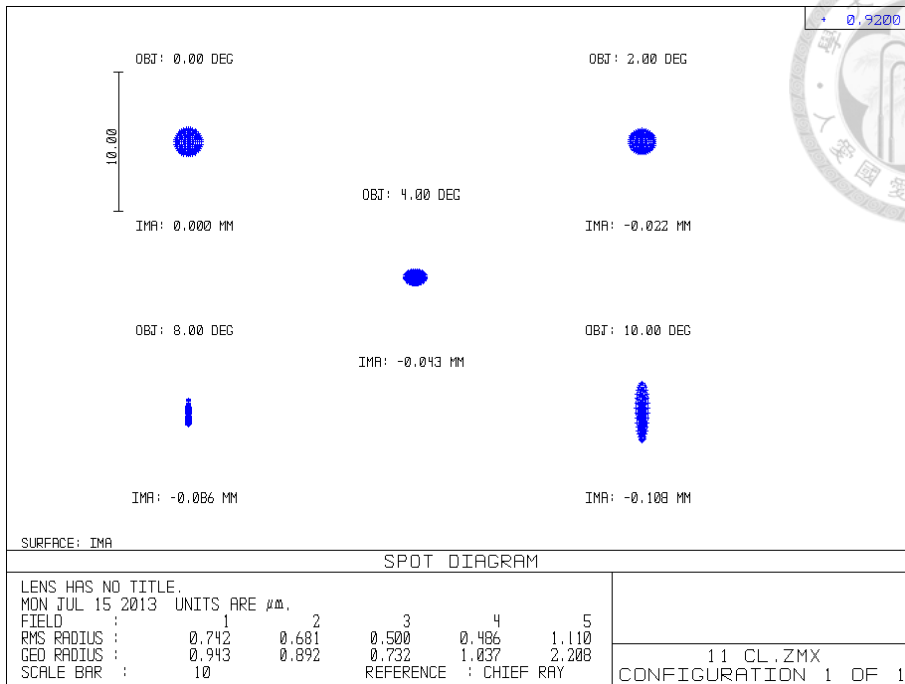
Fig 4.40 Spot diagram of the OPD of the 1:1 tube lens pair with the substitute of the collimating lens.
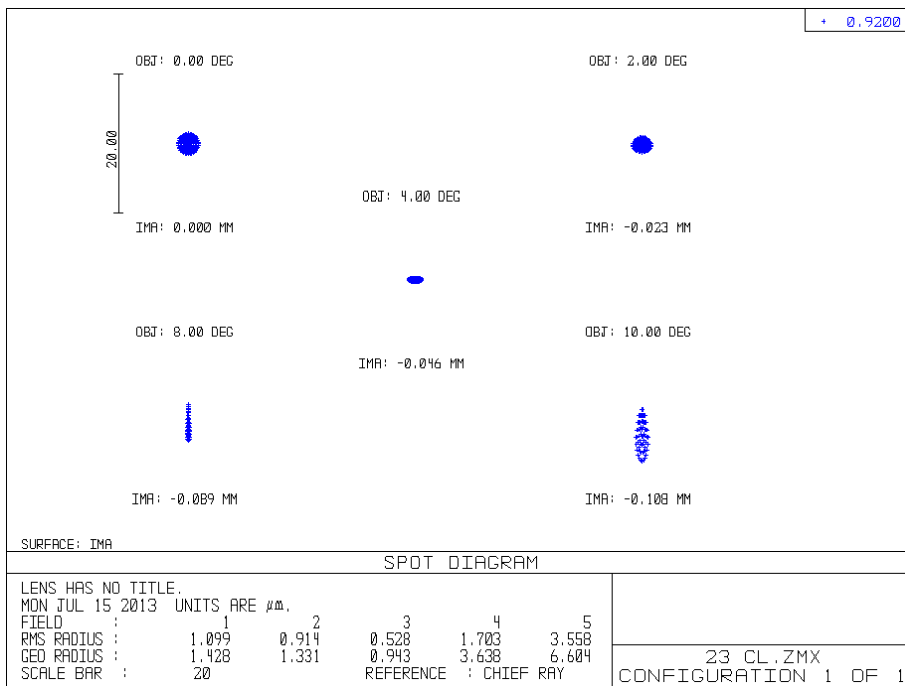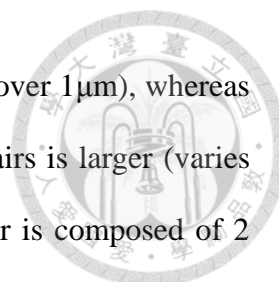

Fig 4.41 Spot diagram of the OPD of the 1:1.5 tube lens pair with the substitute of the collimating lens.

From Fig 4.37 to Fig 4.41 we can find the spot size difference among the 5 incident

angles for the 1:1 tube lens pair is smaller (varies from about 0.5 to over 1μm), whereas the difference of the spot size for the 1:1.5 and the 1:3 tube lens pairs is larger (varies from about 0.5 to over 3μm). This is because the 1:1 tube lens pair is composed of 2 biconvex lenses, which have 4 surfaces degree of freedom (radius of curvature) being designed to compensate the aberration. However, the 1:1.5 and the 1:3 tube lens pairs are composed of common commercial plano-convex lenses, which only has 2 surfaces degree of freedom (radius of curvature), thus they can't compensate the aberration well. The actual value analyzed from the experimental result, however, doesn't vary so much as simulated. The difference between the theoretical value and the experimental value could be attributed to using a substitute for the aspheric lens while running the simulation.

Lens type	Tube lens	ideal	theoretical	experimental
BD	1:1	N/A	0.48~1.13	1.63~2.09
	1:1.5	N/A	0.59~3.02	1.04~1.29
	1:3	0.47	0.51~1.86	0.60~0.80
Collimating	1:1	N/A	0.49~1.11	1.30~1.54
	1:1.5	0.49	0.53~3.56	0.67~0.91

Table 4.5 Resolution comparisons between the ideal values according to Rayleigh's criterion, the theoretical values simulated by ZEMAX, and the values analyzed from the experimental result.

4.4.5 Distortion aberration

The last thing we would like to discuss is the distortion aberration. The aberration is originated from the difference of the transverse magnification of a lens. The two most common distortions are the positive distortion and the negative distortion, or commonly called "pincushion" or "barrel" due to the deformed shapes.
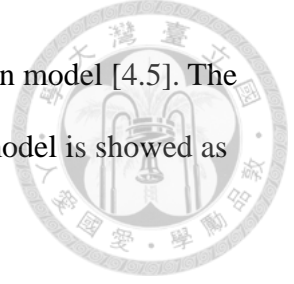
The distortion could be corrected and simulated by Brown's distortion model [4.5]. The model can correct both the radial and the tangential distortion. The model is showed as follows:

$$x_u = (x_d - x_c)(1 + K_1 r^2 + K_2 r^4 + \cdots)$$
$$+ \big(P_1(r^2 + 2(x_d - x_c)^2) + 2P_2(x_d - x_c)(y_d - y_c)\big)(1 + P_3 r^2 + \cdots)$$
$$y_u = (y_d - y_c)(1 + K_1 r^2 + K_2 r^4 + \cdots)$$
$$+ \big(P_2(r^2 + 2(y_d - y_c)^2) + 2P_1(x_d - x_c)(y_d - y_c)\big)(1 + P_3 r^2 + \cdots)$$

where

$(x_d, y_d) = $ distorted image point as projected on image plane as specified lens,

$(x_u, y_u) = $ undistorted image point as projected by an ideal pin-hole camera,

$(x_c, y_c) = $ distortion center (assumed to be the principal point),

$K_n = n^{th}$ radial distortion coefficient,

$P_n = n^{th}$ tangential distortion coefficient,

$r = \sqrt{(x_d - x_c)^2 + (y_d - y_c)^2}$

The distortion is primarily dominated by the low order radial components [4.6]. Barrel distortion typically has a positive K_1 term, whereas pincushion distortion has a negative value. For the mixed (moustache) distortion, it has non-monotonic radial geometric series, which means not every term in the polynomial has to be the same positive or negative. To correct the distortion, software post-processing is usually used.

Here, we demonstrate a way how to correct the distortion simply. The programs we use are simply ImageJ and PhotoImpact. There's a plug-in program for ImageJ which can

alter the value of K_1 and K_2 of Brown's distortion model. This can provide the basic distortion compensation. For example, we may choose the positive value for K_1 and K_2 to deal with the pincushion distortion, and the negative value for the barrel distortion. As for PhotoImpact, it can also compensate the distortion, but it is worked by a moving slidebar instead of altering parameters.

The distortion of our image is not central symmetric and is a mixture of both kinds of distortion. Thus we roughly divide the following Fig 4.42 (a) into two parts. The left part seems to have a barrel distortion, whereas the right one has a pincushion distortion. If we set the value of K_2 to 0.00015 then we can get Fig 4.42 (b), and K_2 to -0.00001 for Fig 4.42 (c). Then we use PhotoImpact to further add some trapezoid distortion for the asymmetric of left and right and the oblique or the central axis, so we can get Fig 4.43 (a) from 4.42 (b) and Fig 4.43 (b) from Fig 4.42 (c). Finally, we reserve only the right part of Fig 4.43 (a) and the left part of Fig 4.43 (b) and add them together to get Fig 4.43 (c). In Fig 4.43 (c) we can find the distortion near the central part is almost removed, but the distortion near the margin still exists. This could be attributed to the higher order K_n term and the deviation of the distortion center. By the way, adding the barrel or the pincushion distortion compensation makes the FOV shrink or broaden respectively. This may lead to a data loss while frame pixels mapping into different frames.
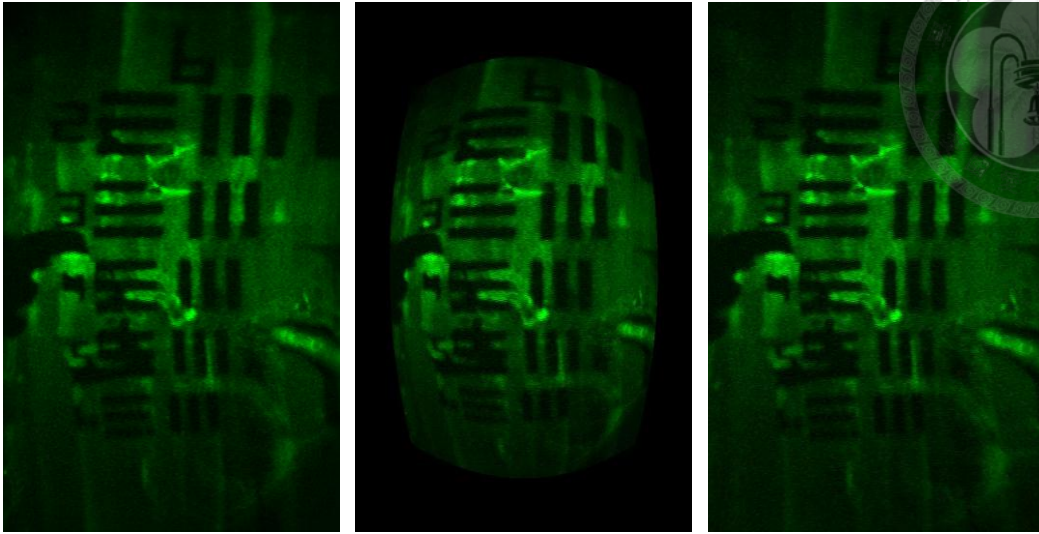
Fig 4.42 (a) The original picture with distortion and without correction. **(b)** The picture adding barrel distortion compensation. **(c)** The picture adding pincushion compensation.
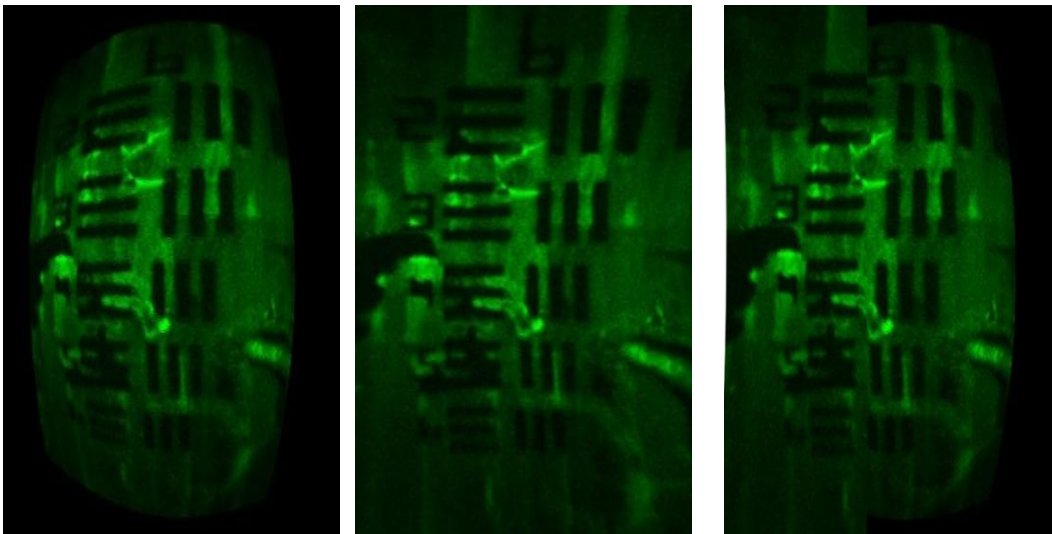

Fig 4.43 (a) The picture with barrel distortion compensation and the trapezoid distortion compensation. **(b)** The picture with pincushion distortion compensation and the trapezoid distortion compensation. **(c)** The picture from the right part of Fig 4.42 (a) and the left part of Fig 4.43 (b) adding together.

4.5 Application

In this section, various kinds of sample image are presented, including two-photon

fluorescence (2PF), second harmonic generation (SHG), and third harmonic generation (THG).

4.5.1 Nonlinear optical sample image

Thanks to Professor Huai-Jen Tsai's help, so we can use the zebrafish with GFP (green fluorescence protein) to test the performance of 2PF microscopy. By different means of genetic engineering, GFP can exist in different parts of the body in zebrafish, such as: muscle, skin, or heart. The excitation wavelength peak for GFP is at 920 nm, and the emission wavelength peak is at 520 nm. Thus we choose Ti:sapphire laser as the excitation source.

The fish used are usually 72 hpf (hours postfertilization) for highly developed. In general, the longer the fish grown, the stronger the fluorescence from the GFP is. However, as the fish grow bigger and thicker, it becomes harder to observe the tissue in the deeper layer of the fish. The penetration depth is restricted not only the wavelength of the illumination, but also the WD (working distance) of the objective.

The zebrafish sample preparation was thanks to the help of Cheng-Yung Lin and Jie-Shin Chen. The typical way to mount the fish is described as follows. First, the fish is anesthetized by tricaine (3-amino benzoic acid ethyl ester). Then agarose gel is introduced to mount the fish on the microslide. A 3D stage is used to move the microslide for different FOV.
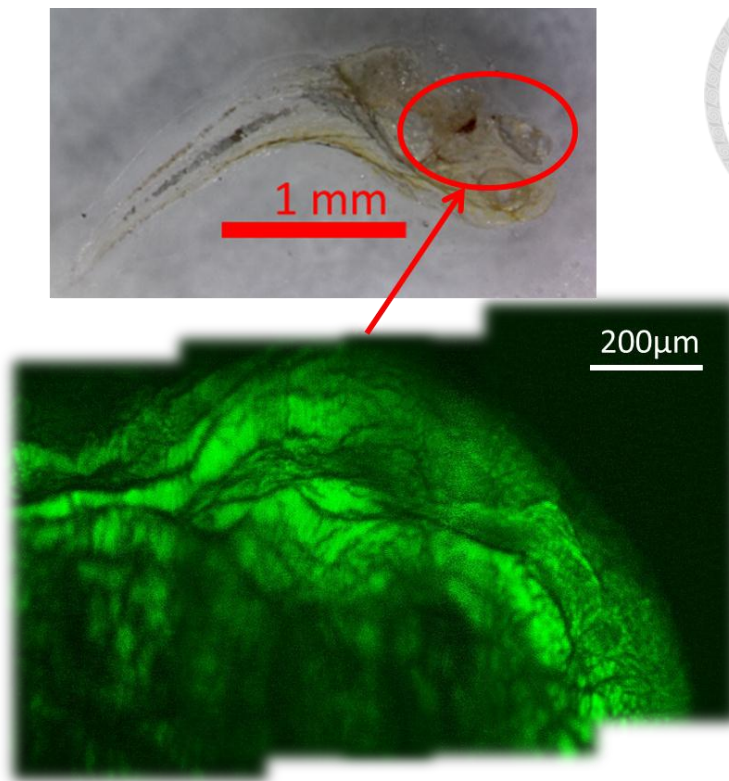
Fig 4.44 2PF images of GFP zebrafish pieced together (BD lens with 1:1 tube lens).

Fig 4.45 2PF images of GFP zebrafish pieced together (BD lens with 1:1 tube lens).

Fig 4.46 2PF images of GFP zebrafish pieced together (BD lens with 1:1 tube lens).

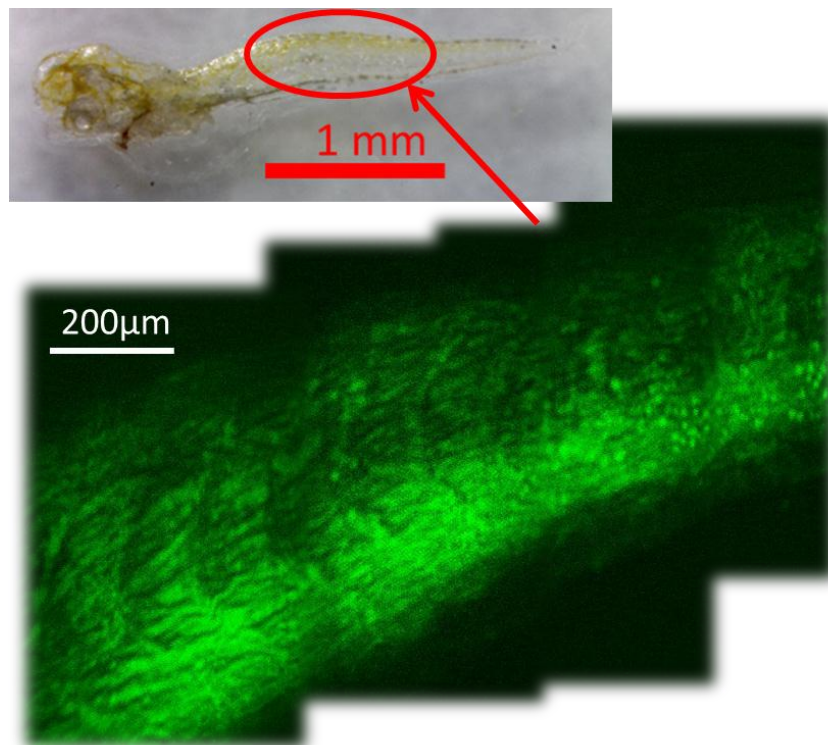**Fig 4.47** 2PF images of GFP zebrafish pieced together (BD lens with 1:1 tube lens).
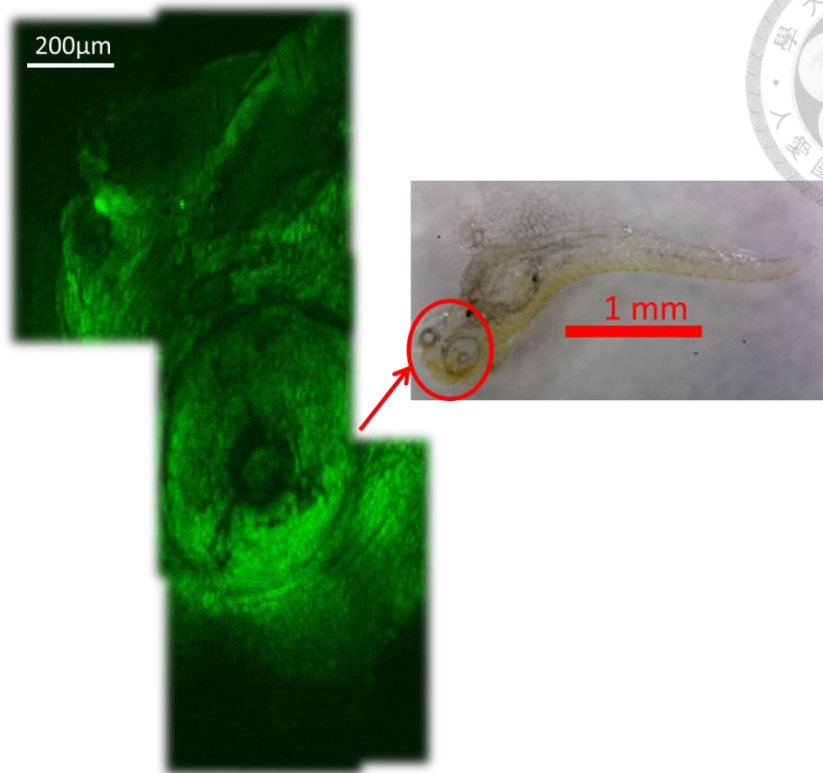
Fig 4.48 2PF images of GFP zebrafish pieced together (BD lens with 1:1 tube lens).

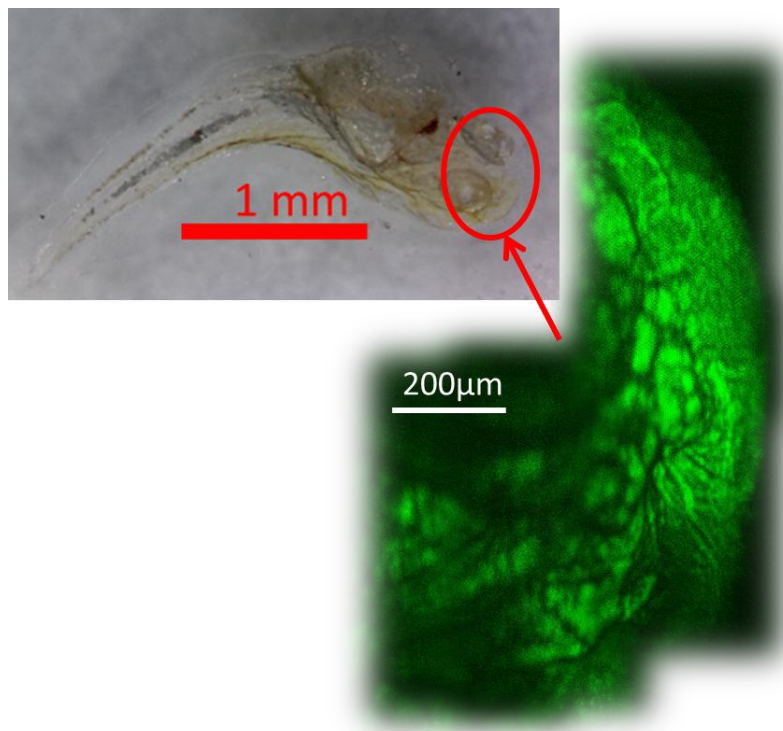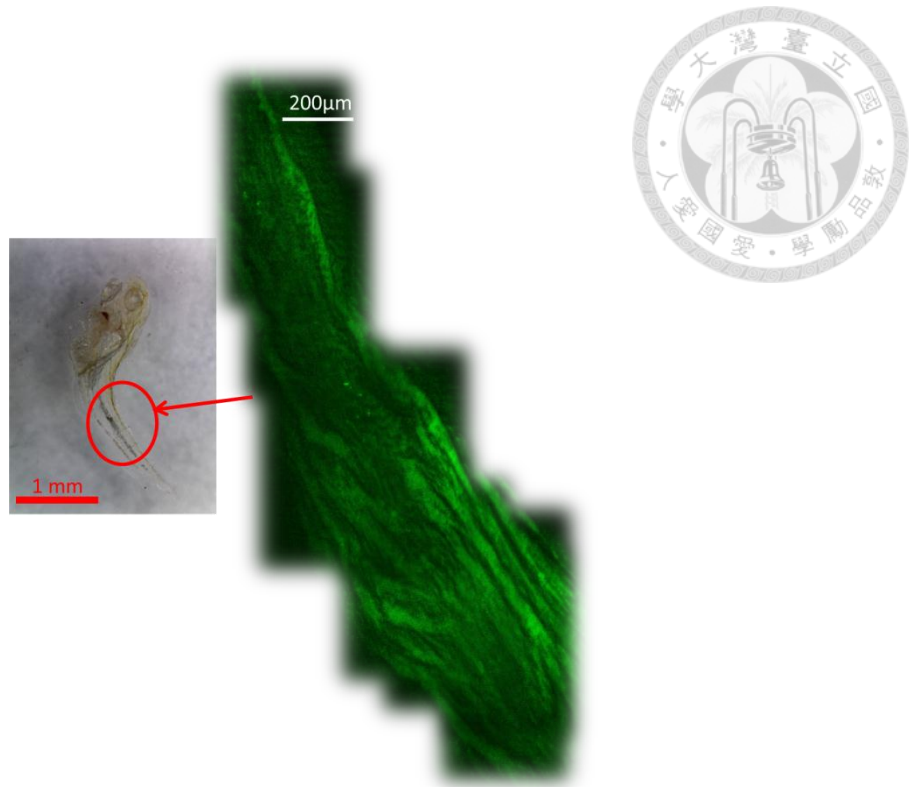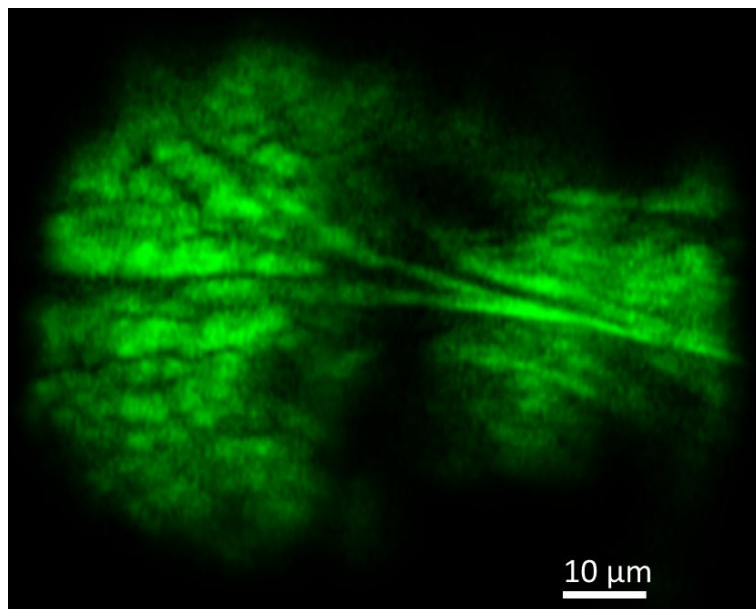**Fig 4.49** 2PF images of GFP zebrafish pieced together (BD lens with 1:3 tube lens).

We chose potato to test the performance of SHG since it contains lots of starch from which we can easily excite the SHG signal. An Yb fiber laser with 1030 nm central

wavelength is used as the excitation source, and the wavelength of the corresponding

SHG is 515 nm. The potato is cut into thin slice for observation.
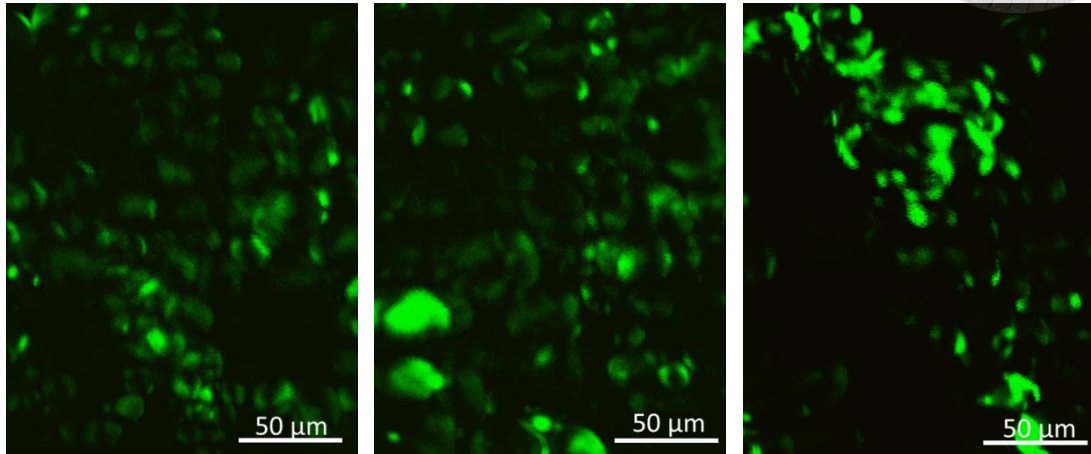
Fig 4.50 Epi-SHG image of potato, excitation wavelength 1030 nm (collimating lens with 1:1 tube lens).

Besides the starch, the collagen of human skin is another source from which SHG can be excited. By

using the same fiber laser, we also get the SHG imaging of collagen in *ex vivo* human skin. FOV: 170 μm

× 220 μm.

The performance of THG is tested by leaves. The excitation source is a Cr:forsterite

laser with central wavelength in 1230nm, and the wavelength of THG is 410 nm.
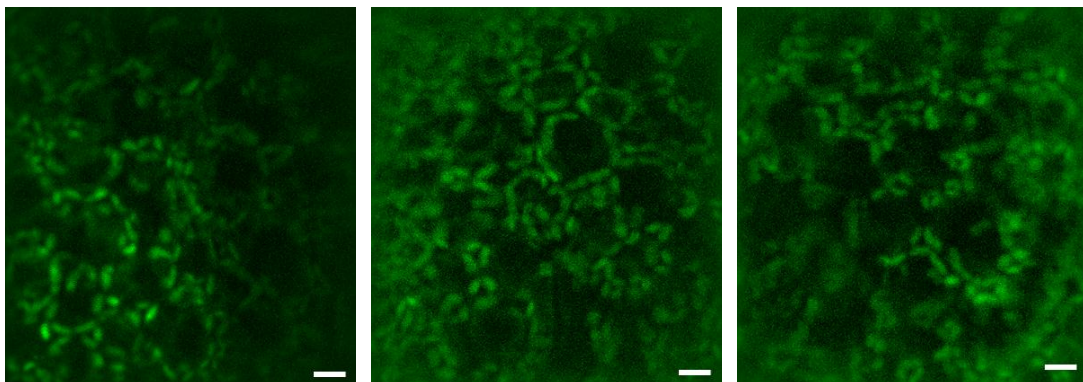

Fig 4.51 2PF image of lower epidermal cells from the leaf of Epipremnum aureum (Devil's ivy). FOV:

165 μm × 179 μm, excitation wavelength 1230 nm (collimating lens with 1:1 tube lens) The scale bar is

15 μm long.
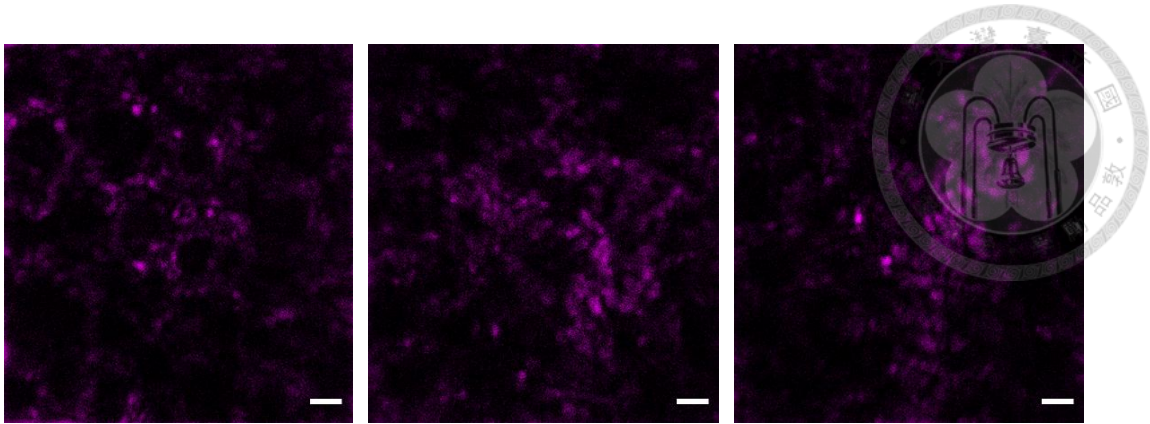
Fig 4.52 THG image of lower epidermal cells from the leaf of Epipremnum aureum (Devil's ivy), FOV:

165 μm × 179 μm, (collimating lens with 1:1 tube lens) The scale bar is 15 μm long.
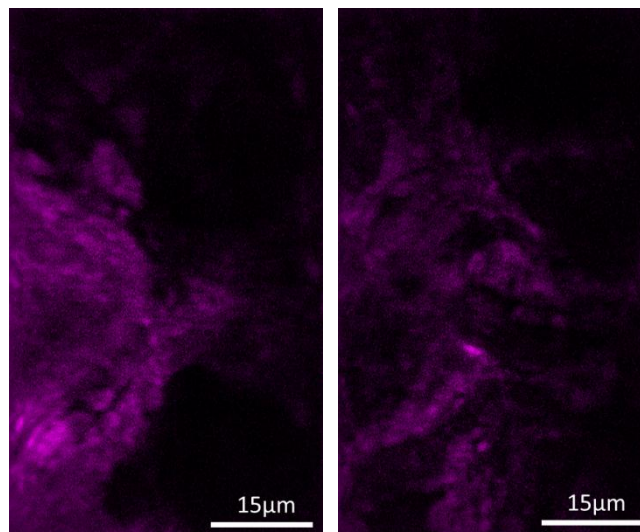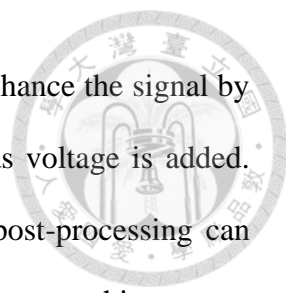
Fig 4.53 THG image of lower epidermal cells from the leaf of Epipremnum aureum (Devil's cry), FOV:

46 μm × 78 μm (BD lens with 1:3 tube lens).

In this section we have showed some sample images of 2PF, SHG, and THG, which shows the capability of the aspheric lens to conduct nonlinear optical microscopy. However, the aspheric lens is still inferior to the commercial objective, which reflects that the excitation power using an aspheric lens as the objective is higher than using a commercial objective. Thus, we have to be aware of the illuminative laser power threshold to avoid the photodamage. The trade-off would be the weaker emitted

nonlinear signal. A PMT (photomultiplier tube) is usually used to enhance the signal by bias voltages. To cope with the weaker photonic signal, higher bias voltage is added. However, the noise is also amplified simultaneously. The digital post-processing can improve the situation, such as using contrast enhancement, denoise, or smoothing.

The excitation power we used to excite 2PF (520 nm) is 20~50 mW by 920 nm excitation. For HG, the excitation power is 50~100 mW by 1230 nm excitation to excite SHG (615 nm), and THG (410 nm), which reflects that higher power is needed to generate the HG signal than the multi-photon signal. To avoid photodamage, we prefer longer wavelength infrared excitation source to excite SHG and THG, such as a Cr: forsterite laser or a Yb fiber laser.

4.5.2 Real-time zebrafish heartbeat observation

We choose a GFP zebrafish and observe its heart to demonstrate the ability of *in-vivo* video-rate real-time imaging by 2PF microscopy. Two issues are related to this test. The first one is can we see a real-time heartbeat? Since the fish is very fragile, we should control the illumination power carefully. Thus, the incidence can not only excite the nonlinear signal, but also keep the fish safe without damage. The second issue is can we can count the heart rate? This has much to do with the scanning speed and the data acquisition ability of our system.

To conduct this experiment, zebrafish is first anesthetized and carefully mounted into a substance on the microslide. This work also thanks to the help of Cheng-Yung Lin and Jie-Shin Chen from Professor Huai-Jen Tsai's lab. A 3D stage was used to move the microslide and locate where the heart is. Finally we found the location of the heart

within one minute and successfully observe the heartbeat.

In Fig 4.55 we can see the heart of a zebrafish is composed of two parts. The bigger part is the atria, and the smaller part is the ventricle. By instant observation, the heart rate is around 180/min. By frame doubling as we mentioned before, we can further measure the heart rate with a slower playing speed.
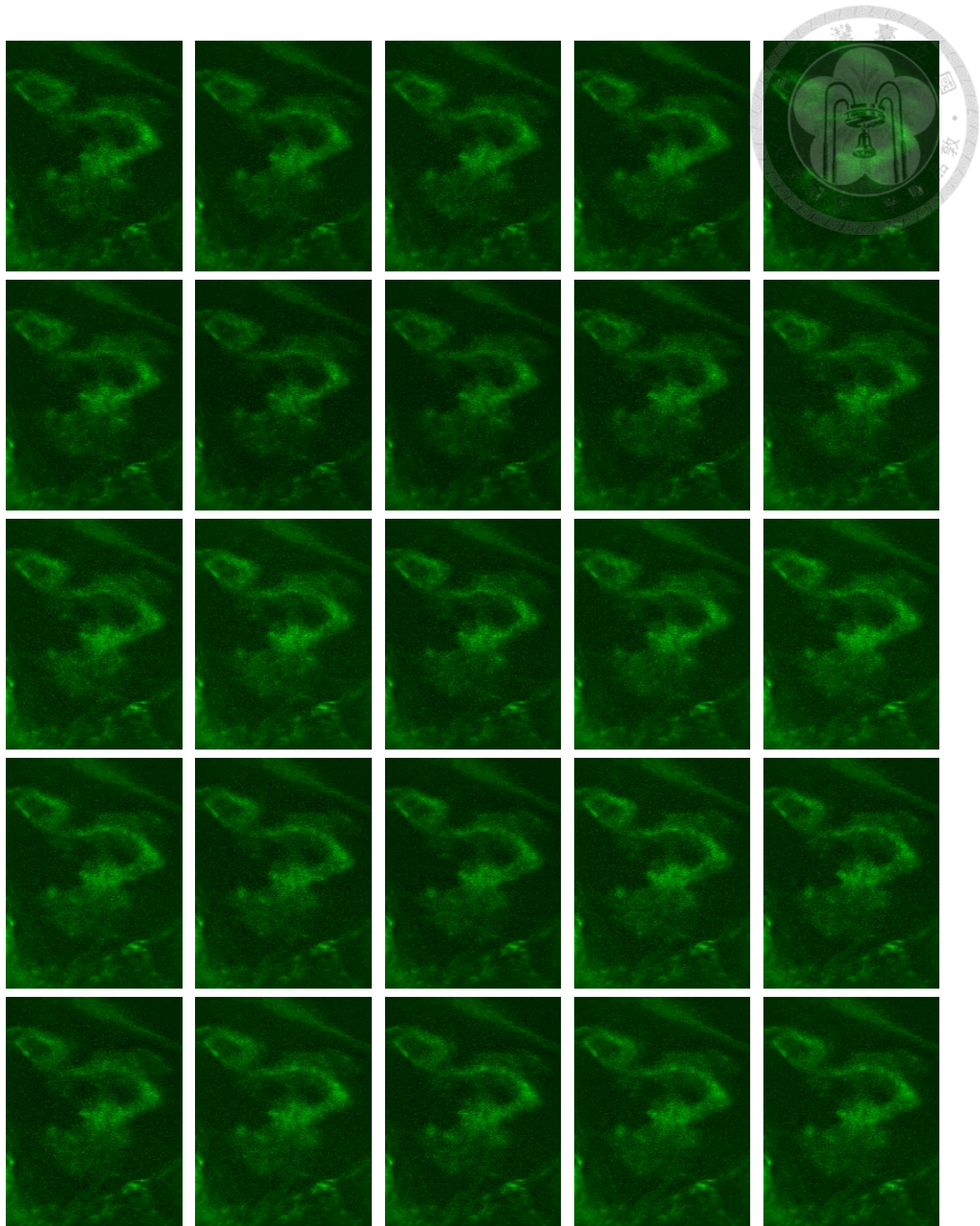
Fig 4.54 Snapshot of the heartbeat of the zebrafish with vascular endothelial GFP (BD lens with 1:1 tube lens).
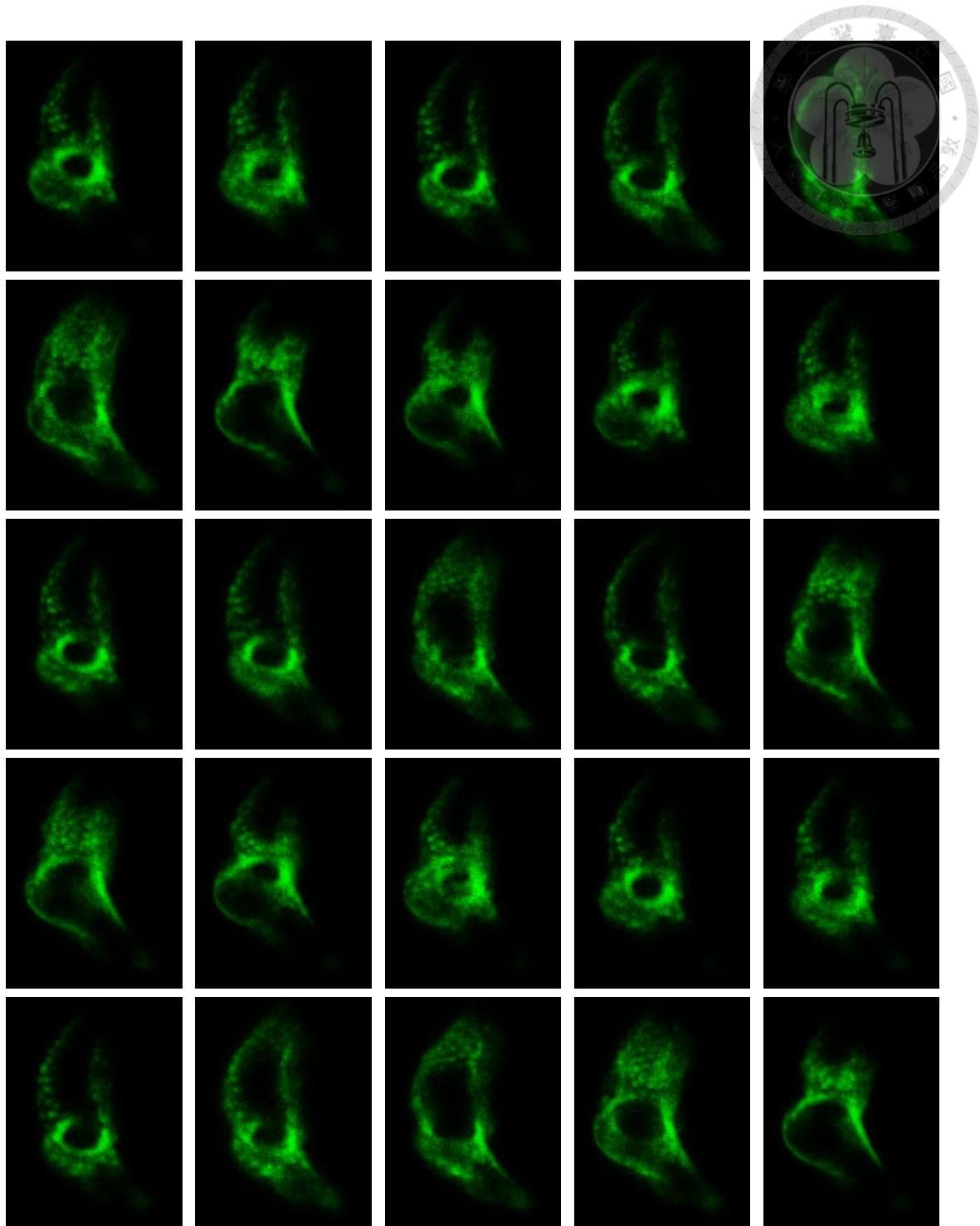
Fig 4.55 Snapshot of the heartbeat of the zebrafish with myocardium GFP (BD lens with 1:1 tube lens).
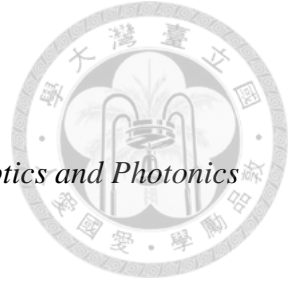
Reference

[4.1]   C. Pruss, E. Garbusi, and W. Osten, "Testing aspheres," *Optics and Photonics News* **19** (4), pp. 24-29 (2008).

[4.2]   S. W. Smith, *The Scientist & Engineer's Guide to Digital Signal Processing* (California Technical Pub, 1997).

[4.3]   M. Offroya, Y. Roggob, and L. Duponchel, "Increasing the spatial resolution of near infrared chemical images (NIR-CI): The super-resolution paradigm applied to pharmaceutical products," *Chemometrics and Intelligent Laboratory Systems* **117**, pp. 183-188 (2012).

[4.4]   J. Squier, and M. Müller, "High resolution nonlinear microscopy: A review of sources and methods for achieving optimal imaging," *Rev. Sci. Instrum.* **72**, pp. 2855-2867 (2001).

[4.5]   D. C. Brown, "Decentering distortion of lenses," *Photogrammetric Engineering* **32** (3), pp. 444-462 (1966).

[4.6]   J. P. de Villiers, F. W. Leuschner, and R. Geldenhuys, "Centi-pixel accurate real-time inverse distortion correction," *International Symposium on Optomechatronic Technologies*. SPIE (2008).

Chapter 5 Summary & future work

In this thesis, we demonstrate a miniaturized nonlinear optical microscope system using two different mini aspheric lenses (a laser diode collimating lens with 0.8 NA and a BD lens with 0.85 NA) as the objective and using the MEMS mirror as the scanner. The cost of the mini aspheric lens is cheap. Each of the single piece costs not more than 1000 NTD (30 USD). Thus, a disposable objective is possible for each particular application.

2PF or HG microscopy is able to be conducted with a miniaturized imaging head. FOV from 59 μm × 93 μm up to 178 μm × 280 μm is realized by simply changing the combination of the aspheric lens and the tube lens pair (ratio of magnification 1:1, :1.5, and 1:3) or slightly adjusting the distance between them. Among these combinations, lateral resolution varies from about 2 μm to 0.6 μm as the CA gradually fully covered. Therefore, we can apply the imaging head on different purpose, either for larger FOV with a lower resolution or for smaller FOV with a higher resolution. Frame rate up to 34/s can be reached. The high frame-rate acquisition ability is demonstrated by an *in-vivo* observation of the zebrafish heartbeat.

Finally, the performance of our system is listed in Table 5.1.

Lens type	Tube Lens	FOV	Best Lateral Resolution	Frame Rate
BD	1:1	178×280	1.63	
	1:1.5	121×200	1.04	
	1:3	59×93	0.60	34/s
Collimating	1:1	87×140	1.30	
	1:1.5	62×112	0.67	

Table 5.1 Performance of all kinds of combination of the aspheric lens and the tube lens pair. The unit of FOV and the lateral resolution is μm.
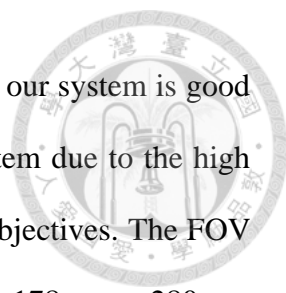
In comparison with the performance from other groups in Table 5.2, our system is good at the frame rate. The resolution is also better than most of the system due to the high NA aspheric lenses, except for some commercial water immersion objectives. The FOV doesn't dominate, however it still varies from 59 μm × 93 μm up to 178 μm × 280 μm by changing the tube lens pair.

From	FOV	NA	Lateral Resolution	Frame Rate
Adela Ben-Yakar	36~310 in diameter	0.46	1.64±0.09	10
	142×297	0.55	1.27±0.03	7
Chi-Kuang Sun	70×76	0.9 (water)	<1	31
	70×100	1.2 (water)	0.4	24
Chris Xu	150~1000 in extent	0.18 or 0.5	0.976	1
	110 in extent	0.8 (water)	0.8	4.1
Eric Seibel	up to 200 in diameter	0.5	~1	25
Fabio Mammano	80 in extent	0.4~0.75	0.9~1.2	N/A
Fritjof Helmchen	65 in extent	0.8 (water)	N/A	2
	100 in extent	N/A	N/A	N/A
	up to 800 in diameter	0.5	>4	N/A
Joachim Knittel	up to 280 in extent	0.5	3.3	N/A
K. König	up to 420 in extent	0.65	0.6	2.6
	up to 420 in extent	0.65	x=1.08,y=0.67	6
Mark J. Schnitzer	up to 211 in diameter	0.46, 0.42, 0.26	1.26±0.1	N/A
	at least 166 in extent	0.47, 0.46, 0.38	0.86±0.07	<3
	145~215 in extent	0.48	1.21±0.04	2
	up to 80×20	0.46	N/A	N/A
	up to 295×100	0.58	1.29±0.05	1~15
	at least 40 in extent	0.82	1.0±0.2	N/A
	275 in extent	0.49	0.9	
	130 in extent	0.48	1	
	75 in extent	0.45	1.2	
	700 in extent	0.49	0.9	1~5
	350 in extent	0.47	1	
	120 in extent	0.65	0.8	
	75 in extent	0.82	0.6	

Michael J. Levene	>120 in extent	0.6	0.618	N/A
Min Gu	at least 111 in extent	0.5	N/A	N/A
	at least 147×85	0.6	N/A	N/A
	up to 475×475	0.35	~1	2.6
Robert J. Gordon	at least 150 in diameter	N/A	1.5	1.1
Shuo Tang	at least 91×91	0.62	N/A	N/A
	up to ~200 in extent	0.62	~2	0.25
Winfried Denk	up to ~250 in extent	0.9 (water)	0.9±0.1	N/A
Xingde Li	up to 120~220 in diameter	0.46	2±0.2	2.6
	up to ~320 in diameter	N/A	~1.6	3.3
	120 in diameter	0.5	N/A	3
	150 in diameter	N/A	N/A	~3
	110 in diameter	0.8	N/A	2.6
	~100 in diameter	N/A	N/A	1.9
	~100 or 150 in diameter	0.8	~1.2	~3
	110 in diameter	~0.7	~0.7	~3

Table 5.2 System performance of the FOV, the NA, the lateral resolution, and the frame rate.

The possible improvement for the system is to redesign the 1:1.5 and 1:3 tube lens pair instead of using simple plano-convex spherical lenses, just like the 1:1 tube lens pair optimized by a simulation program. On the other hand, the 1:3 bean size magnification is too much for the BD, which means some power is wasted outside the clear aperture. After recalculation, a 1:2.5 tube lens would be a more appropriate one. The development and improvement of the electronic control is another important issue. This work roughly consists of two parts: the firmware, and the hardware. The firmware is about the FPGA code which is the most critical and important part of the whole system, since it dominates the synchronization of the driving MEMS mirror, the data acquisition, and the instantaneous mapping.

The hardware part concerns the more durable or efficient MEMS mirror and the stable

FPGA control board. A reliable electronic system is highly desired, since a severe electric board dysfunction had ever postponed our research for almost half a year. Thanks to the help of Wei-Cheng Kuo and Josh Tu, so we can finally debug successfully and continue the research.

With the latest MEMS scanner, there are still some works we can do. By alternating the scanning angle of the MEMS mirror in fast and slow axis, we can make the FOV with equal extent, thus both the lateral resolutions in x and y directions may be even. According to our calculation, the frame rate can also reach over 50/s without missing pixels by integrating the latest MEMS scanner.

The post processing to correct the distortion aberration is another work. By calibrating the deformed FOV, we can analyze the resolution more accurately or observe the sample with periodic rectilinear structures without distortions.